Title
Exploring the Texture of Ocean-Atmosphere Redox Evolution on the Early Earth

Author
Reinhard, Christopher Thomas

Publication Date
2012

UNIVERSITY OF CALIFORNIA
RIVERSIDE

Exploring the Texture of Ocean-Atmosphere Redox Evolution on the Early Earth

A Dissertation submitted in partial satisfaction
of the requirements for the degree of

Doctor of Philosophy

in

Geological Sciences

by

Christopher Thomas Reinhard

September 2012

Dissertation Committee:
Dr. Timothy W. Lyons, Chairperson
Dr. Gordon D. Love
Dr. Nigel C. Hughes

The Dissertation of Christopher Thomas Reinhard is approved:

Committee Chairperson

University of California, Riverside

ACKNOWLEDGEMENTS

It goes without saying (but I'll say it anyway…) that things like this are never done in a vacuum. Not that I've invented cold fusion here, but it was quite a bit of work nonetheless and to say that my zest for the enterprise waned at times would be to put it euphemistically. As it happens, though, I've been fortunate enough to be surrounded these last years by an incredible group of people. To those that I consider scientific and professional mentors that have kept me interested, grounded, and challenged – most notably Tim Lyons, Rob Raiswell, Gordon Love, and Nigel Hughes – thank you for all that you do. I also owe Nigel and Mary Droser a particular debt of graditude for letting me flounder a bit my first year at UCR, being understanding and supportive, and encouraging me to start down the road to where I've ended up (for better or worse).

I've also been very fortunate to be surrounded by a great group of people in the lab (a credit to Tim's ability to foster a really special atmosphere within his group) and in the UCR Earth Sciences Department writ large, to whom I owe countless thanks for myriad things – helping me with analytical and lab issues, chatting about ideas over coffee, talking me off a ledge or two (ahem…Ben), playing footy on the quad, and too many other things to mention. To Steve Bates, Ben Gill, Clint Scott, Silke Severmann, Bill Gilhooly, Noah Planavsky, Jeremy Owens, Andy Robinson, Natascha Riedinger, Anthony Chappaz, Dalton Hardisty, and all of those in Tim's lab (and extended lab) that I've had the pleasure to cross paths with – many, many thanks. My time in Riverside also wouldn't have been what it was without Ryan McKenzie, Clara Lee, Greg Lawson, Daniel Garson, Greg Miller, Stephan Hlohowskyj, and Tom Bristow.

Thanks also to my family – nuclear and otherwise – for being a constant source of support, encouragement, and inspiration. I've always been encouraged to do what interests me, for as long as I can remember, and I don't take that for granted. Lastly (but not leastly), to Katy Jean Zimmermann – the days are few that I'm not struck by how lucky I am to have come across you. Thank you for everything – your compassion, sense of humor, and kindness are all things I strive to emulate. You make me want to be a better person in this world.

DEDICATION

I had two dreams about him after he died…it was like we was both back in older times and I was on horseback goin through the mountains of a night. Goin through this pass in the mountains. It was cold and there was snow on the ground and he rode past me and kept on goin. Never said nothin. He just rode on past and he had this blanket wrapped around him and he had his head down and when he rode past I seen he was carryin fire in a horn the way people used to do and I could see the horn from the light inside of it. About the color of the moon. And in the dream I knew that he was goin on ahead and that he was fixin to make a fire somewhere out there in all that dark and all that cold and I knew that whenever I got there he would be there. And then I woke up.

-Cormac McCarthy

For Jeffery Paul John Reinhard (1949 – 2001)

ABSTRACT OF THE DISSERTATION

Exploring the Texture of Ocean-Atmosphere Redox Evolution on the Early Earth

by

Christopher Thomas Reinhard

Doctor of Philosophy, Graduate Program in Geological Sciences
University of California, Riverside, September 2012
Dr. Timothy W. Lyons, Chairperson

The evolution of oxygenic photosynthesis has dramatically reshaped the chemistry of the surface Earth, and the presence of significant quantities of O_2 in the atmosphere and ocean now drives the fundamental dynamics of nearly all quantitatively significant biogeochemocal cycles (C, S, P, N, Fe). Whether by direct consumption through the metabolic demands of large, complex organisms, or through the recycling of essential substrates within microbial ecosystems, biologically produced O_2 provides nearly all of the compounds used in metabolic electron transfer on a global scale. Although it is widely accepted that the partial pressure of O_2 in Earth's atmosphere has increased through time (with attendant, although somewhat complex, changes in ocean ventilation), there is still much debate surrounding the timing of the emergence of oxygenic photosynthesis and little is known about the detailed tempo and mode with which this metabolic innovation came to shape early Earth surface chemistry.

This dissertation explores the early oxygenation of Earth's atmosphere and the relationship between atmospheric oxygen levels and ocean ventilation from a variety of perspectives. First, empirical data based on an integrated suite of paleoredox proxies is used to suggest that biological oxygen production emerged and began exerting significant effects on Earth surface chemistry at least 100 million years prior to the initial accumulation of large quantities of O_2 in the atmosphere (often referred to as the "Great Oxidation Event", approximately 2.4 billion years ago). The implications of this time lag between metabolic innovation and large-scale biogeochemical reorganization are explored through a series of quantitative models, focusing on the thermodynamics and kinetics of mineral reactions under various Earth surface conditions, regional oceanographic modeling of surface ocean O_2 cycling, and a global sulfur isotope mass balance model that explicitly incorporates rare sulfur isotope systematics (^{33}S, ^{36}S) and the dynamics of sedimentary recycling on long timescales. Finally, the dynamics of ocean ventilation following the initial accumulation of oxygen in the atmosphere are explored by combining a large trace metal database with a spatially explicit mass balance model that exploits the differing redox behavior and surface cycling of molybdenum (Mo) and chromium (Cr).

TABLE OF CONTENTS

CHAPTER 1

INTRODUCTION 1

References 6

CHAPTER 2

A LATE ARCHEAN SULFIDIC SEA STIMULATED BY EARLY OXIDATIVE WEATHERING OF THE CONTINENTS..8

Preface 8

Introduction 8

Main Article 9

Supplementary Information 18

Geological Setting..18

Analytical Methods 21

Oxidative Mobilization of Crustal Sulfur Under Low atmospheric pO_2...............23

Sulfur Isotope Compilation 27

Alternative Hypotheses for the Observed Sulfur Isotope Pattern 30

References 32

CHAPTER 3

OXIDATIVE WEATHERING ON THE EARLY EARTH 38

Preface 38

Introduction 38

Main Article 39

Introduction..39

Alternative Oxidants 42

Accumulation of O_2 in the Surface Ocean 47

Oxidative Processing on the late Archean Earth..57

Discussion 64

Conclusions..66

References 69

CHAPTER 4

LONG-TERM SEDIMENTARY RECYCLING OF RARE SULFUR ISOTOPE ANOMALIES AND ITS SIGNIFICANCE FOR RECONSTRUCTING ATMOSPHERIC EVOLUTION...81

Preface 81

Introduction 81

Main Article 82

Supplementary Information..92

Sulfur Isotope Database..92

Model Setup 93

References 99

CHAPTER 5

A COUPLED MASS BALANCE APPROACH FOR RECONSTRUCTING OCEANIC REDOX LANDSCAPES: PROTEROZOIC CASE STUDY 107

Preface 107

Introduction 107

Main Article 108

The Mid-Proterozoic Geochemical Record **................112**

Interpreting the Enrichment Record: A Model for Global Mass Balance and Burial in Marine Sediments **................115**

Interpreting the Enrichment Record: Model Results **................119**

A 'Biologically Sulfidic' Ocean **................121**

Conclusions **................125**

Supplementary Information 128

Metal Enrichment Database and Filtering Protocols **................128**

Modern Molybdenum (Mo) Mass Balance **................129**

Modern Chromium (Cr) Mass Balance **................133**

Hydrothermal Cycling of Mo and Cr **................136**

Offshore Scaling of Metal Burial Rates in the Model **................139**

Prescribed Perturbations in the Model and the Role of Reducing Sediments **.....143**

Using the Model to Calculate Authigenic Metal Enrichments **................146**

References 150

CHAPTER 6

CONCLUSION 161

APPENDIX A

ANALYTICAL DATA FOR THE ABDP-9 CORE...162

APPENDIX B

SOURCES FOR THE CHROMIUM AND MOLYBDENUM SHALE ENRICHMENT DATABASE...165

References 173

LIST OF FIGURES

Fig. 1.1. Schematic depiction of the global biogeochemical oxygen cycle **2**

Fig. 1.2. Summary of atmospheric and ocean redox states through Earth's history........... **3**

Fig. 2.1. Stratigraphic profiles of reactive iron chemistry, molybdenum enrichment, and total organic carbon (TOC) content for the ABDP-9 drillcore **12**

Fig. 2.2. Compilation of rare sulfur isotope data for late Archean Hamersley Basin marine sulfides, showing distributions in $\delta^{34}S - \delta^{33}S$ (a) and $\delta^{34}S - \Delta^{33}S$ (b) space......... **15**

Fig. 2.3. Schematic representation of atmosphere-ocean chemistry during late Archean time in the Hamersley Basin **17**

Fig. 2.S1. Generalized stratigraphy and absolute age constraints for the late Archean Hamersley Basin, detailing the units represented in the interval of the ABDP-9 core studied here **20**

Fig. 2.S2. Crossplots of reactive iron species in the Mt. McRae Shale from the ABDP-9 core.. **23**

Fig. 2.S3. Estimated dissolution kinetics of pyrite under various atmospheric pO_2 and pH conditions **26**

Fig. 3.1. Schematic depiction of the surface ocean physical-biogeochemical model used to calculate steady state dissolved O_2 (a), and paramaterization of vertical transport rates as a function of average surface wind speed implemented in the model (b) **49**

Fig. 3.2. Results from the surface ocean physical-biogeochemical model, depicting contours of steady state dissolved O_2 as a function of average surface wind speed and carbon export flux **..56**

Fig. 3.3. A range of algorithms used to describe the flux of labile carbon to the sediment-water interface as a function of sediment accumulation rate (a), and oxygen penetration depths as a function of bottom water dissolved O_2 at a range of sedimentation rates as predicted by the M96 algorithm used in this study **...........62**

Fig. 3.4. Calculations depicting the timescale comparisons explored in this study. Panel (a) shows timescales of pyrite dissolution due to oxidation by O_2 in shallow marine sediments at a range of bottom water O_2 concentrations, compared with timescales of burial below the zone of O_2 penetration. Panel (b) shows dissolution timescales for pyrite in a fluid at equilibrium with various pO_2 values, compared with microbially enhanced dissolution rates and soil formation timescales on the modern Earth**..65**

Fig. 4.1. Database of $\Delta^{33}S$ ($\Delta^{33}S = \delta^{33}S - 0.515*\delta^{34}S$) through time (a) and the cumulative average $\Delta^{33}S$ value as a function of database age (b). Shaded box in (a) depicts the average ±2SD for all post-2200 Ma data. Shaded boxes in (b) denote 95% confidence intervals around each cumulative mean **..........................84**

Fig. 4.2. Schematic of the sulphur isotope mass balance model used in this study. Arrows denote flux terms (labeled "F_i"), while boxes denote various oceanic and crustal sulphur reservoirs (labeled "M_i") **..86**

Fig. 4.3. Overview of modeling results for the sedimentary recycling of rare sulphur isotope anomalies. The black solid curve in all cases represents the reference model. Dashed curves represent sensitivity analyses. The shaded box denotes the average ±2SD of all post-2200 Ma data **88**

Fig. 4.S1. Cumulative average $\Delta^{33}S$ value (a) and database size (b) as a function of database age. Error bars in (a) denote 95% confidence intervals around the cumulative mean of the data. Filled symbols represent complete database, while open symbols represent the filtered database **93**

Fig. 5.1. Database of sedimentary chromium (a) and molybdenum (b) enrichments in anoxic and euxinic black shales through time **113**

Fig. 5.2. Schematic depiction of global chromium (a) and molybdenum (b) mass balance models utilized in this study **117**

Fig. 5.3. Estimated sedimentary enrichments of chromium (a) and molybdenum (b) in a generalized continental margin setting as calculated by the model **121**

Fig. 5.4. The effects of deviating from a strictly first-order mass balance model. Panel (a) shows molybdenum burial rates as a function of ambient seawater molybdenum concentrations for four theoretical response relationships and three modern perennially euxinic marine basins. Panel (b) shows the effect of altering the burial rate scaling on calculated steady state seawater Mo concentrations at increasing extents of euxinic seafloor **123**

Fig. 5.S1. Sensitivity analysis of variations in the input flux for the chromium and molybdenum mass balance models. Panels (a-c) examine the sensitivity of the

chromium model to decreased input, while panels (d-f) examine the sensitivity of the molybdenum model to both increased and decreased input fluxes**...............131**

Fig. 5.S2. Parameterization of offshore decrease in metal burial rates implemented in the model for chromium (a) and molybdenum (b) **142**

Fig. 5.S3. Sensitivity of model results to variations in metal burial rate and bulk mass accumulation rate. Panels (a), (c), and (e) show calculated chromium enrichments as a function of anoxic seafloor. Panels (b), (d), and (f) depict calculated molybdenum enrichments as a function of euxinic seafloor **...............................148**

LIST OF TABLES

Table 3.1. Parameters implemented in the surface ocean physical-biogeochemical model used in this study **54**

Table 3.2. Parameters used for estimating sediment O_2 penetration in a simple diagenetic model **61**

Table 4.S1. Summary of parameter values used in the reference model **98**

Table 5.S1. Summary of flux terms in the modern molybdenum mass balance **132**

Table 5.S2. Summary of flux terms in the modern chromium mass balance **136**

Table 5.S3. Estimated fluxes of molybdenum and chromium associated with seawater-basalt interaction at high temperature **138**

Table 5.S4. Estimated fluxes of molybdenum and chromium associated with seawater-basalt interaction at low temperature **139**

Table A1. Analytical iron speciation data for the Mt. McRae Shale and associated units within the ABDP-9 core **162**

Table B1. Age constraints and geologic setting of units compiled for the chromium and molybdenum enrichment database **165**

CHAPTER 1

INTRODUCTION

The evolution and ecological success of oxygenic photosynthesis on Earth represents a biological and geochemical singularity. This process, although certainly not the only variant on the theme of photosynthetic energy conservation (*1*), has come to utterly transform the surface chemistry of the Earth, providing most of the substrates involved in planetary metabolism and ultimately fostering the evolution and development of large, complex organisms. This process of co-evolution between biological oxygen production and the geochemical conditions that have resulted in its accumulation to significant levels in the atmosphere is perhaps the defining characteristic of the planet Earth, so much so that the spectroscopic observation of significant quantitities of oxygen or ozone in a planetary atmosphere is viewed as strong evidence for a surface biosphere and is considered a prerequisite for the development of complex life (*2-4*).

Oxygenic photosynthesis if often represented in condensed form as:

$$CO_2 + H_2O \overset{h\nu}{\rightarrow} \{CH_2O\} + O_2 \, , \tag{1.1}$$

where $h\nu$ denotes ~10-12 quanta of photons and $\{CH_2O\}$ is a dramatically oversimplified representation of organic matter. It should be noted that the simplicity of the above stoichiometric representation belies the incredible biochemical complexity of the task (*5-7*). In any case, the ability to perform this reaction has conferred a decided advantage on organisms that can manage it, as it releases a tremendous amount of energy and uses as its electron donor the ubiquitous water molecule. In contrast, photosynthetic organisms that derive their reducing power from other compounds (such as H_2S or Fe^{2+}) are of necessity restricted to interface environments of active redox cycling where their electron donors are readily available. However, it is the *waste product* of this process, molecular oxygen (O_2), that has ultimately given rise to the modern Earth surface.

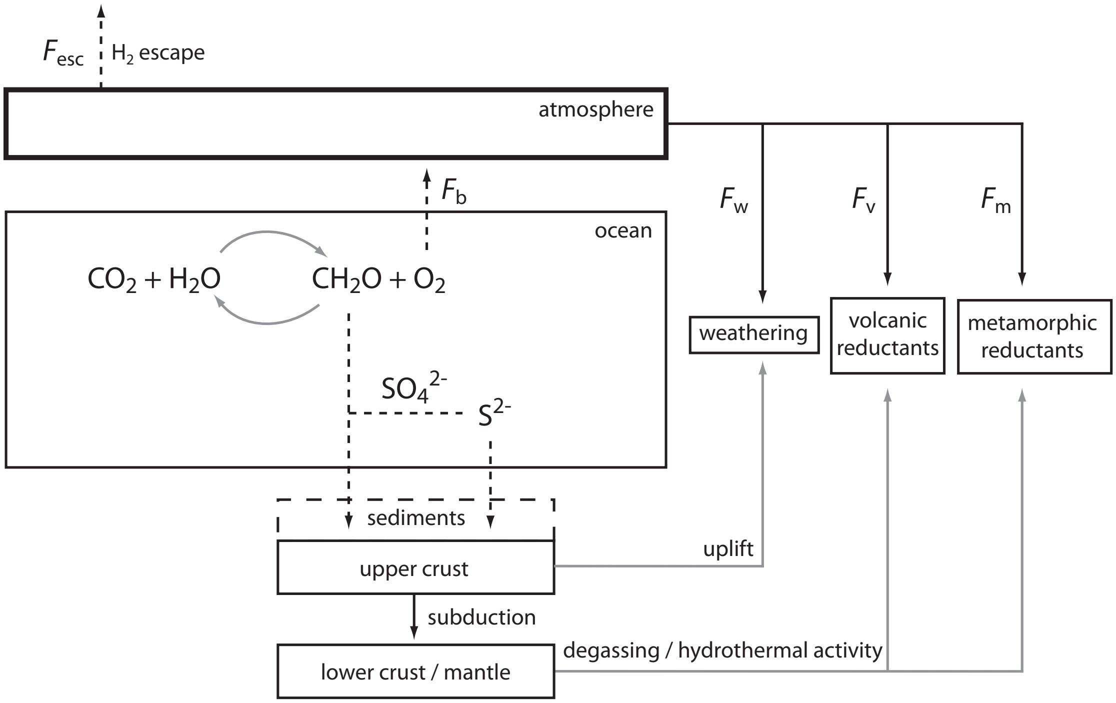

Figure 1.1. A schematic depiction of the global biogeochemical oxygen cycle. The photosynthesis-respiration subcycle is denoted by the grey curved arrows, and although this is localized within the ocean in the figure it also occurs extensively on the land surface of the modern Earth. The burial of organic matter and sedimentary pyrite results in a net release of O_2 to the atmosphere (F_b), while the gradual escape of H_2 to space results in the accumulation of oxidizing equivalents at Earth's surface. Oxygen is consumed through respiration, oxidative weathering (F_w), and through reaction with volcanic (F_v) and metamorphic (F_m) reductants. See (*8*) for an excellent review.

In order for O_2 to accumulate in the atmosphere, however, there must be some imbalance between the rate at which is it produced biologically and the rate(s) at which it is consumed by other processes (Fig. 1.1). Indeed, if some of the organic carbon produced during oxygenic photosynthesis is not removed from the surface system before it is respired (or is not channeled through microbial sulfate reduction with the reducing equivalents buried as a constituent of sedimentary pyrite), no O_2 would persist at Earth's surface regardless of its biological production. As a result, the accumulation of significant quantities of O_2 in Earth's atmosphere is reliant on a concert of both *biological* and *geochemical* processes. An important corollary of this observation is that there may have been periods of Earth's history during which biological oxygen production was taking place but the Earth surface remained reducing. In other words, when constructing the narrative of biospheric oxygenation there are two primary tie points: (1) the evolution of oxygenic photosynthesis; and, (2) the accumulation of biologically produced O_2 in the atmosphere.

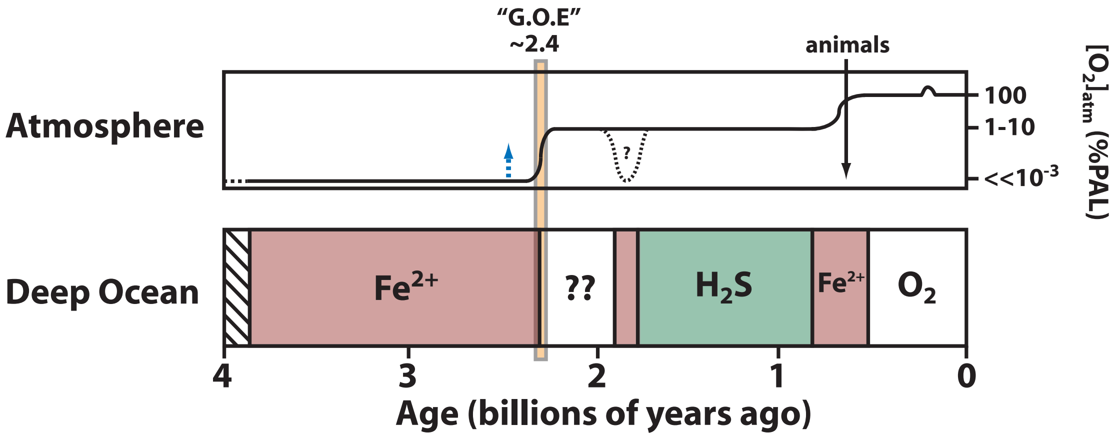

Figure 1.2. A schematic depiction of the evolution of atmosphere-ocean chemistry during Earth's history. The top panel shows estimates of atmospheric O_2 level relative to the Present Atmospheric Level (PAL). The blue dashed arrow denotes possible accumulation of O_2 prior to the 'Great Oxidation Event' (G.O.E.) at ~2.4 billion years ago (Ga; *9-12*). The dotted portion of the curve shows a possible drop in atmospheric O_2 at ~1.8 Ga (*13*). The figure is after (*14*), but is a summary of many decades of work. See (*15-17*) (and references therein) for very elegant and much more detailed treatments of this evolutionary trajectory.

It has been appreciated for some time (e.g., *18*) that the Earth's surface has become progressively more oxidizing with time, and although there are notable exceptions to this view (*19, 20*) it is now widely held that the oxygenation of the atmosphere took place during two geologically rapid periods at the beginning and end of the Proterozoic Eon (Fig. 1.2). However, when biological oxygen production emerged is much more obscure. Tenable estimates range over nearly a billion years, from the timing of the earliest sedimentary record (*21*) to arguments that oxygenic photosynthesis evolved coincident with the initial accumulation of O_2 in the atmosphere (*22, 23*). Superimposed on this evolution in atmospheric chemistry are progressive changes in ocean chemistry – the evolution of oceanic redox structure and the eventual ventilation of the deep ocean (Fig. 1.2).

This dissertation explores these issues from a variety of perspectives. In Chapter 2, empirical data on sedimentary iron (Fe) chemistry and multiple sulfur isotope systematics are used to suggest that evidence exists for the biological production and non-trivial accumulation of O_2 in Earth surface environments significantly prior to the conventionally accepted initial accumulation of O_2 in the atmosphere [often referred to as the 'Great Oxidation Event' (*24*)]. Chapter 3 explores the plausibility of oxygen accumulation in the surface ocean beneath a reducing atmosphere, and the notion that oxidative processing at Earth's surface prior to the Paleoproterozoic rise in atmospheric O_2 could have been localized within the shallow ocean. In Chapter 4, it is suggested on the basis of a simple isotope mass balance model that the isotopic signals used to establish the timing of atmospheric redox transitions in Earth's early history, which require an extremely reducing Earth surface, may be subject to a ‘crustal memory effect’ such that their long-term recycling would allow the maintenance of such isotopic signals despite potentially significant oscillations in atmospheric O_2. Finally, Chapter 5 explores the evolution of ocean chemistry after the initial accumulation of O_2 in the atmosphere, by combining an extensive trace metal database with a coupled mass balance approach.

References:

1. Xiong J, Fischer WM, Inoue K, Nakahara M, Bauer CE (2000) Molecular evidence for the early evolution of photosynthesis. *Science* **289**, 1724-1730.

2. Sagan C, Thompson WR, Carlson R, Gurnett D, Hord C (1993) A search for life on Earth from the Galileo spacecraft. *Nature* **365**, 715-721.

3. Rosenqvist J, Chasseféire E (1995) Inorganic chemistry of O_2 in a dense primitive atmosphere. *Planetary and Space Science* **43**, 3-10.

4. Catling DC, Glein CR, Zahnle KJ, McKay CP (2005) Why O_2 is required by complex life on habitable planets at the concept of planetary "oxygenation time". *Astrobiology* **5**, 415-438.

5. Hoganson CW, Babcock GT (1997) A metalloradical mechanism for the generation of oxygen from water in photosynthesis. *Science* **277**, 1953-1956.

6. van Rotterdam BJ, Crielaard W, van Stokkum IHM, Hellingwerf KJ, Westerhoff HV (2002) Simplicity in complexity: the photosynthetic reaction center performs as a simple 0.2 V battery. *FEBS Letters* **510**, 105-107.

7. Hohmann-Marriott MF, Blankenship RE (2011) Evolution of photosynthesis. *Annual Review of Plant Biology* **62**, 515-548.

8. Catling DC, Claire MW (2005) How Earth's atmosphere evolved to an oxic state: A status report. *Earth and Planetary Science Letters* **237**, 1-20.

9. Kaufman AJ, Johnston DT, Farquhar J, Masterson AL, Lyons TW, Bates S, Anbar AD, Arnold GL, Garvin J, Buick R (2007) Late Archean biospheric oxygenation and atmospheric evolution. *Science* **317**, 1900-1903.

10. Anbar AD, Duan Y, Lyons TW, Arnold GL, Kendall B, Creaser RA, Kaufman AJ, Gordon GW, Scott C, Garvin J, Buick R (2007) A whiff of oxygen before the Great Oxidation Event? *Science* **317**, 1903-1906.

11. Garvin J, Buick R, Anbar AD, Arnold GL, Kaufman AJ (2009) Isotopic evidence for an aerobic nitrogen cycle in the lastest Archean. *Science* **323**, 1045-1048.

12. Reinhard CT, Raiswell R, Scott C, Anbar AD, Lyons TW (2009) A late Archean sulfidic sea stimulated by early oxidative weathering of the continents. *Science* **326**, 713-716.

13. Frei R, Gaucher C, Poulton SW, Canfield DE (2009) Fluctuations in Precambrian atmospheric oxygenation recorded by chromium isotopes. *Nature* **461**, 250-253.

14. Lyons TW, Reinhard CT (2009) Early Earth: Oxygen for heavy-metal fans. *Nature* **461**, 179-181.

15. Holland HD (1984) *The Chemical Evolution of the Atmosphere and Oceans*. Princeton University Press, Princeton, NJ.

16. Canfield DE (2005) The early history of atmospheric oxygen: Homage to Robert M. Garrels. *Annual Review of Earth and Planetary Sciences* **33**, 1-36.

17. Farquhar J, Zerkle AL, Bekker A (2011) Geological constraints on the origin of oxygenic photosynthesis. *Photosynthesis Research* **107**, 11-36.

18. Nursall JF (1959) Oxygen as a prerequisite to the origin of the metazoa. *Nature* **183**, 1170-1172.

19. Ohmoto H (1997) When did the Earth's atmosphere become oxic? *Geochemical News* **93**, 12-27.

20. Ohmoto H, Watanabe Y, Ikemi H, Poulson SR, Taylor BE (2006) Sulphur isotope evidence for an oxic Archaean atmosphere. *Nature* **442**, 908-911.

21. Rosing MT, Frei R (2004) U-rich Archaean sea-floor sediments from Greenland – indications of >3700 Ma oxygenic photosynthesis. *Earth and Planetary Science Letters* **217**, 237-244.

22. Kopp RE, Kirschvink JL, Hilburn IA, Nash CZ (2005) The Paleoproterozoic snowball Earth: A climate disaster triggered by the evolution of oxygenic photosynthesis. *Proceedings of the National Academy of Sciences USA* **102**, 11131-11136.

23. Kirschvink JL, Kopp RE (2008) Palaeoproterozoic ice houses and the evolution of oxygen-mediating enzymes: the case for a late origin of photosystem II. *Philosophical Transactions of the Royal Society B* **363**, 2755-2765.

24. Holland HD (2002) Volcanic gases, black smokers, and the Great Oxidation Event. *Geochimica et Cosmochimica Acta* **66**, 3811-3826.

CHAPTER 2

A LATE ARCHEAN SULFIDIC SEA STIMULATED BY EARLY OXIDATIVE WEATHERING OF THE CONTINENTS

Preface:

The contents of this chapter have been published in modified form as:

> Reinhard, C.T., Raiswell, R., Scott, C., Anbar, A.D., and Lyons, T.W. 2009. A late Archean sulfidic sea stimulated by early oxidative weathering of the continents. Science. **326**: 713-716.

Introduction:

Iron speciation data for the late Archean Mt. McRae Shale provide evidence for a euxinic (anoxic and sulfidic) water column 2.5 billion years ago (Ga). Sulfur isotope data compiled from the same stratigraphic section suggest that euxinic conditions could have been stimulated by an increase in oceanic sulfate concentrations attendant to oxidative weathering of sulfide minerals under an O_2-poor atmosphere. Variability in local organic matter flux likely confined euxinic conditions to mid-portions of the water column on the basin margin. These findings challenge the notion that Earth's deep oceans remained continuously and pervasively iron-rich until 1.8 Ga and indicate that euxinic conditions may have been common on a variety of spatial and temporal scales both prior to and immediately following the rise in atmospheric oxygen.

Main Article:

The first two billion years of Earth's history were characterized by little to no free atmospheric oxygen (*1, 2*). A large body of evidence points to a sharp rise in the concentration of atmospheric O_2 during the Paleoproterozoic between 2.45 and 2.32 Ga (*1-3*), but the history of deep ocean oxygenation is less well known. The deposition of banded iron formations (BIF) during the Archean and early Proterozoic (~3.8 – 1.8 Ga) has been taken to imply that deep ocean water masses were anoxic and rich in dissolved ferrous iron (Fe^{2+}) derived from high temperature weathering of seafloor basalt under low oceanic sulfate (SO_4^{2-}) concentrations (*4, 5*). Reducing and iron-rich (ferruginous) deep ocean conditions are thought to have persisted for most of Earth's early history, although a relative paucity of BIF between 2.4 – 2.0 Ga (*6*) has rendered deep ocean chemistry during this period obscure. In any case, the cessation of BIF deposition at ~1.8 Ga is generally linked to the accumulation of oxygen in the atmosphere through the eventual removal of Fe^{2+} from the ocean either as ferric (hydr)oxides (*7*) or as pyrite in euxinic basins (*8*). A corollary of the latter model is that oxidative delivery of sulfate to the ocean was not sufficient to remove reactive iron, via microbial sulfide production, before ~1.8 Ga. However, recent studies of the late Archean Mt. McRae Shale suggest that oxidative sulfur cycling may have preceded the Paleoproterozoic rise in atmospheric oxygen (*9*) and that conditions sufficient to authigenically enrich molybdenum (Mo) in marine sediments existed at ~2.5 Ga (*10*). On the modern Earth, significant enrichment of Mo into sediments occurs following the conversion of soluble molybdate (MoO_4^{2-}) to particle-reactive thiomolybdates ($MoO_{4-x}S_x^{2-}$) in stable sulfidic environments (*11*), indicating that the Mo enrichments seen in the Mt. McRae Shale may have resulted from the development of a euxinic water column in association with increased oxidative transport of crustal sulfur as SO_4^{2-}.

In order to examine the possibility of euxinia during the late Archean, we analyzed iron mineral speciation in the Mt. McRae Shale (*12*). The distribution of iron among different biogeochemically labile mineral phases ('highly reactive iron') can reveal local redox conditions (*13, 14*). Highly reactive iron (Fe_{HR}) is defined as the sum of pyrite iron (Fe_{PY}) and iron in phases that are reactive to hydrogen sulfide (H_2S) on short diagenetic timescales, such as ferric oxides (Fe_{ox}), magnetite (Fe_{mag}), and iron present as carbonate (Fe_{carb}). In modern sediments from oxic continental margins and the deep-sea, Fe_{HR} comprises 6-38% of the total sedimentary iron (i.e., Fe_{HR}/Fe_T = 0.06-0.38); an average Fe_{HR}/Fe_T ratio of 0.26 ± 0.08 defines the modern siliciclastic baseline (*13*). Values for Fe_{HR}/Fe_T that are elevated above this siliciclastic background suggest reactive iron input that is decoupled from detrital sources, an indication of iron transport and scavenging within an anoxic water column (*15*). We also look toward total iron enrichments (expressed as Fe_T/Al ratios) as an indicator of water column anoxia (*16, 17*).

If Fe_{HR}/Fe_T and Fe_T/Al data provide evidence for anoxia, the ratio Fe_{PY}/Fe_{HR} can be used to distinguish between anoxic but non-sulfidic conditions and anoxic water columns containing free H_2S (euxinic). This approach is based on the simple premise that under anoxic conditions dissolved Fe^{2+} and dissolved H_2S cannot coexist in abundance in solution because of the insolubility of iron sulfide phases, and therefore high values for Fe_{PY}/Fe_{HR} indicate H_2S-dominated water column chemistry. For confirmation, we also measured degree of pyritization (DOP) as a conservative indicator of iron-limited pyrite formation and euxinia (*12, 17*). The distribution of highly reactive Fe species in the Mt. McRae Shale is shown in Figure 2.1, along with Fe_T/Al, bulk molybdenum (Mo), and organic carbon (TOC) concentrations from (*10*). We focus here on the pyritic and organic-rich lower shale interval (LSI) and upper shale interval (USI). Ferric oxides make up a small proportion of Fe_{HR} for the entire sequence analyzed here, indicating water column and/or pore fluid conditions that were reducing with respect to iron (Fig. 2.1). Values for Fe_{HR}/Fe_T and Fe_T/Al are elevated throughout, suggesting that the entire sequence was deposited beneath an anoxic water column. In a few instances, Fe_{PY}/Fe_{HR} values in the LSI approach a threshold ($Fe_{PY}/Fe_{HR} \geq 0.8$) interpreted to reflect euxinia when paired with evidence for anoxic deposition (*14, 19*); however, the average Fe_{PY}/Fe_{HR} for this unit (0.55±0.20) suggests a predominance of ferruginous conditions. Variations in Fe_{HR} within the LSI are governed by differences in Fe_{carb} rather than Fe_{PY} (Fig. 2.S2). These data are consistent with sulfate reduction and pyrite formation within or beneath an anoxic water column, but with reactive Fe in excess of dissolved H_2S such that H_2S did not persist in the pore fluids or water column during LSI deposition.

The USI shows pronounced enrichment in Fe_{HR}, indicating extensive reactive Fe scavenging beneath an anoxic water column (Fig. 2.1). Values for Fe_T/Al, although lower than those seen in the LSI and the siderite-facies BIF underlying the upper shale, remain elevated. In contrast to the LSI, Fe_{PY}/Fe_{HR} values are persistently high (0.85±0.17), as is DOP (0.78±0.23). A strong linear relation between Fe_{HR} and Fe_{PY} for the USI (Fig. 2.S2) demonstrates that variations in the amount of Fe_{HR} are governed by differences in Fe_{PY}

content and that Fe$_{\text{HR}}$ is all but completely pyritized. This combination of parameters (elevated values for Fe$_{\text{HR}}$/Fe$_{\text{T}}$, Fe$_{\text{T}}$/Al, Fe$_{\text{PY}}$/Fe$_{\text{HR}}$, and DOP) indicates that the water column was euxinic for a substantial portion of USI deposition.

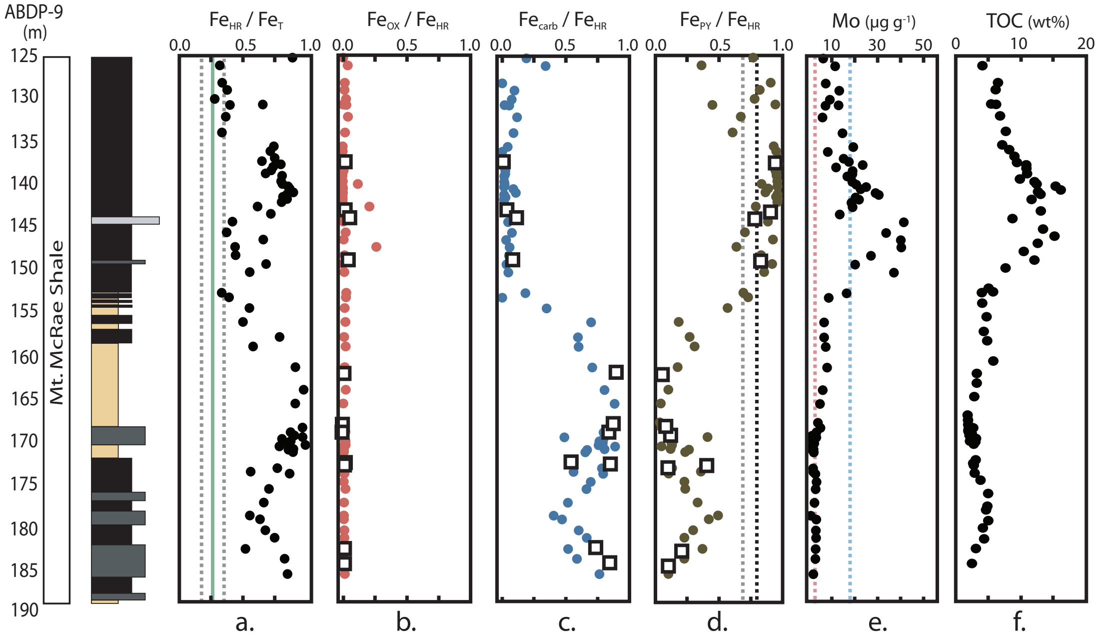

Figure 2.1. Stratigraphic profiles for iron speciation data from the ADBP-9 core. Filled symbols are the results of we chemical extractions, corrected according to the protocols presented in (*34*). Open symbols represent quantitative XRD results from (*34*). The dotted lines in (a) represent the range of Fe$_{\text{HR}}$/Fe$_{\text{T}}$ values seen in modern oxic continental margin and deep-sea sediments (*13*). The solid green line in (a) represents the mean Fe$_{\text{HR}}$/Fe$_{\text{T}}$ value (0.26) for normal (oxic) marine settings (*13*). The dotted lines in (d) represents Fe$_{\text{PY}}$/Fe$_{\text{HR}}$ values that are above 0.7 and 0.8. Euxinia is implied when both of these thresholds are exceeded and Fe$_{\text{T}}$/Al values exceed 0.5. The two dotted lines in (e) reflect average bulk Mo enrichments for the Archean (3 ppm; red) and Proterozoic (18 ppm; blue) (*18*). Data for (e) and (f) from (*10*).

To examine whether euxinia occurred in association with a transient or secular change in the oxidative transport of MoO_4^{2-} and SO_4^{2-} (*20*), we turn to the sulfur isotope composition of syngenetic and early diagenetic pyrite from deep-water facies (shales and BIF) of the Neoarchean-Paleoproterozoic (2.7-2.45 Ga) Hamersley Basin (Fig. 2.2).

Neoarchean samples below the USI, including those from the LSI and the siderite-facies BIF directly beneath the USI, show large $\Delta^{33}S$ values and positive covariation between $\Delta^{33}S$ and $\delta^{34}S$ (Fig. 2.2). This pattern has been hypothesized to reflect a primary atmospheric array in the isotopic composition of elemental sulfur aerosols (*21*). The corresponding linearity and large positive $\Delta^{33}S$ anomalies of these data suggest a tight isotopic coupling between atmospherically derived reduced sulfur species and sedimentary pyrite formation and also indicate that the transfer and mixing mechanisms that contributed to the signal ultimately preserved in the sediments were similar on at least a basinal scale and through large periods of Archean time (*9, 21*).

The sulfur isotope composition of pyrite in the USI and the overlying Brockman BIF shows a different distribution (Fig. 2.2). Values for $\Delta^{33}S$ are attenuated during euxinic deposition, with the largest positive $\Delta^{33}S$ values in the USI found in intervals that are transitional with the siderite-facies BIF unit below or the overlying carbonate unit. The linear array that characterizes the data prior to deposition of the USI is no longer evident, and a linear regression through the USI/Brockman data is closely aligned with the mass-dependent fractionation array in $\delta^{34}S$ - $\delta^{33}S$ space. This shift is accompanied by predominantly small negative $\Delta^{33}S$ values and relatively depleted $\delta^{34}S$ values within the USI followed by subdued variability in $\Delta^{33}S$ and a wide spread in $\delta^{34}S$ values (from -5‰ to +35‰) in the overlying Brockman BIF. We interpret this isotopic shift to reflect increased SO_4^{2-} availability during deposition of the USI and Brockman BIF accompanied by mixing of photolytically produced sulfur and isotopically normal crustal sulfur oxidatively mobilized under an atmosphere that remained O_2-poor (*12*). A transient or secular increase in the oxidative transport of MoO_4^{2-} and SO_4^{2-} during USI deposition is also supported by the contrasting strong non-mass-dependent (NMD) signal (*21*) and essential lack of Mo enrichment (*18*) preserved in pyritic shales of the Jeerinah Fm. underlying the Mt. McRae – analogous to the signals seen in the LSI and the siderite-facies BIF beneath the USI. The persistence of distinct NMD anomalies, despite the overall shift in isotopic arrays, requires the formation and burial of sulfur with NMD isotope composition throughout this period. Ground-level atmospheric O_2 concentrations of less than 2 ppmv (i.e., below 10^{-5} the present atmospheric level) are therefore implied (*27*), and concentrations throughout most of the troposphere may have been substantially lower than this (*27, 28*). This assertion is also supported by $\Delta^{33}S/\Delta^{36}S$ relationships (*9*).

Combined, the high-resolution Fe speciation, Mo enrichment, and sulfur isotope data for the Mt. McRae Shale indicate the development of euxinia during deposition of the USI and that these conditions were contemporaneous with a change in sedimentary sulfur isotope systematics. However, the stratigraphic position of the USI, which is interbedded on a meter scale with the underlying siderite facies BIF near their contact and is conformably overlain by the Brockman BIF, coupled with Fe_T/Al ratios that are persistently and significantly elevated above crustal values (Fig. 2.1), suggest that hydrothermal iron fluxes to the deep basin were important at this time. Our interpretation therefore implies a water column structure that would allow for both the accumulation of dissolved H_2S and the subsequent or coeval deposition of voluminous BIF.

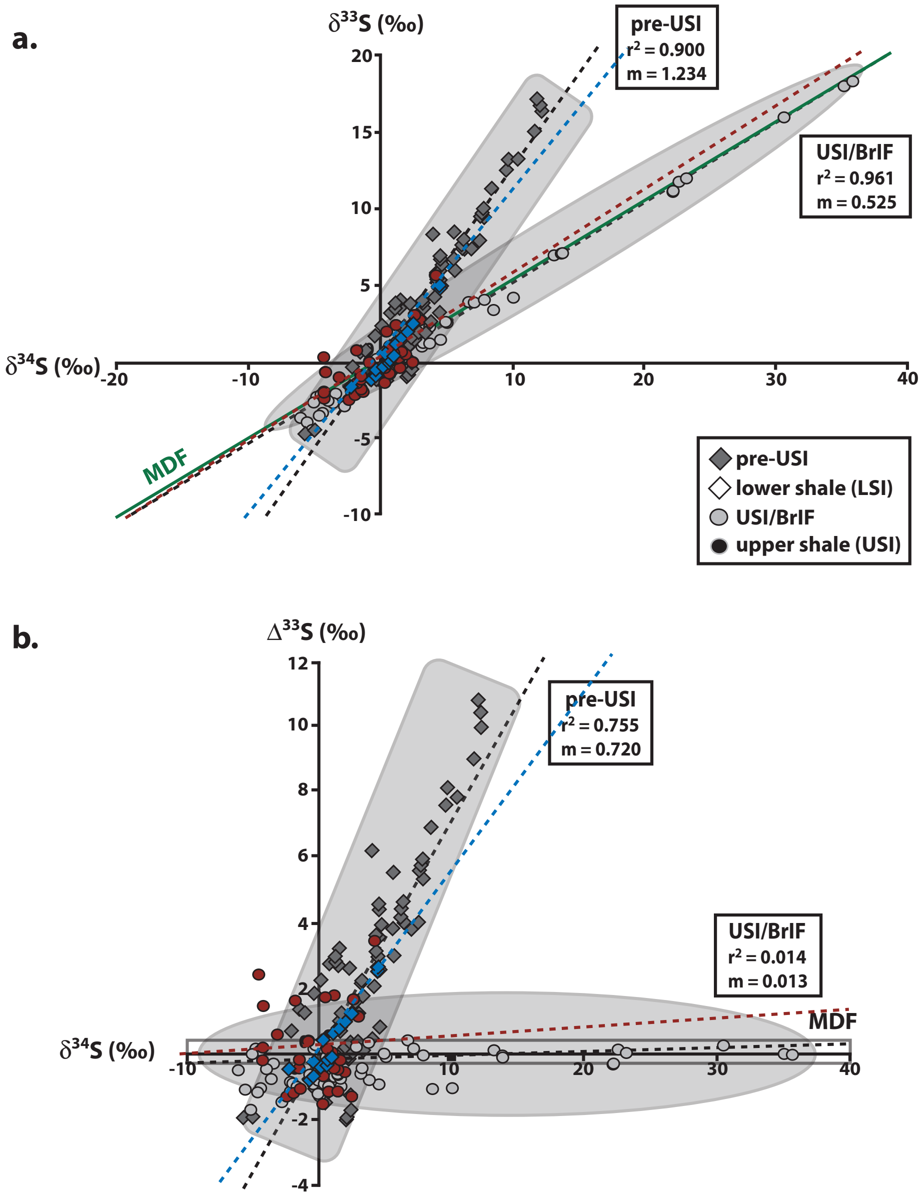

Figure 2.2. Sulfur isotope data for deep water Hamersley Basin pyrite samples spanning 2.7 to 2.46 Ga, displayed as δ^{34}S vs. δ^{33}S (a) and δ^{34}S vs. Δ^{33}S (b). Pre-USI data are from the Jeerinah Formation and lower Mt. McRae Shale (*21, 22*); the LSI and siderite-facies BIF beneath the USI (*9*); and the Marra Mamba BIF (*22*), which was deposited between the Jeerinah Fm. and the Mt. McRae Shale. USI/Post-USI data are from the USI (*9*) and the overlying Brockman BIF (BrIF) (*22, 23*). The line labeled 'MDF' in (a) is the mass-dependent fractionation line, defined as $\delta^{33}S = 0.515 * \delta^{34}S$ (*24*). The grey box in (b) represents the range of Δ^{33}S values attainable by mass-dependent processes (*25, 26*).

To reconcile these observations, we postulate locally enhanced microbial H_2S production, stimulated by organic matter (OM) delivery and facilitated by an increased flux of dissolved SO_4^{2-} to the basin. Local loading of OM would have fueled vigorous sulfate reduction along the basin margin, resulting in an oxidant minimum zone in which dissolved H_2S accumulated and quantitatively removed dissolved Fe^{2+} from the water column (Fig. 2.3). Euxinia would have expanded or contracted periodically as a function of the balance between reactive Fe input and OM flux, with the possibility of dissolved H_2S transiently accumulating on a basin scale or receding beneath the sediment-water interface. This lateral redox structure is similar to the basin-scale lithofacies framework hypothesized for contemporaneous strata from the South African Transvaal basin (*30*), indicating that such conditions may have been common during this period.

Although OM delivery was the proximate cause of euxinia, we propose that it was the increased availability of SO_4^{2-} attendant to oxidative weathering that ultimately allowed microbial H_2S production to overwhelm reactive Fe, at least locally, during USI deposition. Elevated total sulfur concentrations in this interval, coincident with significant increases in TOC and high Fe_T values (*9, 10*), also point to increasing availability of water column SO_4^{2-} such that microbial sulfate reduction was able to keep pace with substantial OM flux and relatively high reactive Fe availability. It is possible that mid-water column euxinia existed subsequent to USI deposition, with the stratigraphic transition to Brockman BIF recording a change in water depth rather than a temporal change in basin chemistry.

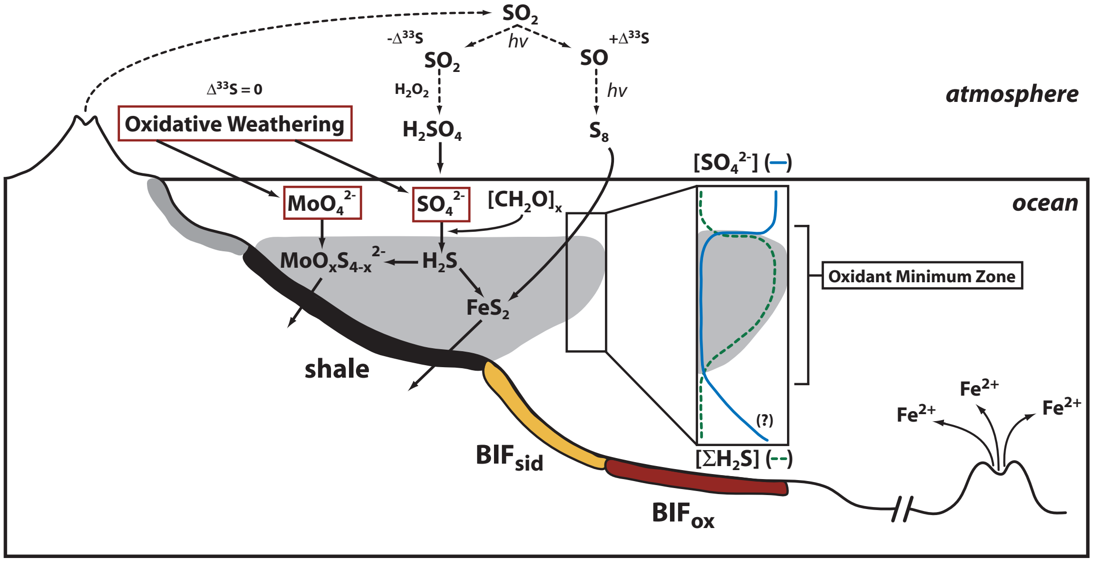

Figure 2.3. Schematic representation of the Hamersley Basin during the deposition of the upper Mt. McRae Shale (USI). Oxidative delivery of SO_4^{2-} and MoO_4^{2-}, combined with a high local organic matter flux, resulted in the accumulation of free H_2S in the water column in excess of dissolved Fe^{2+} (euxinia), supporting authigenic Mo enrichment. Atmospheric O_2 concentrations below 2 ppmv could have driven the enhanced oxidative weathering recorded in the USI but would still have allowed for SO_2 photolysis and the preservation of NMD sulfur isotope anomalies (*12*). Atmospheric photochemistry simplified from (*29*).

Our findings suggest that weak oxidative forcing could have stimulated the development of euxinia 50-100 million years before the Paleoproterozoic rise in atmospheric oxygen and that stable and persistent euxinia could have developed at least locally, and perhaps on a much larger scale, even within BIF-forming basins. Sulfur isotope data indicate that the weathering flux of SO_4^{2-} to the ocean increased substantially following the rise in atmospheric oxygen between 2.45 and 2.32 Ga (*8, 31*). The lack of BIF between 2.4 and 2.0 Ga may therefore reflect the frequent or sustained development of euxinia within Paleoproterozoic basins (*1*), presaging the possibly widespread and protracted development of similar oceanographic conditions hypothesized previously for the Mesoproterozoic (~1.8 – 1.0 Ga) (*8*). Constraints on deep ocean redox during this intervening period are sparse, but existing data intimate that euxinic deep basins were much more common than ferruginous ones between 2.4 and 2.0 Ga (*18*).

More generally, we argue that deposition of BIFs represented episodic pulses of reducing power from Earth's interior (*6*) rather than persistent deepwater conditions. Significant spatial variability in water column chemistry is indicated for intervals of BIF deposition, with intervening periods throughout the Archean and Paleoproterozoic during which at least portions of the water column may have been euxinic. Vacillation between euxinic and ferruginous conditions would have favored the early evolution and ecological expansion of a variety of anoxygenic photosynthetic metabolisms in pelagic environments, presaging the evolution of oxygenic photosynthesis (*32*). Expressions of biological oxygen production (such as those seen in the upper Mt. McRae and Brockman BIF) would then have varied with the extent to which episodic or sustained pulses of reductants from the Earth's interior would have buffered photosynthetic oxygen, contributing to the protracted nature of Earth surface oxygenation during the Archean and Proterozoic (*33*).

Supplementary Information:

Geological Setting:

Drill core ABDP-9 intersects a well-preserved, laminated interval of mixed lithologies that accumulated below wave base and experienced only mild regional metamorphism (prehnite-pumpellyite facies to <300ºC) (*9*, *10*). The Mt. McRae Shale, the focus of this study, is underlain stratigraphically by the Mt. Sylvia Formation and is overlain by the Dales Gorge Member of the Brockman Iron Formation (Fig. 2.S1). The uppermost portion of the ABDP-9 core consists of carbonate with gray/black shale interbeds, which grade down core into pyritic carbonaceous shale interbedded with organic-rich marl and ~20 m of pyritic black shale (the upper shale interval or USI). This carbonaceous shale interval contains, on average, 4.3 weight % (wt%) pyrite sulfur and 9.1 wt% total organic carbon (TOC) (*9*, *10*). The dominant lithology changes down core at ~155m, passing from black pyritic shale into siderite-facies banded iron formation (BIF). Below 173m, the lithology transitions again into black pyritic shale interbedded with carbonate/marl. This lower shale interval (LSI) is also rich in pyrite sulfur and TOC, averaging 2.5 wt% and 3.9 wt%, respectively (*9*, *10*).

All three facies are consistent with reducing bottom waters during deposition (anoxic and iron-rich [ferruginous] or anoxic and sulfidic [euxinic]) and the pyritic shale units also suggest extensive sedimentary sulfate reduction and the potential for sulfidic pore fluids and/or bottom waters. We sampled at 0.2m to 2m intervals for high-resolution analysis of sulfur isotopes (*9*), trace-metal content (*10*), and Fe-speciation analysis (this study). The latter was undertaken to further explore the possibility of euxinic (anoxic and sulfidic) conditions. Sampling specifically avoided pyrite nodules and prominent pyrite laminae, as these are likely to skew Fe speciation results away from primary depositional chemistry. Such features are most abundant near the top of the USI transitioning into the overlying carbonate and are not present within the interval of extended euxinia discussed in the main text.

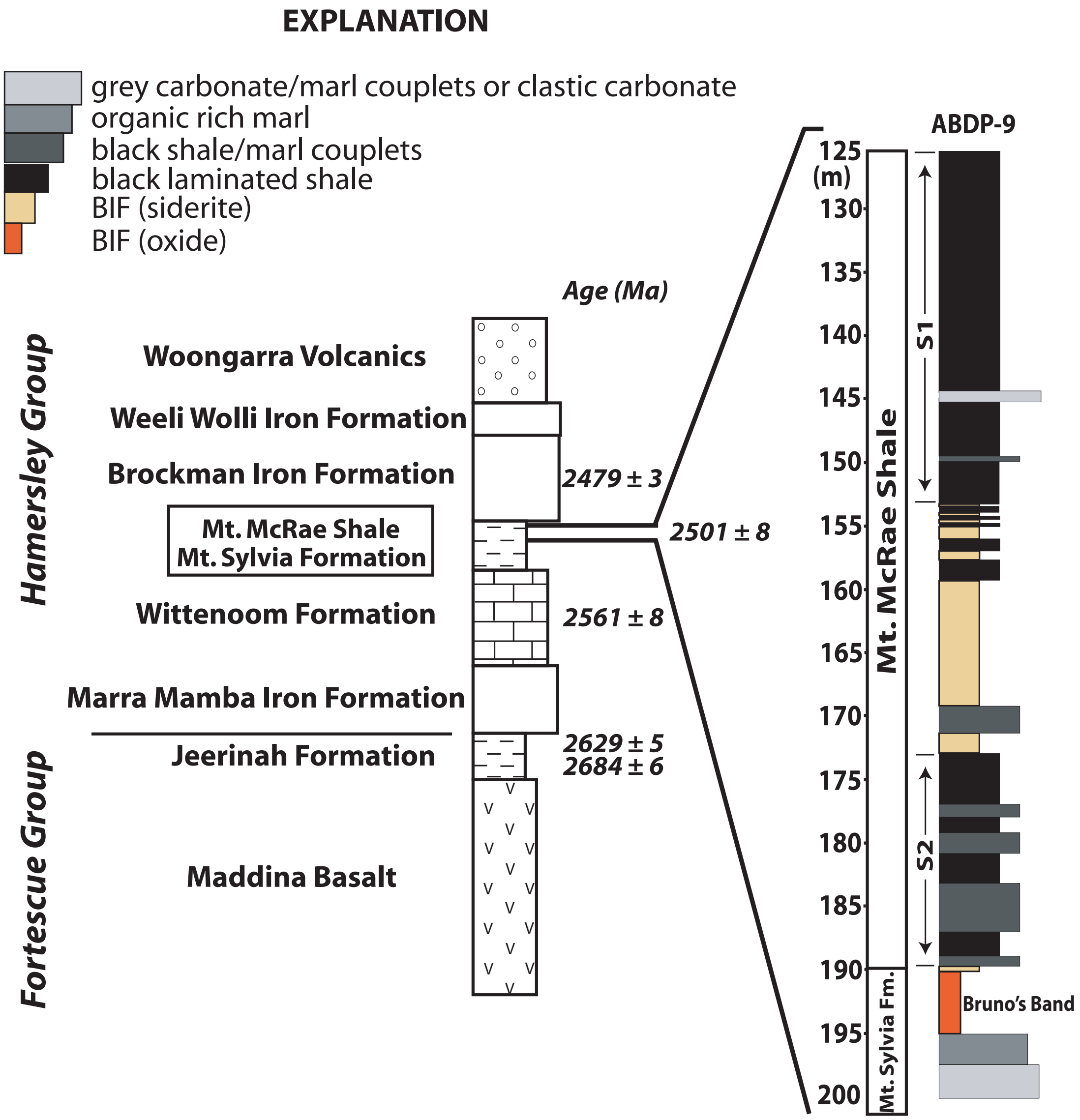

Figure 2.S1. Stratigraphic column highlighting the Mt. McRae Shale. Stratigraphic details for the Fortescue and Hamersley groups and available dates are from (*40*). The detailed stratigraphy of the Mt. McRae Shale is from (*9*). The upper Mt. McRae Shale yields a Re-Os age of 2501.1±8.2 Mya (*10*), consistent with previous age estimates.

Analytical Methods:

The speciation of highly reactive iron (Fe_{HR}), which comprises pyrite iron and other iron phases that will react with sulfide to form pyrite in the water column or during early diagenesis, was obtained via a calibrated sequential extraction protocol (*14*, *35*). Briefly, ~100 mg of sample powder was first treated with a buffered sodium acetate solution, which extracts carbonate-associated Fe (either siderite, ferroan calcite, and/or the dolomite-ankerite solid solution series). This fraction is here referred to as Fe_{carb}. Samples were then treated with a sodium dithionite solution. Fe obtained from this extraction step, here referred to as Fe_{ox}, consists of "reducible" iron oxide phases, or iron oxides such as goethite and hematite that are reactive to hydrogen sulfide (H_2S) on early diagenetic timescales. Magnetite, a mixed-valence iron oxide that does not react with dithionite, was extracted with an ammonium oxalate solution. Sequential extracts were analyzed on an Agilent 7500ce ICP-MS after 100-fold dilution in trace-metal grade 2% HNO_3. Pyrite iron was calculated (assuming a stoichiometry of FeS_2) based on wt% sulfur extracted during a two hour hot chromous chloride distillation followed by iodometric titration (*36*).

The total amount of highly reactive iron, or Fe_{HR}, is defined as $Fe_{HR} = Fe_{carb} + Fe_{ox} + Fe_{mag} + Fe_{PY}$. Data are reported as the ratio of a particular reactive Fe phase to the total amount of highly reactive Fe (e.g., Fe_{carb} / Fe_{HR}). Analytical data are detailed in Table S1. We note that a previous study of Fe speciation in the Mt. McRae Shale (*14*) did not find evidence for sulfidic conditions. However, this study was performed on different core material and was not performed at the same resolution and within the same detailed context, and so it is probable that these data record a period of Mt. McRae deposition that was not euxinic (i.e., analogous to the LSI or the siderite-facies BIF beneath the USI of this study). Sulfur isotope analyses are described in detail elsewhere (*9*, *21-23*).

As a complement to the sequential extraction data, we measured Degree of Pyritization (DOP), defined as:

$$\mathrm{DOP} = \frac{\mathrm{Fe_{PY}}}{\mathrm{Fe_{HCl}} + \mathrm{Fe_{PY}}}\ , \tag{2.1}$$

where $\mathrm{Fe_{HCl}}$ is iron extracted by boiling ~100 mg of sample powder for one minute in concentrated HCl (*37*) and measured using conventional spectrophotometric techniques (*38*). $\mathrm{Fe_{PY}}$ is determined as above. DOP provides a conservative estimate of the degree to which reactive Fe has been converted to pyrite because $\mathrm{Fe_{HCl}}$ includes some amount of poorly reactive silicate Fe that is unreactive with hydrogen sulfide even on very long timescales (*39*). In addition to detrital contributions, this fraction can include both authigenic iron-silicates formed during diagenesis and iron-silicates possibly formed at the expense of other highly reactive iron phases during metamorphism. Significantly elevated $\mathrm{Fe_T}$/Al values within the LSI and the siderite-facies BIF, combined with relatively low (though diagnostically anoxic) values for $\mathrm{Fe_{HR}}/\mathrm{Fe_T}$, may indicate that the $\mathrm{Fe_{HR}}$ extraction methodology is not complete for samples with unusually high concentrations of crystalline siderite. This relationship could also result from authigenic and/or metamorphic formation of Fe silicates. Because the DOP methodology quantitatively mobilizes siderite in addition to all other reactive Fe phases, as well as authigenic Fe silicates and a portion of other poorly reactive silicate phases (*39*), it ensures conservative assessment of euxinia. We note that, according to DOP values, the pattern that we observe does not change but becomes even more striking if there is indeed residual siderite missed by our Fe_{carb} extraction step.

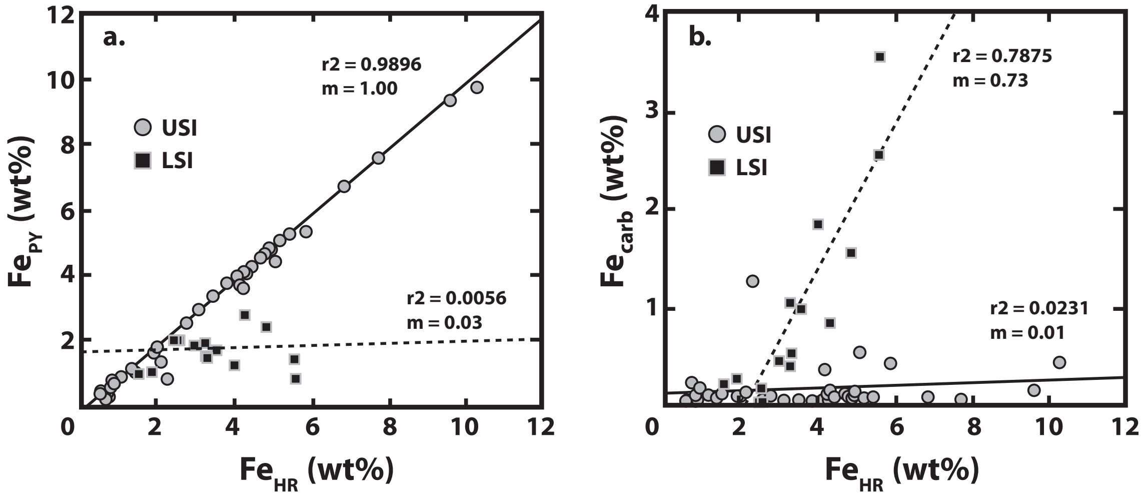

Figure 2.S2. (a) Pyrite iron (Fe_{PY}) and (b) carbonate iron (Fe_{carb}) relative to concentrations of highly reactive iron (Fe_{HR}) in the USI and LSI of the Mt. McRae Shale. In the USI, variations in Fe_{HR} result from variations in pyrite Fe content, with the regression slope suggesting virtually complete pyritization of Fe_{HR}. In the LSI, variations in Fe_{HR} more closely track variations in carbonate Fe, indicating reactive Fe in excess of dissolved sulfide during deposition.

Oxidative Mobilization of Crustal Sulfur Under Low Atmospheric pO_2:

The reactions governing the oxidative dissolution of pyrite in low-temperature aqueous environments can be summarized as (*40*, *41*):

$$FeS_2 + \frac{7}{2}O_2 + H_2O \rightarrow Fe^{2+} + 2SO_4^{2-} + 2H^+ \;, \tag{2.2}$$

$$Fe^{2+} + \frac{1}{4}O_2 + H^+ \rightarrow Fe^{3+} + \frac{1}{2}H_2O \;, \tag{2.3}$$

$$FeS_2 + 14Fe^{3+} + 8H_2O \rightarrow 15Fe^{2+} + 2SO_4^{2-} + 16H^+ \;. \tag{2.4}$$

The importance of O_2 in this process is thought to be tied more to the regeneration of Fe^{3+} (Eq. 2.3) than to direct oxidation of pyrite (Eq. 2.2). Indeed, this reaction is often thought of as the rate-limiting step in pyrite oxidation, particularly at low pH (*41*), and is necessary to sustain pyrite oxidation at circumneutral pH given the low solubility of Fe^{3+} under such conditions (*42*, *43*). Despite this apparent dependence on O_2, any process capable of catalyzing Fe^{3+} regeneration could, in principle, sustain oxidative dissolution of pyrite. One additional possibility, and importantly one that would not require environmental O_2, is anoxygenic photosynthetic Fe^{2+} oxidation (*44*). However, the standard electrode potentials of both the $Fe(OH)_3/Fe^{2+}$ and Fe^{3+}/Fe^{2+} couples increase sharply with decreasing pH and approach or exceed the midpoint potentials of known anoxygenic photosynthetic reaction centers below pH ~ 5 (*45-47*). Indeed, anoxygenic photosynthetic iron oxidizers studied to date tend to show optimum growth in a very narrow pH range of ~6.5-6.8 (*46*, *48*, *48*).

Although the buffering activity of silicates in terrestrial environments that support sulfide mineral oxidation is not very well understood (*50*), the timescales of sulfide oxidation and acidity generation are generally thought to be fast relative to the dissolution rates of crustal silicates (*50-52*), which should result in limited buffering capacity at the site of weathering. If we assume an Archean rainwater pH of ~ 4.7 [corresponding to a conservative estimate of atmospheric pCO_2 ~ 0.03 bar (*53*, *54*); but see (*55*)] and a crustal sulfide budget dominated by igneous granitic rocks, the local pH of the weathering environment would likely have been acidic, perhaps strongly so, rendering photosynthetic Fe^{2+} oxidation energetically unfavorable given available constraints. Although anaerobic

Fe^{2+} oxidation can also be coupled to reduction of nitrate (NO_3^-) (*56*, *57*) and Mn(IV)-oxides (*58*), both processes should require environmental O_2 to catalyze oxidant generation. We therefore conclude that the most parsimonious mechanism for regenerating Fe^{3+} and sustaining oxidative dissolution of pyrite is through reaction with environmental O_2.

Building on the approach used in (*10*), we further explore the plausibility of oxidation of crustal sulfides under an atmosphere still sufficiently reducing to support the production and preservation of NMD-S isotope anomalies ($pO_2 < 10^{-5}$ PAL; *27*). We use pyrite in the following calculations to represent igneous crustal sulfides owing to the availability of kinetic data (*40*, *59*). We follow the rate law (*40*):

$$r = 10^{-8.19(\pm 0.10)} \frac{m_{\mathrm{DO}}^{0.5(\pm 0.04)}}{m_{\mathrm{H^+}}^{0.11(\pm 0.01)}}\ , \tag{2.5}$$

where r is the pyrite destruction rate (mol m^{-2} s^{-1}). Dissolved oxygen (DO) concentrations in solution are estimated assuming equilibration of a weathering fluid with various values of atmospheric pO_2 using a Henry's Law constant (K_H) at 25ºC of 1.26 x 10^{-3} mol L^{-1} bar^{-1} (*60*). We assume that the meteoric environment where chemical weathering occurred was sufficiently dilute for Henry's Law to apply. We also assume that Earth's atmospheric pressure has remained constant. Although the oxidation kinetics are sensitive to changes in pH, doubling the temperature to 50ºC (i.e., $K_H = 9.32 \times 10^{-4}$ mol L^{-1} bar^{-1}) has a negligible effect. The calculations assume a cubic pyrite grain with a surface area of 6 x 10^4 μm, typical for fine-grained igneous sulfides.

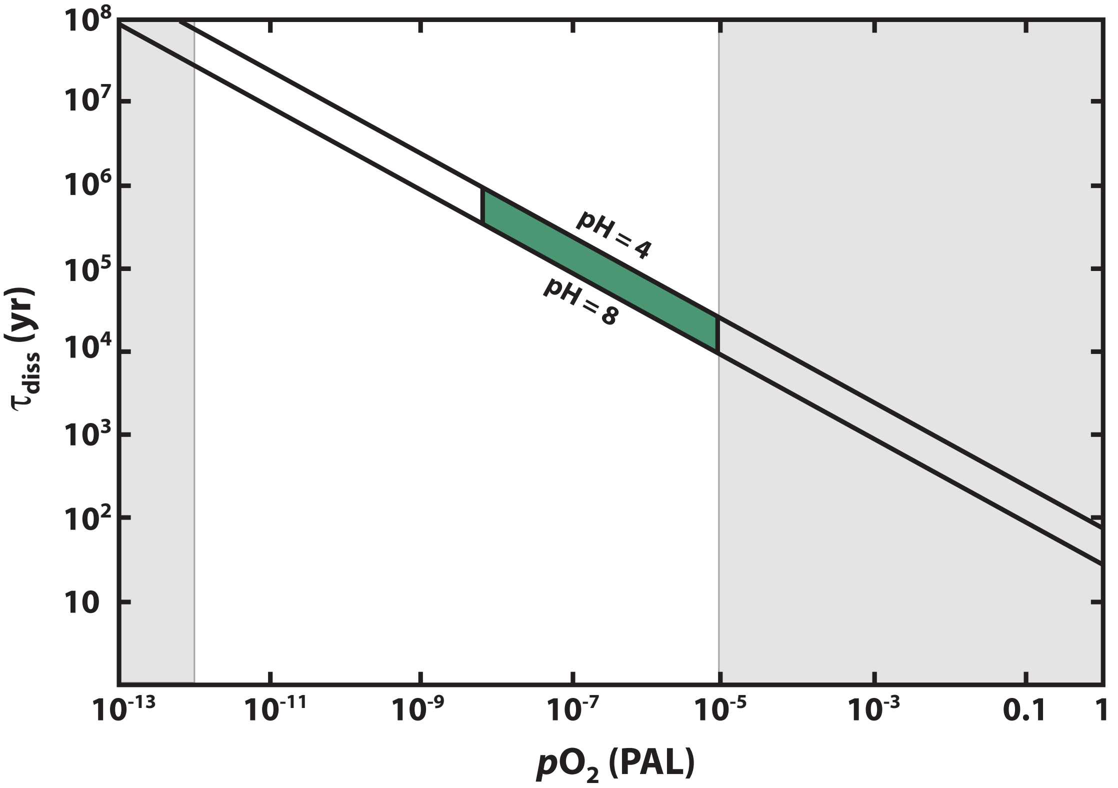

Figure 2.S3. Dissolution kinetics of a cubic pyrite crystal under various atmospheric oxygen concentrations and pH conditions. Systems supporting pyrite oxidation can have a wide range of pH values as a result of mineral buffering, but will likely be below neutral once sulfide oxidation has initiated (see text). The grey box encompasses one plausible range of atmospheric oxygen concentrations at ground level (~0.002 – 1ppmv) during deposition of the upper shale interval.

Figure 2.S3 shows the dissolution times of pyrite as a function of pO_2 and pH. At hypothesized prebiotic concentrations of atmospheric O_2 ($pO_2 < 10^{-13}$ PAL; *61*) pyrite dissolution is extremely slow (on the order of ~100 million to 1 billion years or more) regardless of pH. However, even at atmospheric O_2 concentrations below 10^{-5} PAL, a pyrite grain with a surface area of 6 x 10^4 μm will dissolve on timescales of tens of thousands of years. Given available constraints on the depositional time represented by

the USI (~10-15 million years; *10*), it is plausible that igneous continental sulfides would dissolve oxidatively at atmospheric oxygen concentrations of ~10^{-5}-10^{-8} PAL on timescales that are a small fraction of the shale's total duration (Fig. 2.S3). As pointed out in (*10*), these are lower limits because they neglect crystal defects and microbial activity, both of which would accelerate dissolution. In any case, the oxidative mobilization and delivery of sulfate and molybdate to the ocean during deposition of the USI would require biological oxygen production but could have reasonably occurred beneath an atmosphere with pO_2 still low enough to favor the production of preservation of NMD-S anomalies.

Sulfur Isotope Compilation:

We conclude that the USI captured a coupled oxidative pulse of MoO_4^{2-} and SO_4^{2-} to the Hamersley Basin. However, authigenic Mo enrichments require the accumulation of free H_2S as well as a source of dissolved Mo. It is therefore also possible that an oxidative source of MoO_4^{2-} and SO_4^{2-} existed prior to the deposition of the USI, and its geochemical expression was delayed by the persistence of ferruginous conditions and a lack of free H_2S. In order distinguish between these two scenarios, we examined the sulfur isotope composition of Hamersley Basin sulfides above and below the euxinic interval recorded in the USI. We hypothesized that a transient or secular change in the flux of isotopically normal crustal SO_4^{2-} as a result of oxidative weathering should result in the attenuation of non-mass-dependent (NMD) sulfur isotope anomalies still preserved in authigenic sulfides and that this could be coupled to an increased variability in $\delta^{34}S$ as a result of increased SO_4^{2-} availability.

Data for our sulfur isotope compilation derive from Hamersley Basin sulfides deposited between ~2700 and 2460 Ma in deep basinal sediments (shales and iron formations) (*9*, *21-23*). Data from (*21*) include samples from the Mt. McRae Shale, but these are grouped here with the "Pre-USI" data following the correlation presented in (*9*). Similarly, data from the lower Mt. McRae Shale of (*22*) are grouped with "Pre-USI" data. As discussed in the text, our target is the temporal pattern at relatively high resolution through the Neoarchean period of Hamersley Basin deposition.

Comparison of sulfur isotope systematics between basinal facies and shallow carbonate facies can be problematic because of depth-related heterogeneities in the isotopic composition of different reservoirs, particularly if seawater sulfate concentrations remained very low, and because the complexities of water column/diagenetic Fe-S cycling are less well understood for carbonates. Neoarchean carbonate environments are likely to display significant differences in Fe-S systematics relative to coeval shale and iron formation facies deposited in deep basinal environments as a function of reactive Fe limitation, sediment accumulation rate, and perhaps localized biological oxygen release (*62*, *63*). We therefore focus on deep basinal facies (laminated shales and iron formations) so that temporal isotopic changes are not obscured by differences in Fe-S systematics within markedly different depositional environments.

We note that some carbonate facies data overlying the USI display relatively large $\Delta^{33}S$ values (approaching 4‰ for samples with SF_6 constraints [*9*]) and occupy a space in the $\delta^{34}S$ – $\Delta^{33}S$ field that is unusual for Archean pyrites (*9*). These atypical samples have been interpreted previously to reflect multi-stage cycling of elemental sulfur during the initial widespread manifestation of the oxidative biological sulfur cycle within the surface ocean (*9*), and some of the larger $\Delta^{33}S$ values may suggest temporal fluctuations in the intensity of oxidative sulfate delivery. However, the dominantly mass-dependent signal preserved in the Brockman Iron Formation, combined with the essential lack of large $\Delta^{33}S$ values after ~2480 Ma, suggests that the sulfur isotope shift we observe was broadly unidirectional within the Hamersley Basin and perhaps globally. Again, because of such complications, we have focused our temporal comparison on like facies over a relatively narrow time interval.

Mesoarchean samples from the Hamersley Basin lying well below our intervals of interest have also been excluded because recent studies suggest that there is a significant change in sulfur isotope systematics related to variations in atmospheric transparency to UV (*64*), atmospheric oxidation state (*65*), or photochemical shielding of SO_2 by an atmospheric organic haze (*66*), among other possibilities (*67*). The decline in $\Delta^{33}S$ values during the Mesoarchean appears to be a robust empirical result but is not well understood. We therefore elected to focus on samples deposited in closer temporal association with the ABDP-9 material. Data from other Neoarchean basins were also not included because available age constraints do not allow for meaningful correlation at the stratigraphic resolution afforded by the ABDP-9 core and associated Hamersley Basin units. Their inclusion would also be peripheral to the primary purpose of the compilation – that is, to demonstrate increased and possibly sustained O_2-dependent delivery of continental sulfur during and following deposition of the USI relative to the subjacent strata.

Alternative Hypotheses for the Observed Sulfur Isotope Pattern:

Atmospheric photochemical models indicate that the magnitude of NMD-S anomalies should also be influenced by atmospheric CH_4 concentrations (*28*) and volcanic SO_2 outgassing rates (*21*, *68*). It is plausible, then, that the pattern we note for the late Archean Hamersley Basin resulted from either (1) a decrease in atmospheric CH_4 concentrations such that elemental sulfur aerosols could no longer be produced and exported efficiently from the troposphere or (2) a change in volcanic SO_2 outgassing rates occurred, which caused an attenuation in $\Delta^{33}S$ values. In the first case, the most obvious mechanism for a decrease in atmospheric CH_4 would be an increase in available oxidants (in particular SO_4^{2-}) that would either directly (through consumption; *69*) or indirectly (through competition for organic substrate; *70*) act as a negative feedback on biological CH_4 production. However, distinct NMD-S anomalies persist during and subsequent to the deposition of the USI, suggesting that the requisite tropospheric CH_4 concentrations for the generation of elemental sulfur aerosols were met and that atmospheric O_2 concentrations were still extremely low. Further, a decline in biogenic CH_4 flux to the atmosphere as a result of increased oceanic SO_4^{2-} concentrations would still be consistent with our overarching model (i.e., increased oxidative transport of crustal sulfur). In the second case, model predictions indicate that the magnitude of NMD-S anomalies generated in the atmosphere should vary directly with $p\mathrm{SO}_2$ as a function of varying rates of volcanic SO_2 outgassing (*68*). We can think of no reason to imagine a secular decrease in rates of volcanic SO_2 outgassing during the deposition of the USI and the overlying Brockman Fm. Indeed, this period is thought to correspond to the emplacement of subaerial (*33*) and submarine (*71*) large igneous provinces and the associated deposition of voluminous BIF, indicating that volcanic SO_2 outgassing rates, if variable, may have been elevated rather than attenuated.

References:

1. Canfield DE (2005) The early history of atmospheric oxygen: Homage to Robert M. Garrels. *Annual Review of Earth and Planetary Sciences* **33**, 1-36.

2. Holland HD (2002) Volcanic gases, black smokers, and the Great Oxidation Event. *Geochimica et Cosmochimica Acta* **66**, 3811-3826.

3. Bekker A, Holland HD, Wang P-L, Rumble III D, Stein HJ, Hannah JL, Coetzee LL, Beukes NJ (2004) Dating the rise of atmospheric oxygen. *Nature* **427**, 117-120.

4. Isley AE (1995) Hydrothermal plumes and the delivery of iron to Banded Iron Formation. *Journal of Geology* **103**, 169-185.

5. Kump LR, Seyfried Jr. WE (2005) Hydrothermal Fe fluxes during the Precambrian: Effect of low oceanic sulfate concentrations and low hydrostatic pressure on the composition of black smokers. *Earth and Planetary Science Letters* **235**, 654-662.

6. Isley AE, Abbott DH (1999) Plume-related mafic volcanism and the deposition of banded iron formation. *Journal of Geophysical Research* **104**, 15461-15477.

7. Cloud P (1972) A working model of the primitive Earth. *American Journal of Science* **272**, 537-548.

8. Canfield DE (1998) A new model for Proterozoic ocean chemistry. *Nature* **396**, 450-453.

9. Kaufman AJ, Johnston DT, Farquhar J, Masterson AL, Lyons TW, Bates S, Anbar AD, Arnold GL, Garvin J, Buick R (2007) Late Archean biospheric oxygenation and atmospheric evolution. *Science* **317**, 1900-1903.

10. Anbar AD, Duan Y, Lyons TW, Arnold GL, Kendall B, Creaser RA, Kaufman AJ, Gordon GW, Scott C, Garvin J, Buick R (2007) A whiff of oxygen before the Great Oxidation Event? *Science* **317**, 1903-1906.

11. Erickson BE, Helz GR (2000) Molybdenum(VI) speciation in sulfidic waters: Stability and lability of thiomolybdates. *Geochimica et Cosmochimica Acta* **64**, 1149-1158.

12. Methods and materials are detailed within Supporting Information.

13. Raiswell R, Canfield DE (1998) Sources of iron for pyrite formation in marine sediments. *American Journal of Science* **298**, 219-245.

14. Poulton SW, Fralick PW, Canfield DE (2004) The transition to a sulphidic ocean ~1.84 billion years ago. *Nature* **431**, 173-177.

15. Wijsman JWM, Middelburg JJ, Heip CHR (2001) Reactive iron in Black Sea Sediments: implications for iron cycling. *Marine Geology* **172**, 167-180.

16. Interpretation of this measurement follows the same rationale as that for Fe_{HR}/Fe_T [i.e., enrichments above the average Fe_T/Al ratio for continental crust of ~0.5 imply transport and scavenging of iron under anoxic conditions], but importantly Fe_T/Al is immune to concerns regarding authigenic iron-silicate formation or metamorphic repartitioning of reactive iron phases into poorly reactive silicate mineralogies.

17. Lyons TW, Severmann S (2006) A critical look at iron paleoredox proxies: New insights from modern euxinic marine basins. *Geochimica et Cosmochimica Acta* **70**, 5698-5722.

18. Scott C, Lyons TW, Bekker A, Shen Y, Poulton SW, Chu X, Anbar AD (2008) Tracing the stepwise oxygenation of the Proterozoic ocean. *Nature* **452**, 456-459.

19. Anderson TF, Raiswell R (2004) Sources and mechanisms for the enrichment of highly reactive iron in euxinic Black Sea sediments. *American Journal of Science* **304**, 203-233.

20. Because Mo enrichments require both an oceanic Mo reservoir and the accumulation of free H_2S, it is possible that the metal enrichments recorded in the USI point only to the development of euxinia rather than a temporally constrained increase in the flux of MoO_4^{2-} and SO_4^{2-} to the Hamersley Basin during USI deposition.

21. Ono S, Eigenbrode JL, Pavlov AA, Kharecha P, Rumble III D, Kasting JF, Freeman KH (2003) New insights into Archean sulfur cycle from mass-independent sulfur isotope records from the Hamersley Basin, Australia. *Earth and Planetary Science Letters* **213**, 15-30.

22. Partridge MA, Golding SD, Baublys KA, Young E (2008) Pyrite paragenesis and multiple sulfur isotope distribution in late Archean and early Paleoproterozoic Hamersley Basin sediments. *Earth and Planetary Science Letters* **272**, 41-49.

23. Mojzsis SJ, Coath CD, Greenwood JP, McKeegan KD, Harrison TM (2003) Mass-independent isotope effects in Archean (2.5 to 3.8 Ga) sedimentary sulfides determined by ion microprobe analysis. *Geochimica et Cosmochimica Acta* **67**, 1635-1658.

24. Hulston JR, Thode HG (1965) Variations in the S^{33}, S^{34}, and S^{36} contents of meteorites and their relation to chemical and nuclear effects. *Journal of Geophysical Research* **70**, 3475-3484.

25. Farquhar J, Johnston DT, Wing BA, Habicht KS, Canfield DE, Airieau S, Thiemens MH (2003) Multiple sulphur isotopic interpretations of biosynthetic pathways: implications for biological signatures in the sulphur isotope record. *Geobiology* **1**, 27-36.

26. Ono S, Wing B, Johnston D, Farquhar J, Rumble D (2006) Mass-dependent fractionation of quadruple stable sulfur isotope system as a new tracer of sulfur biogeochemical cycles. *Geochimica et Cosmochimica Acta* **70**, 2238-2252.

27. Pavlov AA, Kasting JF (2002) Mass-independent fractionation of sulfur isotopes in Archean sediments: Strong evidence for an anoxic Archean atmosphere. *Astrobiology* **2**, 27-41.

28. Zahnle K, Claire M, Catling D (2006) The loss of mass-independent fractionation in sulfur due to a Palaeoproerozoic collapse of atmospheric methane. *Geobiology* **4**, 271-283.

29. Kasting JF, Zahnle KJ, Pinto JP, Young AT (1989) Sulfur, ultraviolet radiation, and the early evolution of life. *Origins of Life and Evolution of the Biosphere* **19**, 95-108.

30. Klein C, Beukes NJ (1989) Geochemistry and sedimentology of a facies transition from limestone to iron-formation deposition in the early Proterozoic Transvaal Supergroup, South Africa. *Economic Geology* **84**, 1733-1774.

31. Cameron EM (1982) Sulphate and sulphate reduction in early Precambrian oceans. *Nature* **296**, 145-148.

32. Xiong J, Fischer WM, Inoue K, Nakahara M, Bauer CE (2000) Molecular evidence for the early evolution of photosynthesis. *Science* **289**, 1724-1730.

33. Kump LR, Barley ME (2007) Increased subaerial volcanism and the rise of atmospheric oxygen 2.5 billion years ago. *Nature* **448**, 1033-1036.

34. Raiswell R, Reinhard CT, Derkowski A, Owens J, Bottrell SH, Anbar AD, Lyons TW (2011) Formation of syngenetic and early diagenetic iron minerals in the late Archean Mt. McRae Shale, Hamersley Basin, Australia: New insights on the patterns, controls and paleoenvironmental implications of authigenic mineral formation. *Geochimica et Cosmochimica Acta* **75**, 1072-1087.

35. Poulton SW, Canfield DE (2005) Development of a sequential extraction procedure for iron: implications for iron partitioning in continentally derived particulates. *Chemical Geology* **214**, 209-221.

36. Canfield DE, Raiswell R, Westrich JT, Reaves CM, Berner RA (1986) The use of chromium reduction in the analysis of reduced inorganic sulfur in sediments and shales. *Chemical Geology* **54**, 149-155.

37. Raiswell R, Buckley R, Berner RA, Anderson TF (1988) Degree of pyritization of iron aas a paleoenvironmental indicator of bottom-water oxygenation. *Journal of Sedimentary Petrology* **58**, 812-819.

38. Stookey LL (1970) Ferrozine – A new spectrophotometric reagent for iron. *Analytical Chemistry* **42**, 779-781.

39. Raiswell R, Canfield DE, Berner RA (1994) A comparison of iron extraction methods for the determination of degree of pyritisation and the recognition of iron-limited pyrite formation. *Chemical Geology* **111**, 101-110.

40. Williamson MA, Rimstidt JD (1994) The kinetics and electrochemical rate-determining step of aqueous pyrite oxidation. *Geochimica et Cosmochimica Acta* **58**, 5443-5454.

41. Evangelou VP, Zhang YL (1995) A review: Pyrite oxidation mechanisms and acid mine drainage prevention. *Critical Reviews in Environmental Science and Technology* **25**, 141-199.

42. Moses CO, Nordstrom DK, Herman JS, Mills AL (1987) Aqueous pyrite oxidation by dissolved oxygen and ferric iron. *Geochimica et Cosmochimica Acta* **51**, 1561-1571.

43. Moses CO, Herman JS (1991) Pyrite oxidation at circumneutral pH. *Geochimica et Cosmochimica Acta* **55**, 471-482.

44. Widdel F, Schnell S, Heising S, Ehrenreich A, Assmus B, Schink B (1993) Ferrous iron oxidation by anoxygenic phototrophic bacteria. *Nature* **362**, 834-836.

45. Stumm W, Morgan JJ (1981) *Aquatic Chemistry* 2nd ed., Wiley-Interscience, New York, NY.

46. S. Heising, L. Richter, W. Ludwig, B. Schink, *Arch. Microbiol.* **172**, 116-124 (1999).

47. D.E. Canfield, B. Thamdrup, E. Kristensen, *Aquatic Geomicrobiology*, Elsevier Academic Press, San Diego, CA (2006).

48. Heising S, Schink B (1998) Phototrophic oxidation of ferrous iron by a *Rhodomicrobium vannielii* strain. *Microbiology* **144**, 2263-2269.

49. Kappler A, Newman DK (2004) Formation of Fe(III)-minerals by Fe(II)-oxidizing photoautotrophic bacteria. *Geochimica et Cosmochimica Acta* **68**, 1217-1226.

50. Sherlock EJ, Lawrence RW, Poulin R (1995) On the neutralization of acid rock drainage by carbonate and silicate minerals. *Environmental Geology* **25**, 43-54.

51. White AF, Brantley SL (1995) Chemical weathering rates of silicate minerals: An overview. *Reviews of Mineralogy and Geochemistry* **31**, 1-22.

52. Lengke MF, Tempel RN (2005) Geochemical modeling of arsenic sulfide oxidation kinetics in a mining environment. *Geochimica et Cosmochimica Acta* **69**, 341-356.

53. Rye R, Kuo PH, Holland HD (1995) Atmospheric carbon dioxide concentrations before 2.2 billion years ago. *Nature* **378**, 603-605.

54. Haqq-Misra JD, Domagal-Goldman SD, Kasting PJ, Kasting JF (2008) A revised, hazy methane greenhouse for the Archean Earth. *Astrobiology* **8**, 1127-1137.

55. Ohmoto H, Watanabe Y, Kumazawa K (2004) Evidence from massive siderite beds for a CO_2-rich atmosphere before ~1.8 billion years ago. *Nature* **429**, 395-399.

56. Straub KL, Benz M, Schink B, Widdel F (1996) Anaerobic, nitrate-dependent microbial oxidation of ferrous iron. *Applied and Environmental Microbiology* **62**, 1458 1460.

57. Benz A, Brune A, Schink B (1998) Anaerobic and aerobic oxidation of ferrous iron at neutral pH by chemoheterotrophic nitrate-reducing bacteria. *Archives of Microbiology* **169**, 159-165.

58. Meyers CR, Nealson KH (1988) Microbial reduction of manganese oxides: Interactions with iron and sulfur. *Geochimica et Cosmochimica Acta* **52**, 2727-2732.

59. McKibben MA, Barnes HL (1986) Oxidation of pyrite in low temperature acidic solutions: Rate laws and surface textures. *Geochimica et Cosmochimica Acta* **50**, 1509-1520.

60. Langmuir D (1997) *Aqueous Environmental Geochemistry*, Prentice Hall, Inc., Upper Saddle River, NJ.

61. Kasting JF (1987) Theoretical constraints on oxygen and carbon dioxide concentrations in the Precambrian atmosphere. *Precambrian Research* **34**, 205-229.

62. Eigenbrode JL, Freeman KH (2006) Late Archean rise of aerobic microbial ecosystems. *Proceedings of the National Academy of Sciences USA* **103**, 15759-15764.

63. Kamber BS, Whitehouse MJ (2007) Micro-scale sulphur isotope evidence for sulphur cycling in the late Archean shallow ocean. *Geobiology* **5**, 5-17.

64. Farquhar J, Peters M, Johnston DT, Strauss H, Masterson A, Wiechert U, Kaufman AJ (2007) Isotopic evidence for Mesoarchaean anoxia and changing atmospheric sulphur chemistry. *Nature* **449**, 706-709.

65. Ohmoto H, Watanabe Y, Ikemi H, Poulson SR, Taylor BE (2006) Sulphur isotope evidence for an oxic Archaean atmosphere. *Nature* **442**, 908-911.

66. Domagal-Goldman SD, Kasting JF, Johnston DT, Farquhar J (2008) Organic haze, glaciations and multiple sulfur isotopes in the Mid-Archean Era. *Earth and Planetary Science Letters* **269**, 29-40.

67. Kasting JF, Howard MT (2006) Atmospheric composition and climate on the early Earth. *Philosophical Transactions of the Royal Society B* **361**, 1733-1742.

68. Lyons JR (2007) *Geophysical Research Letters* **34**, doi: 10.1029/2007GL031031.

69. Catling DC, Claire MW, Zahnle KJ (2007) Anaerobic methanotrophy and the rise of atmospheric oxygen. *Philosophical Transactions of the Royal Society A* **365**, 1867-1888.

70. Habicht KS, Gade M, Thamdrup B, Berg P, Canfield DE (2002) Calibration of sulfate levels in the Archean ocean. *Science* **298**, 2372-2374.

71. Barley ME, Pickard AL, Sylvester PJ (1997) Emplacement of large igneous province as a possible cause of banded iron formation 2.45 billion years ago. *Nature* **385**, 55-58.

CHAPTER 3

OXIDATIVE WEATHERING ON THE EARLY EARTH

Preface:

The contents of this chapter represent a manuscript in preparation for submission to the journal *Chemical Geology*. This is reflected in the formatting, which includes numbered section headings throughout the article.

Introduction:

Recently accumulating evidence suggests that the biological production of oxygen in Earth's surface oceans preceded the initial accumulation of large amounts of oxygen in the atmosphere by 100 million years or more. However, the potential effects of oxygen production on surface ocean chemistry have remained little explored, and questions persist regarding both the potential role of oxidants other than molecular oxygen and the locus of oxidation of crustal material (i.e., subaerial and/or submarine settings). Here, we revisit the notion of transient and/or spatially restricted 'oxygen oases' in the Archean surface ocean by employing a simple steady-state box model of the surface ocean in a coastal upwelling system, and explore the plausibility that such a system could support the widespread oxidation of reduced crustal minerals. We find that although it is possible to establish strong air-sea gas exchange disequilibrium with respect to O_2, there is an apparent timescale mismatch between the kinetics of oxidative dissolution and the rate at which reduced minerals delivered physically to shallow marine sediments will be buried below the zone of oxidant penetration. Estimated dissolution timescales compare more favorably with typical timescales of soil development, despite the much lower dissolved oxygen concentrations inferred for a subaerial environment at gas exchange equilibrium with atmospheric pO_2. We suggest that, although the production and accumulation of dissolved O_2 in the Archean surface ocean is probable under certain conditions and should be explored as a biogeochemical agent, it is unlikely that extensive oxidative weathering of chalcophile elements such as Mo, Re, and S occurred within the marine realm.

Main Article:

1. INTRODUCTION

The evolution of oxygenic photosynthesis has dramatically reshaped the chemistry of the surface Earth, and the presence of significant quantities of O_2 in the atmosphere and ocean now drives the fundamental dynamics of nearly all quantitatively significant biogeochemical cycles (C, S, P, N, Fe). Whether by direct consumption through the metabolic demands of large, complex organisms, or through the recycling of essential substrates within microbial ecosystems, biologically produced O_2 provides nearly all of the substrates used in metabolic electron transfer on a global scale. Although it is widely accepted that the partial pressure of O_2 in Earth's atmosphere has increased through time (with attendant, although somewhat complex, changes in ocean ventilation), there is still much debate surrounding the timing of the emergence of oxygenic photosynthesis and little is known about the detailed tempo and mode with which this metabolic innovation came to shape early Earth surface chemistry.

Despite arguments that have suggested the evolution of cyanobacterial oxygenic photosynthesis as early as ~3.8 Ga (*1*), perhaps the most compelling arguments emerged through the examination of solvent-extractable lipid biomarker records (*2-4*). Subsequent work has suggested that this early record resulted from later migration (*5*), calling the syngeneity of the biomarkers into question. This provided 'negative' support for the view that the earliest compelling evidence for oxygenic photosynthesis is the initial rise in atmospheric $p\mathrm{O_2}$ during the Paleoproterozoic (e.g., *6*), presently constrained by the rare sulfur isotope record to be between ~2.45 – 2.32 Ga (*7-9*). In contrast, a number of recent studies have presented geochemical evidence suggesting non-trivial oxidative mobility of a number of different elements typically stored in the crust as reduced phases and most soluble as oxyanions (MoO_4^{2-}, ReO_4^{-}, CrO_4^{2-}, SO_4^{2-}, NO_3^{-}), arguing for the presence of oxygenic photosynthesis on a reducing Earth surface significantly prior to the Paleoproterozoic rise in $p\mathrm{O_2}$ (*10-17*). Arguments have also been presented based on C-S-Fe systematics without resort to geochemical evidence for oxidative mobilization (*18*).

Taken together, these results suggest the possibility that oxygenic photosynthesis may have evolved significantly prior to the first significant rise in $p\mathrm{O_2}$ recorded during the Paleoproterozoic, both with and without (e.g., *18*) exerting geochemically significant effects on Earth's surface. However, strictly speaking such patterns only require mobilization and transport under conditions that are oxidizing with respect to the element in question, with no *a priori* necessity for the presence of biologically produced O_2. In addition, the aforementioned studies generally do not claim to distinguish between a subaerial and submarine weathering system – in other words, is the mobilization process occurring in shallow ocean sediments or in the subaerial realm?

The latter distinction may seem somewhat esoteric, but has potentially important implications for our understanding of the detailed pattern of surface Earth oxygenation. If the process is dominated by accumulation of O_2 (or other oxidants) in the surface ocean on a broad scale, this suggests a more nuanced Earth surface redox structure than most models provide (*17*), and raises questions about sea-air gas exchange and the magnitude of disequilibrium that can feasibly be sustained in communication with a strongly reducing atmosphere. On the other hand, a subaerial mechanism would have an entirely different set of implications. For example, most 1-D photochemical models suggest that when pO_2 is below $\sim10^{-5}$ PAL it is not well mixed within the atmosphere (*19*), raising questions regarding the physicochemical and temporal dynamics necessary to sustain subaerial oxidative mobilization. Further, if the oxidant is not in the gas phase it would presumably need to be generated *in-situ*, which may provide information about the evolution of other chemosynthetic metabolisms or inorganic surface chemistry in terrestrial settings.

In what follows, we discuss the potential of oxidants other than O_2 to drive the observed patterns in the late Archean record, and suggest that although it is difficult to rule out alternative oxidants in every case it is by far most parsimonious to hypothesize that the active oxidant is molecular oxygen. We then revisit the notion of spatially and/or temporally restricted accumulation of O_2 in the surface ocean (‘oxygen oases’; *20*), as a first-order basis for evaluating the plausibility of oxidative mobilization in shallow marine sediments. This is followed by a comparison of what we can infer about the timescales of mobilization, transport and removal from the surface system in subaerial and submarine systems.

2. ALTERNATIVE OXIDANTS

When considering the mobilization of Mo, Re, and S as oxyanions, one must consider the oxidative weathering of sulfide mineral phases in sedimentary and crustal rocks. The majority of empirical and laboratory data available are for pyrite (FeS_2), the most abundant metal sulfide in Earth's crust (*21*), and we use pyrite here and in the treatment to follow as a 'proxy' for metal sulfide phases. We emphasize that such an approach will be necessarily revised as more field and laboratory data for other metal sulfide phases become available. From a thermodynamic standpoint, several oxidants other than O_2 could be invoked to promote oxidative dissolution of sulfides, including (in order of reducing oxidation potential) nitrate (NO_3^-), manganese oxide phases (denoted here as MnO_2), and ferric iron (Fe^{3+}), either in dissolved or mineral form. These are each discussed in turn.

2.1. Nitrate (NO_3^-)

Microbially catalyzed oxidation of FeS_2 using NO_3^- has been suggested for aquifer systems and anoxic groundwater sediments (*22-24*) and can be depicted as:

$$5FeS_2 + 14NO_3^- + 4H^+ \rightarrow 7N_2 + 10SO_4^{2-} + 5Fe^{2+} + 2H_2O \ . \qquad (3.1)$$

There are two principal problems with invoking such a mechanism as the driving force for Archean sulfide oxidation. The first is empirical – field studies in modern bioturbated sediments monitoring the dissolution of tracer-marked $^{55}FeS_2$ strongly suggest that although both FeS and FeS_2 can be efficiently oxidized by MnO_2, FeS_2 is not oxidized with NO_3^- or amorphous ferric oxides (*25,26*). We return to MnO_2 and ferric oxides below. The second is *a priori* – the generation of significant quantities of NO_3^- would appear to require, either directly or indirectly, the presence of molecular oxygen in the environment. Luther et al. (*27*) suggested the possibility of anaerobic NH_4^+ oxidation using MnO_2 as an electron acceptor, with one variant of this process yielding NO_3^-:

$$NH_4^+ + 4MnO_2 + 6H^+ \rightarrow 4Mn^{2+} + NO_3^- + 5H_2O \ . \tag{3.2}$$

We note that other possible stoichiometries would yield N_2 rather than NO_3^-. However, observational evidence to support such a mechanism is, at present, controversial. Aller et al. (*28*) invoke it to explain certain features of pore water chemistry from the Panama Basin, and Hulth et al. (*29*) suggest this process is occurring in sediments from Long Island Sound but is masked by rapid NO_3^- consumption through denitrification. However, a ^{15}N-tracer study of anoxic NH_4^+-rich coastal marine sediments containing ~3 wt% MnO_2 and reactive oxidized Mn to depths of greater than 10cm failed to provide any evidence of the process occurring (*30*). In short, although this mechanism is thermodynamically feasible, it awaits concrete demonstration of quantitative environmental significance and has not been shown to operate in modern environments in which it should be most favorable. Further, it would still suffer from the problem that significant MnO_2 production would itself seem to require the presence of O_2 in the environment (discussed below).

2.2 Manganese oxides (MnO_2)

The oxidative dissolution of FeS_2 by manganese oxide phases is well known (*25, 26, 31*). This can be shown as:

$$\mathrm{FeS_2 + 7.5MnO_2 + 11H^+ \rightarrow Fe(OH)_3 + 2SO_4^{2-} + 7.5Mn^{2+} + 4H_2O}\ . \tag{3.3}$$

Alternative stoichiometries may yield elemental sulfur (S^0) rather than sulfate (*25*). The generation of manganese oxides is conventionally assumed to require O_2. A typical mechanism (ignoring Mn^{3+} production and/or disproportionation for simplicity) is:

$$\mathrm{2Mn^{2+} + O_2 + 2H_2O \rightarrow 2MnO_2 + 4H^+}\ . \tag{3.4}$$

In modern environments, this process is microbially catalyzed, and the abiotic oxidation of Mn^{2+} by O_2 is extremely slow (*32*). While it is thermodynamically plausible for NO_3^- to serve as an oxidant for Mn^{2+}, we are aware of no experimental or field evidence for this process. In any case, this mechanism would be no more satisfactory than oxidation using NO_3^- – in other words, both mechanisms are mutually dependent on each other in order to generate the necessary electron acceptor, and the only oxidant plausibly available at Earth's surface in sufficient quantities that can short-circuit this dependence is O_2.

2.3 Ferric iron (Fe^{3+})

In marine sediments, there is sound evidence from field studies suggesting that Fe^{3+} phases will not serve as an oxidant for FeS_2 (*25, 26, 31*). In low-temperature subaerial weathering environments the oxidative dissolution of FeS_2 can be summarized as (*33, 34*):

$$FeS_2 + \frac{7}{2}O_2 + H_2O \rightarrow Fe^{2+} + 2SO_4^{2-} + 2H^+ \ , \tag{3.5}$$

$$Fe^{2+} + \frac{1}{4}O_2 + H^+ \rightarrow Fe^{3+} + \frac{1}{2}H_2O \ , \tag{3.6}$$

$$FeS_2 + 14Fe^{3+} + 8H_2O \rightarrow 15Fe^{2+} + 2SO_4^{2-} + 16H^+ \ . \tag{3.7}$$

The primary role of O_2 in environments supporting sulfide oxidation is conventionally thought to be the regeneration of Fe^{3+} from Fe^{2+}, with Fe^{3+} serving as the 'primary' oxidant. Iron provides an interesting contrast to other potential oxidants, because any process that can regenerate Fe^{3+} with sufficient speed and efficiency should in principle be able to sustain sulfide mineral oxidation in subaerial systems.

The sustained regeneration of Fe^{3+} could proceed in an anoxic system at the expense of NO_3^- (*35, 36*), MnO_2 (*37*), through UV photooxidation (*38, 39*), and through anoxygenic photosynthesis with Fe^{2+} as an electron donor (*40*). The first two possibilities require the production and accumulation of NO_3^- and MnO_2, which is discussed above and will not be considered further here. Photooxidation of Fe^{2+}, during which dissolved Fe^{2+} species absorb short-wave solar radiation (200-400 nm) and are oxidized to dissolved Fe^{3+} species that are subsequently hydrolyzed and precipitated as amorphous Fe oxides, has been shown to occur under acidic conditions and at circum-neutral pH (*39*). This mechanism has been discussed by many authors as a possible anoxic pathway to the formation of banded iron formations (BIFs) during the Archean (*39, 41-43*).

Anoxygenic photosynthesis could also promote the regeneration of Fe^{3+}, and has been presented as alternative catalyst for the deposition of BIFs (*44, 45*)

Although it now seems unlikely that a photooxidation mechanism would be quantitatively important against other Fe^{2+} loss processes in marine settings (e.g., *46*), we should consider whether this process could drive the oxidative dissolution of sulfide minerals in subaerial environments. This is difficult to evaluate with any certainty, but this mechanism should be operative at any period of Earth's history during which ozone column depth was insufficient to prevent short-wave radiation from reaching ground level. Even at the highest estimated pO_2 values for the Archean atmosphere, O_3 production should be minimal (*19*, *47, 48*), indicating that, if operative and quantitatively significant, regeneration of Fe^{3+} through photooxidation in subaerial settings should have been ubiquitous. However, sulfidic black shales of the ~2.7 Ga Jeerinah Formation show no authigenic enrichment of Mo (*18*), which suggests that there is some temporal texture to the mobilization of redox-sensitive trace elements through the mid- and late-Archean and would seem to provide evidence against a presumably ubiquitous photochemical mechanism.

The photosynthetic oxidation of Fe^{2+} provides another possible mechanism, but we emphasize again that this provides little leverage in the marine realm given the combined observations that hydrolysis lifetimes of dissolved Fe^{3+} species are orders of magnitude shorter than dissolution timescales of sulfide mineral phases (*33, 49*) and amorphous Fe oxides will not dissolve FeS_2 (discussed above). In subaerial environments, the plausibility of this mechanism is less clear. However, the standard electrode potentials of the $Fe(OH)_3/Fe^{2+}$ and Fe^{3+}/Fe^{2+} couples approach or exceed the midpoint potentials of well studied anoxygenic photosynthetic reaction centers below pH values of ~5 (*50-52*). This is consistent with the observation that photosynthetic iron oxidizers at present appear to show a very narrow pH range for optimum growth that is slightly below neutral (*51, 53, 54*).

In summary, we suggest that although there are many other potential oxidants that may be appealed to in order to explain the observation of increased mobilization and transport of oxyanions during the late Archean, most of these either indirectly require the presence of O_2 in the environment or are less plausible on other grounds. We conclude that the most parsimonious explanation at present is that biological O_2 production indeed evolved significantly prior to the Paleoproterozoic rise in atmospheric oxygen.

3. Accumulation of O_2 in the surface ocean

3.1 A simple model

Given the possibility of oxygenic photosynthesis in the Archean surface ocean, it would be reasonable to suggest that evidence for oxidative mobilization of a suite of different elements preserved in the late Archean record perhaps reflects oxidation in shallow marine sediments (*10, 11, 15*). To explore this possibility further, it would be useful to have some sense as to the O_2 concentrations that a reduced mineral phase might encounter after physical weathering and transport to the ocean. Kasting (*20*) first suggested the possibility of localized accumulation of dissolved O_2 in the Archean surface ocean, a concept often referred to as ‘oxygen oases’. If such environments existed during the Archean, it would be plausible to support aerobic respiration and a variety of inorganic redox processes while maintaining a broadly reducing atmosphere. This concept has been the subject of debate (e.g., *55, 56*), and questions have been raised regarding how stable such a system would be against physical mixing, gas exchange, and reductant input from the deep ocean.

We revisit the 'oxygen oasis' concept by utilizing a simple box model of the surface ocean, meant to represent a coastal upwelling system (*57, 58*; Fig. 3.1). Although we acknowledge that very little is known about meridional or zonal ocean circulation on a global scale during the Archean, we consider it likely that the type of environment depicted by our model represents the most plausible set of conditions for supporting elevated rates of carbon fixation (and, thus, export production), and is therefore a natural starting point for examining the degree to which O_2 might be expected to accumulate within localized regions of the surface ocean.

The model is divided into three boxes, with the surface ocean represented by a proximal "active" box (*S2*) and a distal "inactive" box (*S1*), combined with a third "inactive" box representing intermediate depths beneath the zone of upwelling (*I*). The active surface box responds to forcing according to the boundary conditions supplied by the inactive boxes and air-sea gas exchange. Physical mixing is described by computing a vertical upwelling velocity based on average surface wind speed. We neglect vertical (diapycnal) and horizontal (isopycnal) mixing due to turbulent diffusivity, as these terms are typically small relative to the advective velocities associated with coastal upwelling (e.g., *59*). In addition, the boundary conditions of the model (discussed below) are such that the incorporation of physical mixing terms associated with eddy processes will only serve to dampen accumulation of biological O_2 in the surface ocean. The upwelling flux is sourced from intermediate water column depths, consistent with modern eastern boundary current systems.

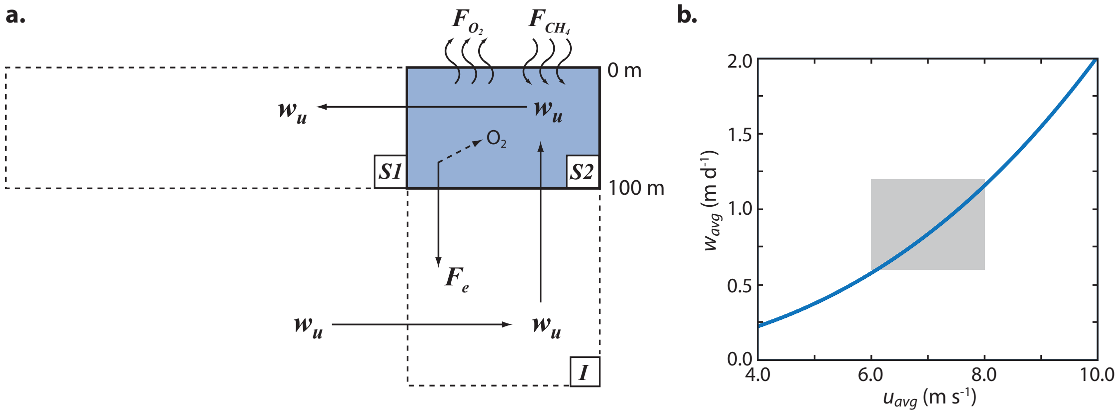

Figure 3.1. Schematic depiction of the surface ocean model used in the text (**a**), and the model parameterization of total vertical transport (w_{avg})as a function of annually averaged surface wind speed (u_{avg}) (**b**). Parameter definitions and values are shown in Table 1. The blue shaded box in (**a**) is the active box in the model, with the other two providing the necessary boundary conditions. In (**b**), the blue curve shows the relationship between u_{avg} and w_{avg} expressed in the model, while the grey shaded box shows the range of values for modern eastern boundary current systems (*60, 61*, and references therein).

The upwelling velocity can be described physically as the quotient of offshore Ekman transport (U_E) and a characteristic length scale over which this transport decays (L_u). Offshore Ekman transport is in turn a function of wind stress (τ), seawater density (ρ_{sw}) and the Coriolis parameter (f):

$$U_E = \frac{\tau}{\rho_{sw} f} \quad . \tag{3.8}$$

The wind stress is related to the surface wind speed (*u*), air density (ρ_{air}) and a drag coefficient (C_D) as:

$$\tau = \rho_{air} C_{\mathrm{D}} u^2 \ . \tag{3.9}$$

We calculate the drag coefficient based on surface wind speed according to the empirical function of Smith (*62*) (see also *63*):

$$C_{\mathrm{D}} = [0.61 * 0.063u] * 10^{-3} \ . \tag{3.10}$$

The characteristic length scale (L_u) can be thought of as the width of active Ekman divergence – vertical velocity distal to this zone is driven by the cyclonic curl of the wind stress, and is typically of a much smaller magnitude (*64*). This length scale is conventionally taken to be the latitude-dependent local Rossby radius of deformation (*65*), but it also depends to some extent on the local Ekman layer depth and shelf geometry [see, for example, *66*]. The relationship between surface wind speed and vertical velocity thus depends, in principle, on the latitudinal distribution of the upwelling zone (which influences both *f* and the local Rossby radius) and shelf geometry.

For simplicity, we assume a constant value for *f* (4.99×10^{-5} s^{-1}, equivalent to an assumed latitude of 20ºN/S), and an off-shore length scale L_u of 125 km. The latter is meant to represent the broad zone of enhanced vertical transport within an eastern boundary current system (*60*), where rates of primary production and carbon export flux are highest. The relationship between annually averaged surface wind speeds and total vertical transport within the zone of active upwelling for our simple parameterization is shown in Figure 3.1b. We feel that imposing constant values for *f* and L_u is a reasonable simplification given the first-order nature of the questions explored here and considering that any latitude or shelf geometry that we might assume for the Archean coastal ocean is somewhat arbitrary. A more detailed study incorporating three-dimensional transport and realistic bathymetry would be worthwhile, but is beyond our scope here.

The final physical term important for regulating the steady-state O_2 concentration of the surface ocean in the model is the air-sea gas exchange flux (F_{O_2}) given by:

$$F_{\mathrm{O}_2} = k_{\mathrm{O}_2} * \Delta[\mathrm{O}_2] \ , \tag{3.11}$$

where k_{O_2} denotes a gas exchange velocity and $\Delta[O_2]$ represents the 'saturation anomaly', or the departure of a water mass from saturation equilibrium with ambient atmospheric pO_2 ($[O_2]_{sat} - [O_2]_{S2}$). Values for $[O_2]_{sat}$ are calculated for a temperature of 20ºC and a salinity of 35‰ using the equations of (*67*) and assuming an atmospheric pO_2 of 10^{-5} PAL. Our results are very weakly sensitive to the latter assumption provided atmospheric pO_2 is presumed to be at or below this value. We parameterize the dependence of gas exchange velocity on wind speed following the conventional formulation of (*68*):

$$k_{\mathrm{O}_2} = 0.31u^2[Sc/660]^{-0.5} \ , \tag{3.12}$$

where u is the surface wind speed and Sc is the Schmidt number for oxygen, a dimensionless parameter describing the relationship between the kinematic viscosity of seawater (μ) and the molecular diffusivity (D_x) of a given gas ($Sc = \mu/D_x$) . Input parameters and sources are listed in Table 3.1.

When considering the potential for accumulation of O_2 in the surface ocean, it is most meaningful to examine export fluxes of carbon from the photic zone (F_e) rather than overall rates of carbon fixation. The export flux must, by definition, be balanced by a net accumulation of O_2 in the region of production, subject to the constraints imposed by physical mixing, gas exchange, and biogeochemical sink terms. We have elected to use export fluxes of carbon as an "independent variable", decoupled from the transport terms. Strictly speaking this is not physically realistic, as export flux can be expected to respond to rates of primary production, which will in turn respond to the recharge of nutrients to the photic zone and therefore changes in upwelling flux. The primary reason for decoupling export fluxes from the physical circulation is that in order to explicitly couple them we would need to implement another suite of assumptions regarding deep ocean nutrient status and the strength/efficiency of the biological pump, a non-trivial task given our poor understanding of Archean ocean chemistry and surface ocean ecology. As an alternative, we vary surface wind speed to yield a range of annually integrated upwelling velocities typical of modern coastal systems (Fig. 3.1b) and explore a range of export fluxes characteristic of environments that show a similar annually integrated upwelling rates.

The concentration of dissolved oxygen in the surface box of the model evolves as:

$$\frac{d}{dt}[\mathrm{O}_2]_{S2} = \Delta_{mix} + F_{\mathrm{O}_2} + J_{bio} \ , \tag{3.13}$$

where the terms on the right-hand side represent, respectively, sources minus sinks due to physical mixing (Δ_{mix}), the gas exchange flux (F_{O_2}) and sources minus sinks due to biogeochemical processing (J_{bio}):

$$\Delta_{mix} = w_u[\mathrm{O_2}]_I - w_u[\mathrm{O_2}]_{S2} \ , \tag{3.14}$$

$$F_{\mathrm{O_2}} = k_{\mathrm{O_2}}([\mathrm{O_2}]_{sat} - [\mathrm{O_2}]_{S2}) \ , \tag{3.15}$$

$$J_{bio} = r_{O:C}F_e - w_u r_{\mathrm{O:Fe}}[\mathrm{Fe}^{2+}]_I - w_u r_{\mathrm{O:CH_4}}[\mathrm{CH_4}]_I - k_{\mathrm{CH_4}}[\mathrm{CH_4}]_{sat} \ . \tag{3.16}$$

In Eq. 3.16, F_e is the export flux of carbon from the photic zone, $r_{\mathrm{O:C}}$ is the stoichiometric ratio between carbon export and O_2 production, and $[\mathrm{Fe}^{2+}]_I$ and $[\mathrm{CH_4}]_I$ represent the concentrations of dissolved iron and methane in intermediate waters. The terms $r_{\mathrm{O:Fe}}$ and $r_{\mathrm{O:CH_4}}$ represent the stoichiometry of O_2 consumption through Fe^{2+} and CH_4 oxidation, respectively. The last term in Eq. 3.16 follows from our assumption that CH_4 introduced to the surface ocean through air-sea gas exchange is quantitatively oxidized.

At steady state, inputs and outputs of O_2 to the active surface box due to physical mixing and biogeochemical processes are balanced. If we further assume that both the deep ocean and areas distal to nutrient recharge are reducing (i.e., $[O_2]_I \sim [O_2]_{S1} \sim 0$), and combine the Fe^{2+} and CH_4 consumption terms into a single reductant flux (J_{red}), we can obtain a solution for the O_2 concentration in the active surface box:

$$[\mathrm{O_2}]_{S2} = \frac{1}{w_u k_{\mathrm{O_2}}}(k_{\mathrm{O_2}}[\mathrm{O_2}]_{sat} + r_{\mathrm{O:C}}F_e - J_{red} - k_{\mathrm{CH_4}}[\mathrm{CH_4}]_{sat}) \ . \tag{3.17}$$

We examine a range of values for parameters that are rather poorly constrained, in particular the reducing capacity of deeper waters being upwelled to the surface box. Calculations assuming calcite-siderite co-equilibrium provide estimates of deep water $[Fe^{2+}]$ on the order of ~40-120 μmol kg^{-1} (*80, 81*), and we explore here an order of magnitude range in $[Fe^{2+}]_I$, from 10 – 200 μmol kg^{-1} (Table 3.1). We note, however, that some estimates of deep water [Fe^{2+}] during the Archean are substantially higher than this (e.g., *82*), so this flux term in our model should probably be viewed as a lower estimate.

Table 3.1. Parameters used in the surface ocean model.

Parameter	Description	Value/Range	Units	Source
μ	kinematic viscosity of seawater	9.23×10^{-7}	$m^2 s^{-1}$	*69*
D_{O2}	molecular diffusivity of O_2	2.13×10^{-9}	$m^2 s^{-1}$	*70*
Sc_{O2}	Schmidt number for O_2	433	-	(see text)
D_{CH4}	molecular diffusivity of CH_4	1.56×10^{-9}	$m^2 s^{-1}$	*70*
Sc_{CH4}	Schmidt number for CH_4	592	-	(see text)
ρ_{sw}	seawater density	1027	$kg\ m^{-3}$	*71*
ρ_{air}	air density	1.2	$kg\ m^{-3}$	*72*
f	Coriolis parameter	4.98×10^{-5}	-	(see text)
L_u	length scale of upwelling zone	125	km	*60, 61*
$r_{O:C}$	stoichiometry of O_2 production	1.45	-	*73, 74*
$r_{O:Fe}$	stoichiometry of Fe^{2+} oxidation	0.25	-	*75*
$r_{O:CH_4}$	stoichiometry of CH_4 oxidation	2.00	-	*76*
pO_2	atmospheric partial pressure of O_2	2.09	ppmv	*77*
pCH_4	atmospheric partial pressure of CH_4	1000	ppmv	*78, 79*
F_e	carbon export flux	0 – 500	$gC\ m^{-2}\ y^{-1}$	-
u	surface wind speed (ann. avg.)	4 – 10	$m\ s^{-1}$	-
[Fe^{2+}]	Fe^{2+} concentration in *I* box	10 – 200	$\mu mol\ kg^{-1}$	*80, 81*

Concentrations of CH_4 are almost totally unconstrained, but in a reducing ocean with any labile carbon flux it is very likely that some reservoir of dissolved CH_4 would exist in the deep ocean. We impose a constant and relatively low dissolved $[CH_4]$ value of 10 μmol kg^{-1}. This can be viewed mechanistically as representative of reducing systems in which dissolved $[CH_4]$ is buffered by SO_4^{2-} at levels that are conventionally taken to be thermodynamically controlled (*83, 84*). This is likely conservative for our purposes, given that oceanic SO_4^{2-} levels were quite low during the Archean (*85, 86*) and that modern systems characterized by reducing, sulfate-deficient deep waters typically accumulate extremely high levels of dissolved CH_4 (e.g., *87*). Furthermore, we do not include other possible sources of reducing power, such as dissolved Mn^{2+} or NH_4^+. In essence, we seek to place upper limits on the ability of our model system to accumulate O_2, for the purposes of establishing plausible boundaries for our subsequent examination of sulfide mineral oxidation in Archean shallow marine sediments.

3.2 Model results

Results of the simple model are shown in Figure 3.2. Our results are consistent with Kasting (*20*) at low reductant levels and relatively low vertical transport rates (Fig. 3.2a), in that dissolved $[O_2]$ values in excess of ~10 μmol kg^{-1} can be attained when rates of advection and reducing capacity of deep waters are relatively low. At higher reductant concentrations there is a significant region of parameter space that is undersaturated with respect to $pO_2 = 10^{-5}$ PAL (Fig. 3.2b). However, it is also clear that reasonable changes within the approximate modern ranges of vertical transport and carbon export flux, such as may occur on seasonal timescales, are sufficient to traverse from [O_2] values below saturation to values greatly in excess of saturation equilibrium. It is important to stress the magnitude of this disequilibrium – a dissolved [O_2] concentration of 1 μmol kg^{-1} is equivalent to a roughly 300-fold oversaturation with respect to an atmospheric pO_2 of ~10^{-5} PAL. Thus, as argued by Kasting (*20*), it is reasonable to imagine severe ocean-atmosphere disequilibrium with respect to O_2 on a reducing Earth surface within biologically productive regions of the ocean.

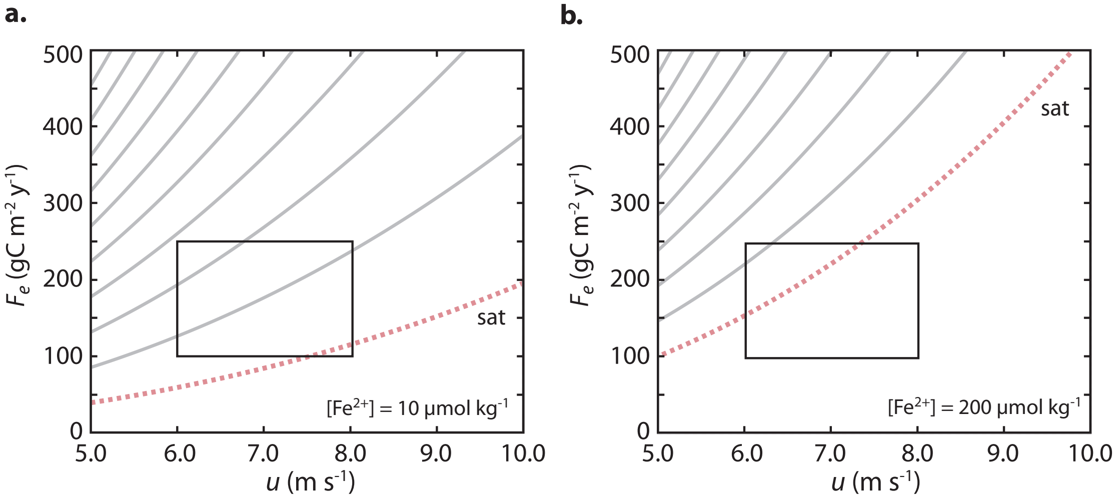

Figure 3.2. Concentrations of dissolved O_2 in the coastal surface ocean as a function of export flux of carbon from the simple box model. Calculations are shown for intermediate-water [Fe^{2+}] values of 10 μmol kg^{-1} (**a**) and 100 μmol kg^{-1} (**b**). Contours are steady-state [O_2] values (in μmol kg^{-1}), with a contour interval of 5 μmol kg^{-1}. The dashed red contours represent the saturation line at atmospheric $pO_2 = 10^{-5}$ PAL. Black boxes denote an approximate range of typical average wind speeds (u) and carbon export fluxes (F_e) for modern eastern boundary current systems.

That said, we consider dissolved [O_2] values significantly above ~10 μmol kg^{-1} unlikely, unless Archean coastal regions were significantly more productive than equivalent modern systems for a given rate of vertical transport. Our calculations may underestimate the reducing power of deep waters, particularly if large concentrations of

CH_4 develop in an oxidant-lean ocean. In addition, our exclusion of vertical and horizontal eddy diffusivity artificially enhances gradients in both dissolved O_2 and deep ocean reductants. Although this effect is likely to be small, it is probably non-trivial. It is also possible that carbon export flux for a given rate of primary production was significantly below modern analog systems prior to the introduction of large, recalcitrant cells, widespread mineral ballasting, and metazoan fecal pellet production. It may be that stable, elevated values of dissolved [O_2] may somewhat paradoxically be more easily achieved in offshore regions, despite attenuated biological productivity, due to less vigorous physical transport and reductant flux. In any case, we suggest that reduced detrital minerals physically transported to the coastal marine realm are unlikely to have been exposed to dissolved [O_2] values greater than ~10 μmol kg^{-1}, and likely much less than this once deposited on the shallow seafloor (i.e., our calculations specify average values and do not allow for a gradient within the local water column).

4. Oxidative processing on the late Archean Earth

In what follows, we explore the possibility that oxidative mobilization of chalcophile elements in late Archean environments occurred in shallow marine sediments, and compare this with the plausibility of subaerial oxidation. The basic approach is a timescale comparison – after obtaining a first-order estimate of the timescale needed to oxidatively dissolve a sulfide mineral, we compare this timescale with the timescale available for oxidation in a given environment. In a marine setting, this will depend on the timescale at which a sulfide mineral that has been physically weathered and transported under purely anoxic conditions and delivered to shallow marine sediments becomes buried beneath the zone of the sediment column into which oxidants penetrate. In a subaerial setting, the applicable comparison is between the dissolution timescale and a characteristic 'weathering timescale', a range which is approximated here by typical soil formation timescales on the modern Earth.

4.1. Oxidative dissolution

Because of the vast literature that exists on the oxidative dissolution kinetics of pyrite (FeS_2; *33, 88-91*), and because this mineral is the most abundant crustal sulfide, we use it as a proxy for crustal sulfide minerals. We acknowledge, however, that different sulfide minerals can be expected to show very different kinetic behavior, and that a similar approach should be applied to other sulfide mineralogies as more robust rate laws become available. We employ the following rate law for dissolution as a function of ambient oxygen (*33*):

$$r = 10^{-8.19(\pm 0.10)} \frac{m_{\mathrm{DO}}^{0.5(\pm 0.04)}}{m_{\mathrm{H^+}}^{0.11(\pm 0.01)}} , \tag{3.18}$$

where r is the pyrite destruction rate (mol m^{-2} s^{-1}). Dissolved oxygen concentrations (DO) in solution at the site of weathering are estimated either by assuming equilibration of a weathering fluid with various pO_2 values using a Henry's Law constant (K_H) at 25ºC of 1.26 x 10^{-3} mol L^{-1} bar^{-1} (*92*), or by using assumed bottom water oxygen concentrations as input values. In the case of a meteoric fluid, we assume sufficient dilution that the Henry's Law constant need not be corrected for ionic strength. We also assume that total atmospheric pressure has remained constant. Calculations for the submarine case are performed at a pH range of 7-9 and a temperature of 10ºC, while calculations for the subaerial case are performed at pH = 5 and a temperature of 25ºC. Although examination of Eq. (3.18) implies a pH effect on dissolution rates, this effect is slight compared to that of dissolved O_2. The effect of temperature, mediated through gas exchange equilibrium, is negligible at the scale considered here. The calculations assume a cubic pyrite grain (the results are not noticeably different if a spherical geometry is assumed) with a given surface area, ranging between 6 x 10^2 µm (side length *l* = 10 µm) and 6 x 10^4 µm (side length *l* = 100 µm), meant to represent fine-grained igneous sulfides (*93, 94*). The lower end of this range is characteristic of framboidal pyrite forming syngenetically in modern sulfidic settings (e.g., *95*).

4.2 Oxygen penetration depth

A first-order approximation for sediment oxygen penetration depth (L_{O_2}) can be given by (*96*):

$$L_{O_2} \approx \sqrt{\phi D_s \frac{w[O_2]_{bw}}{\Sigma k_i F^0_{G_i}}} \tag{3.19}$$

where ϕ is sediment porosity, D_s is the sediment diffusion coefficient for O_2 (corrected for temperature and tortuosity), w is the sedimentation rate, $[O_2]_{bw}$ is the bottom water O_2 concentration, and k_i and $F^0_{G_i}$ represent the first-order decay constant and flux to the sediment-water interface, respectively, of two labile organic matter fractions. We employ a simple ‘multi-*G*’ model (e.g., *97*) with two active organic matter pools and a third that is considered unreactive (and which will subsequently be ignored). While this is clearly an idealized description of organic matter decomposition in marine sediments (*98, 99*), such an approach has been used successfully to describe early diagenesis in a wide range of modern environments (*97*, *100-111*). The total flux of metabolizable carbon to the sediment is partitioned into two fractions of different intrinsic lability (f_{G_1} and f_{G_2}), such that 60% of the overall flux is considered "labile" and 20% of the overall flux is considered "semilabile", with the remaining 20% considered "unreactive" and metabolically unavailable. Rate constants (k_1 and k_2) are chosen to vary over two orders of magnitude, consistent with observations in modern coastal sediments (*85, 112*).

There is a well-established empirical relationship between overall sediment accumulation rates and fluxes of carbon to the benthic system (*113, 114*), and it is essential to take this into account in order to avoid underestimation of O_2 penetration depths at low sedimentation rates. Several empirical relationships between sedimentation rate and carbon flux to the sediment-water interface have been proposed for use in global diagenetic models, and these are summarized in Fig. 3.3a. We choose to employ the algorithm of Middelburg et al. (*113, 114*), as this relationship gives the lowest fluxes of metabolizable carbon for a given sedimentation rate. We have taken care in all parameter choices to avoid underestimating first-order O_2 penetration depths. For example, even the largest carbon flux used in the present exercise (~1.2 mmolC cm^2 y^{-1}) is still rather modest for biologically active continental margin sediments (*113, 115*), and the intrinsic rate constants utilized are on the low end of empirically determined values for metabolizable organic matter in sediments, particularly for the most labile fraction (*52*, *104*, *116, 117*). We examine an order of magnitude range of sedimentation rates (0.1 – 1.0 cm yr^{-1}), meant to represent comprehensively represent sediments deposited along inner-outer shelf environments (*113, 118*), as we expect that physically transported detrital mineral grains would be deposited close to shore.

Parameters are listed in Table 3.2, and L_{O_2} values as a function of $[O_2]_{bw}$ are shown in Fig. 3.3b. Calculated values for sediment oxygen penetration depth are well in accord with data from modern biologically active coastal sediments (*119-130*), and in fact probably over-estimate penetration depths somewhat. We can see that O_2 penetration depths are larger for higher sedimentation rates. The physical reason for this is that in a system in which benthic respiration is not limited by fluxes of metabolizable carbon, a relatively larger fraction of the more labile carbon pool is metabolized closer to the sediment-water interface at lower sedimentation rates.

Table 3.2. Parameters used for estimating sediment O_2 penetration.

Parameter	Description	Value/Range	Units
w	sedimentation rate	0.1 – 1.0	cm y^{-1}
D_0	free diffusion coefficient	1.46×10^{-9}	m^2 s^{-1}
ϕ	porosity	0.8	-
θ^2	squared tortuosity	$1 - \ln\phi^2$	-
D_s	sediment diffusion coefficient	D_0 / θ^2	m^2 s^{-1}
f_{G_1} , f_{G_2}	organic carbon fractions	0.6 , 0.2	-
k_1 , k_2	remineralization rate constants	0.1 , 0.001	y^{-1}

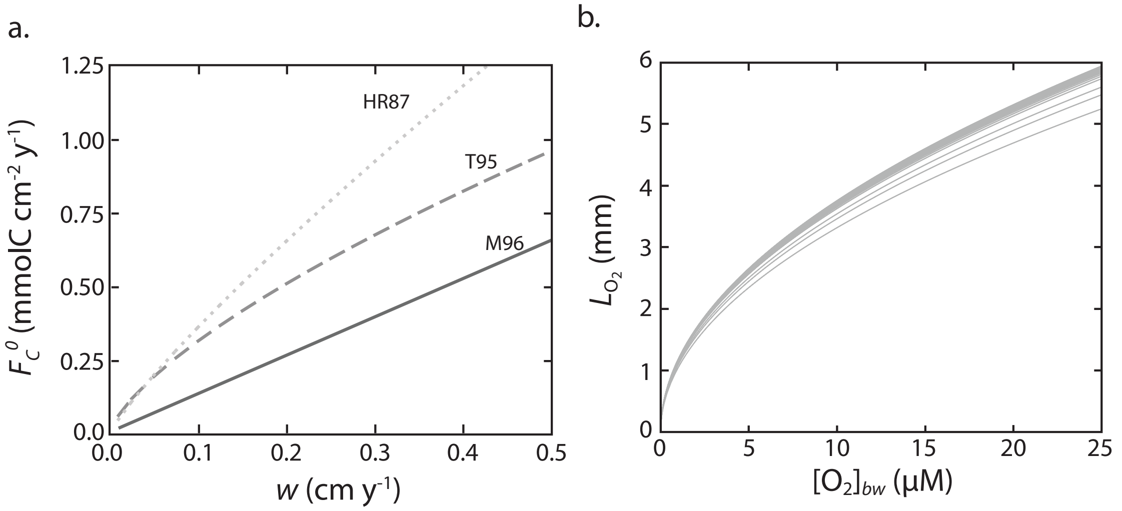

Figure 3.3. The left panel **(a)** depicts functions used to describe the relationship between sediment accumulation rate (*w*) and carbon flux to the sediment-water interface (F_C^0). Shown are the algorithms proposed by Henrichs & Reeburgh (*131*; HR87), Tromp et al. (*118*; T95), and Middelburg et al. (*113*; M96). The right panel **(b)** shows sediment O_2 penetration depths as a function of bottom water oxygen concentration according to the model discussed in the text, using the algorithm from Middelburg et al. (*113*). Each contour represents a different sediment accumulation rate (and thus carbon flux). The contour interval is 0.025 cm y^{-1}.

4.3 Timescale comparison

As can be seen from Fig. 3.4a, the sulfide dissolution timescales are generally orders of magnitude less rapid than the timescales at which a detrital reduced mineral can be expected to be buried below the zone of oxygen penetration. Even under conditions of very small sulfide crystal size (10 μm), low sediment accumulation rates (0.1 cm y^{-1}), and relatively high bottom water O_2, rates of dissolution are nearly an order of magnitude longer than the rates at which detrital sulfides will be buried below the zone of O_2 penetration. This is in spite of assuming relatively low first-order decay constants for organic matter of 0.1 and 0.001 y^{-1} and imposing a conservative algorithm for carbon flux to the sediment-water interface. In addition, we implicitly assume that there is essentially no dissolved O_2 gradient within the surface ocean in our model(s), i.e. that the average steady state O_2 concentration calculated above can be extrapolated to the shallow seafloor. While dissolved NO_3^- or solid Mn-oxides will, in principal, penetrate more deeply into sediments than O_2, it is not likely that this can alleviate an order of magnitude difference in the relative timescales. This problem will be particularly acute in a world in which sediments are not bioturbated by benthic organisms, a process that dramatically enhances the role of Mn-oxides in redox cycling during early diagenesis (e.g., *132*). Higher sedimentation rates and larger crystal sizes, even within a modest range, exacerbate the mismatch in timescales (Fig. 3.4a). We conclude, therefore, that the localization of oxidative weathering of sulfide mineral phases within shallow marine sediments beneath an oxygenated water column is extremely unlikely.

However, dissolution timescales compare much more favorably with typical timescales of soil formation on the modern Earth (Fig. 3.4b). This is so despite: (1) the assumption that sulfide oxidation proceeds exclusively through chemical oxidation by O_2, which is an extremely slow process relative to oxidation via Fe^{3+}; (2) the assumption of essentially abiotic dissolution, which does not consider the effects of crystal defects or microbial activity, both of which can be expected to accelerate dissolution (in some cases dramatically); and, (3) the assumption that local O_2 levels are set by gas exchange equilibrium with a reducing atmosphere. In the first case, local activity of microorganisms that derive chemical energy from the microaerophilic oxidation of Fe^{2+} will dramatically accelerate dissolution rates, and indeed represent perhaps the most crucial component of modern environments that support extensive sulfide mineral oxidation (e.g., *139*). Although the lower O_2 limit for growth of such organisms is not known with precision, it is likely to be very low (*140*). It is crucial to point out that this potential mechanism of enhanced sulfide dissolution rates *cannot apply to submarine settings*, a simple consequence of the hydrolysis and precipitation half-lives of Fe^{3+} species at circumneutral pH. In the second case, rates of microbially enhanced sulfide dissolution are significantly more rapid than typical soil formation timescales (Fig. 3.4b), even at the lowest O_2 levels measured in the laboratory (on the order of a dilute fluid in equilibrium with $pO_2 \sim 10^{-5}$ PAL; *138*). In the third case, *in situ* biological O_2 production, or production proximal to the site of weathering, could increase ambient O_2 levels above that depicted in Figure 3.4b. We return to this below.

5. DISCUSSION

Our results indicate that significant gas exchange disequilibrium could have existed in productive regions of the Archean surface ocean after the evolution of oxygenic photosynthesis, consistent with previous theoretical (*20, 56*) and empirical (*11, 17*) work. However, with reasonable assumptions regarding deep ocean reducing capacity it is still possible to drive the surface ocean below saturation with an atmospheric pO_2 level on the order of 10^{-5} PAL, consistent with existing evidence for a surface ocean that was, at times, reducing with respect to Mn and Ce (*141*). A shift between the two states can be easily driven by relatively small changes in rates of vertical transport and carbon export production, such as may be envisioned to occur on seasonal timescales. We suggest an approximate upper limit on dissolved O_2 in productive coastal regions of the

Archean surface ocean on the order of ~10 μmol kg^{-1}, provided that such systems during the Archean were not characterized by greater productivity and/or carbon export efficiency than modern analog systems at a given rate of vertical transport. Potentially large regions of the surface ocean could be characterized by such elevated O_2 concentrations, on a variety of timescales, while remaining fully consistent with 1-D photochemical models of Archean atmospheric chemistry (*77, 142, 143*).

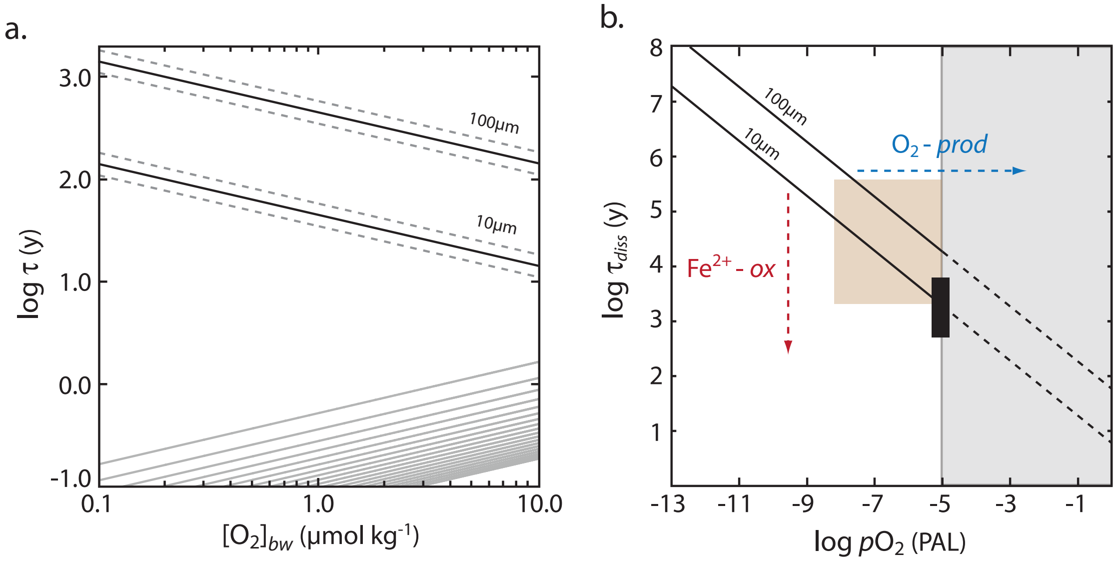

Figure 3.4. Comparison of sulfide mobilization timescales for submarine (**a**) and subaerial (**b**) environments. In (**a**), dissolution timescales of small detrital pyrite crystals are compared to burial timescales beneath the zone of oxidant penetration. The upper curves (black, dashed) show dissolution timescales for cubic pyrite grains between 10 μm and 100 μm in width, with the dashed lines denoting calculations for a pH range between 7 and 9. The lower grey curves show burial timescales beneath the zone of oxidant penetration, derived from a simple diagenetic model, for a range of sedimentation rates. Each contour represents a different sediment accumulation rate (and thus carbon flux), increasing downward with a contour interval of 0.05 cm y^{-1}. In (**b**), dissolution timescales are calculated assuming gas exchange equilibrium with various atmospheric pO_2 values. The tan shaded box represents a range of modern soil formation timescales (*133-137*), while the black square denotes rates of biotic pyrite dissolution at low O_2 concentrations (*138*). Dashed arrows depict schematically processes that would act to enhance sulfide dissolution kinetics (microaerophilic Fe^{2+} oxidation, Fe^{2+} – ox) or elevate local O_2 levels (*in situ* O_2 production).

However, we conclude that such an oxygenated surface layer of the ocean would have been inadequate to force large-scale oxidative mobilization of crustal sulfide minerals. This results from two fundamental constraints: (1) at any reasonable marine pH, the hydrolysis and precipitation timescales for Fe^{3+} will be fast enough to render it an essentially inaccessible source of oxidizing power in marine sediments; and, (2) the burial rates of detrital sulfide phases below the dissolution zone in shallow marine sediments are much more rapid than the timescales needed to chemically dissolved sulfides with O_2. Subaerial settings provide a more attractive locus for oxidative sulfide weathering, as the timescales available are much longer than those that can be expected in the marine realm. In addition, subaerial systems will most often be poorly (rock) buffered, in contrast to the virtually limitless buffering capacity of the ocean, which allows a direct role for Fe^{3+} in supporting sulfide oxidation at low pH.

6. CONCLUSIONS

Recently accumulating evidence suggests that the oxidation of Earth's surface was perhaps a gradual and nuanced process, with redox cycling and chemistry that were spatially and temporally complex and highly textured. We have attempted to add a small piece to this puzzle by exploring the plausibility of a late Archean Earth on which oxidative weathering of reduced crustal minerals was localized within the marine realm. We suggest that surface ocean O_2 concentrations were likely to be highly variable in time and space, but that they were unlikely to exceed ~10 μmol kg^{-1}. It remains to be seen if conditions in offshore settings, such as the center of mid-ocean gyres, were more favorable to the accumulation of higher O_2 concentration. Although such settings will no doubt be characterized by lower rates of biological productivity (and carbon export), differences in physical mixing, which essentially acts to reduce concentration gradients and provides a potentially large flux of reductants to the surface ocean, may be able to compensate for lower O_2 production rates. It is obvious that simple models such as those developed and explored here will be inadequate to exploring these more detailed dynamics of Archean biological O_2 cycling in time and space, and in particular better models must be developed for representing circulation in three dimensions and for coupling the physical transport to rates of biological activity in the surface ocean.

We further conclude that coastal oceanic regions, even those supporting high O_2 fluxes, would not be likely to mobilize significant quantities of physically delivered crustal sulfides. This implies a subaerial mechanism, which in turn implies the accumulation of O_2 to small but finite levels within the atmosphere itself. Given that O_2 in the Archean atmosphere likely behaved as the trace redox gas (*19*, *79*; *142*), it may have varied significantly on a regional and/or temporal basis (e.g., *145*), and it is at present unclear exactly what constraints this poses for subaerial weathering processes. In addition, such subaerial processing of crustal sulfides implies that levels of atmospheric O_2 can be buffered by the crust at very low pO_2 values, consistent with theoretical predictions (*145*). We note, however, that the kinetics of sulfide dissolution for a range of other mineral phases and at the very low O_2 levels characteristic of the Archean remain to be explored. Alternatively, biological O_2 production may have occurred proximal to the subaerial weathering environment, perhaps even *in situ*, alleviating kinetic constraints.

The latter suggestion is meant to be more provocative than hypothetical, but we note that nearly all preserved Archean soil horizons (paleosols) contain measurable quantities of organic matter (*146*). In addition, there are good reasons to think that oxygenic photosynthesis could persist in subaerial settings even at very low pH values (e.g., *147*) and within a more deleterious light environment than that seen on the modern Earth (*148*). These issues can only be explored through more elaborate modeling of local weathering chemistry, variability in atmospheric and surface ocean chemistry, and more detailed empirical exploration of the possible role(s) of biology in subaerial weathering environments on the early Earth.

References:

1. Rosing MT, Frei R (2004) U-rich Archaean sea-floor sediments from Greenland – indications of >3700 Ma oxygenic photosynthesis. *Earth and Planetary Science Letters* **217**, 237-244.

2. Brocks JJ, Logan GA, Buick R, Summons RE (1999) Archean molecular fossils and the early rise of eukaryotes. *Science* **285**, 1033-1036.

3. Brocks JJ, Buick R, Summons RE, Logan GA (2003) A reconstruction of Archean biological diversity based on molecular fossils from the 2.78 to 2.45 billion-year-old Mount Bruce Supergroup, Hamersley Basin, Western Australia. *Geochimica et Cosmochimica Acta* **67**, 4321-4335.

4. Summons RE, Jahnke LL, Hope JM, Logan GA (1999) 2-Methylhopanoids as biomarkers for cyanobacterial oxygenic photosynthesis. *Nature* **400**, 554-557.

5. Rasmussen B, Fletcher IR, Brocks JJ, Kilburn MR (2008) Reassessing the first appearance of eukaryotes and cyanobacteria. *Nature* **455**, 1101-1104.

6. Kopp RE, Kirschvink JL, Hilburn IA, Nash CZ (2005) The Paleoproterozoic snowball Earth: A climate disaster triggered by the evolution of oxygenic photosynthesis. *Proceedings of the National Academy of Sciences USA* **102**, 11131-11136.

7. Bekker A, Holland HD, Wang P-L, Rumble D, Stein HJ, Hannah JL, Coetzee LL, Beukes NJ (2004) Dating the rise of atmospheric oxygen. *Nature* **427**, 117-120.

8. Hannah JL, Bekker A, Stein HJ, Markey RJ, Holland HD (2004) Primitive Os and 2316 Ma age for marine shale: implications for Paleoproterozoic glacial events and the rise of atmospheric oxygen. *Earth and Planetary Science Letters* **225**, 43-52.

9. Guo Q, Strauss H, Kaufman AJ, Schröder S, Gutzmer J, Wing B, Baker MA, Bekker A, Jin Q, Kim S-T, Farquhar J (2009) Reconstructing Earth's surface oxidation across the Archean-Proterozoic transition. *Geology* **37**, 399-402.

10. Anbar AD, Duan Y, Lyons TW, Arnold GL, Kendall B, Creaser RA, Kaufman AJ, Gordon GW, Scott C, Garvin J, Buick R (2007) A whiff of oxygen before the Great Oxidation Event? *Science* **317**, 1903-1906.

11. Kaufman AJ, Johnston DT, Farquhar J, Masterson AL, Lyons TW, Bates S, Anbar AD, Arnold GL, Garvin J, Buick R (2007) Late Archean biospheric oxygenation and atmospheric evolution. *Science* **317**, 1900-1903.

12. Wille M, Kramers JD, Nägler TF, Beukes NJ, Schröder S, Meisel T, Lacassie JP, Voegelin AR (2007) Evidence for a gradual rise of oxygen between 2.6 and 2.5 Ga from Mo isotopes and Re-PGE signatures in shales. *Geochimica et Cosmochimica Acta* **71**, 2417-2435.

13. Garvin J, Buick R, Anbar AD, Arnold GL, Kaufman AJ (2009) Isotopic evidence for an aerobic nitrogen cycle in the lastest Archean. *Science* **323**, 1045-1048.

14. Reinhard CT, Raiswell R, Scott C, Anbar AD, Lyons TW (2009) A late Archean sulfidic sea stimulated by early oxidative weathering of the continents. *Science* **326**, 713-716.

15. Frei R, Gaucher C, Poulton SW, Canfield DE (2009) Fluctuations in Precambrian atmospheric oxygenation recorded by chromium isotopes. *Nature* **461**, 250-253.

16. Duan Y, Anbar AD, Arnold GL, Lyons TW, Gordon GW, Kendall B (2010) Molybdenum isotope evidence for mild environmental oxygenation before the Great Oxidation Event. *Geochimica et Cosmochimica Acta* **74**, 6655-6668.

17. Kendall B, Reinhard CT, Lyons TW, Kaufman AJ, Poulton SW, Anbar AD (2010) Pervasive oxygenation along late Archaean ocean margins. *Nature Geoscience* **3**, 647-652.

18. Scott CT, Bekker A, Reinhard CT, Schnetger B, Krapež B, Rumble D, Lyons TW (2011) Late Archean euxinic conditions before the rise of atmospheric oxygen. *Geology* **39**, 119-122.

19. Kasting JF, Donahue TM (1980) The evolution of atmospheric ozone. *Journal of Geophysical Research* **85**, 3255-3263.

20. Kasting JF (1992) Models relating to Proterozoic atmospheric and ocean chemistry. *In* Schopf JW, Klein C (*eds.*), *The Proterozoic Biosphere: A Multidiscliplinary Study*. Cambridge University Press, New York, NY.

21. Fleet ME (2006) Phase equilibria at high temperatures. *Reviews in mineralogy and geochemistry* **61**, 365-419.

22. Postma D, Boesen C, Kristiansen H, Larsen F (1991) Nitrate reduction in an unconfined sandy aquifer: Water chemistry, reduction processes, and geochemical modeling. *Water Resources Research* **27**, 2027-2045.

23. Jørgensen CJ, Jacobsen OS, Elberling B, Aamand J (2009) Microbial oxidation of pyrite coupled to nitrate reduction in anoxic groundwater sediments. *Environmental Science & Technology* **43**, 4851-4857.

24. Torrentó C, Cama J, Urmeneta J, Otero N, Soler A (2010) Denitrification of groundwater with pyrite and *Thiobacillus denitrificans*. *Chemical Geology* **278**, 80-91.

25. Schippers A, Jørgensen BB (2001) Oxidation of pyrite and iron sulfide by manganese dioxide in marine sediments. *Geochimica et Cosmochimica Acta* **65**, 915-922.

26. Schippers A, Jørgensen BB (2002) Biogeochemistry of pyrite and iron sulfide oxidation in marine sediments. *Geochimica et Cosmochimica Acta* **66**, 85-92.

27. Luther GW, Sundby B, Lewis BL, Brendel PJ, Silverberg N (1997) Interactions of manganese with the nitrogen cycle: Alternative pathways to dinitrogen. *Geochimica et Cosmochimica Acta* **61**, 4043-4052.

28. Aller RC, Hall POJ, Rude PD, Aller JY (1998) Biogeochemical heterogeneity and suboxic diagenesis in hemipelagic sediments of the Panama Basin. *Deep-Sea Research I* **45**, 133-165.

29. Hulth S, Aller RC, Gilbert F (1999) Coupled anoxic nitrification/manganese reduction in marine sediments. *Geochimica et Cosmochimica Acta* **63**, 49-66.

30. Thamdrup B, Dalsgaard T (2000) The fate of ammonium in anoxic manganese oxide-rich marine sediment. *Geochimica et Cosmochimica Acta* **64**, 4157-4164.

31. Aller RC, Rude PD (1988) Complete oxidation of solid phase sulfides of manganese and bacterial in anoxic marine sediments. *Geochimica et Cosmochimica Acta* **52**, 751-765.

32. Diem D, Stumm W (1984) Is dissolved Mn^{2+} being oxidized by O_2 in absence of Mn-bacteria or surface catalysts? *Geochimica et Cosmochimica Acta* **48**, 1571-1573.

33. Williamson MA, Rimstidt JD (1994) The kinetics and electrochemical rate-determining step of aqueous pyrite oxidation. *Geochimica et Cosmochimica Acta* **58**, 5443-5454.

34. Evangelou VP, Zhang YL (1995) A Review: Pyrite oxidation mechanisms and acid mine drainage prevention. *Critical Reviews in Environmental Science and Technology* **25**, 141-199.

35. Straub KL, Benz M, Schink B, Widdel F (1996) Anaerobic, nitrate-dependent microbial oxidation of ferrous iron. *Applied and Environmental Microbiology* **62**, 1458-1460.

36. Benz M, Brune A, Schink B (1998) Anaerobic and aerobic oxidation of ferrous iron at neutral pH by chemoheterotrophic nitrate-reducing bacteria. *Archives of Microbiology* **169**, 159-165.

37. Meyers CR, Nealson KH (1988) Microbial reduction of manganese oxides: Interactions with iron and sulfur. *Geochimica et Cosmochimica Acta* **52**, 2727-2732.

38. Cairns-Smith, AG (1978) Precambrian solution photochemistry, inverse segregation, and banded iron formations. *Nature* **276**, 807-808.

39. Braterman PS, Cairns-Smith AG, Sloper RW (1983) Photo-oxidation of hydrated Fe^{2+} – significance for banded iron formations. *Nature* **303**, 163-164.

40. Widdel F, Schnell S, Heising S, Ehrenreich A, Assmus B, Schink B (1993) Ferrous iron oxidation by anoxygenic phototrophic bacteria. *Nature* **362**, 834-836.

41. François LM (1986) Extensive deposition of banded iron formations was possible without photosynthesis. *Nature* **320**, 352-354.

42. François LM (1987) Reducing power of ferrous iron in the Archean ocean, 2. Role of $FeOH^+$ photooxidation. *Paleoceanography* **2**, 395-408.

43. Anbar AD, Holland, HD (1992) The photochemistry of manganese and the origin of banded iron formations. *Geochimica et Cosmochimica Acta* **56**, 2595-2603.

44. Konhauser KO, Hamade T, Raiswell R, Morris RC, Ferris FG, Southam G, Canfield DE (2002) Could bacteria have formed the Precambrian banded iron formations? *Geology* **30**, 1079-1082.

45. Kappler A, Pasquero C, Konhauser KO, Newman DK (2005) Deposition of banded iron formations by anoxygenic phototrophic Fe(II)-oxidizing bacteria. *Geology* **33**, 865-868.

46. Konhauser KO, Amskold L, Lalonde SV, Posth NR, Kappler A, Anbar A (2007) Decoupling photochemical Fe(II) oxidation from shallow-water BIF deposition. *Earth and Planetary Science Letters* **258**, 87-100.

47. Kasting JF, Holland HD, Pinto JP (1985) Oxidant abundance in rainwater and the evolution of atmospheric oxygen. *Journal of Geophysical Research* **90**, 10497-10510.

48. Farquhar J, Savarino J, Airieau S, Thiemens MH (2001) Observation of wavelength-sensitive mass-independent sulfur isotope effects during SO_2 photolysis: Implications for the early atmosphere. *Journal of Geophysical Research* **106**, 32829-32839.

49. Millero FJ, Sotolongo S, Izaguirre M (1987) The oxidation kinetics of Fe(II) in seawater. *Geochimica et Cosmochimica Acta* **51**, 793-801.

50. Stumm W, Morgan JJ (1981) *Aquatic Chemistry: An introduction emphasizing chemical equilibria in natural waters*. Wiley, New York, NY.

51. Heising S, Richter L, Ludwig W, Schink B (1999) *Chlorobium ferrooxidans* sp. nov., a phototrophic green sulfur bacterium that oxidizes ferrous iron in coculture with a *"Geospirillum"* sp. strain. *Archives of Microbiology* **172**, 116-124.

52. Canfield DE, Thamdrup B, Kristensen E (2005) *Aquatic Geomicrobiology*. Advances in Marine Biology, 48, Elsevier, Oxford, UK.

53. Heising S, Schink B (1998) Phototrophic oxidation of ferrous iron by a *Rhodomicrobium vannielii* strain. *Microbiology* **144**, 2263-2269.

54. Kappler A, Newman DK (2004) Formation of Fe(III)-minerals by Fe(II)-oxidizing photoautotrophic bacteria. *Geochimica et Cosmochimica Acta* **68**, 1217-1226.

55. Runnegar B (1993) Algae and oxygen in Earth's ancient atmosphere. *Science* **259**, 835.

56. Kasting JF (1993) Algae and oxygen in Earth's ancient atmosphere. *Science* **259**, 835.

57. Ianson D, Allen SE (2002) A two-dimensional nitrogen and carbon flux model in a coastal upwelling region. *Global Biogeochemical Cycles* **16**, doi:10.1029/2001GB001451.

58. Canfield, DE (2006) Models of oxic respiration, denitrification and sulfate reduction in zones of coastal upwelling. *Geochimica et Cosmochimica Acta* **70**, 5753-5765.

59. Kump LR, Pavlov A, Arthur MA (2005) Massive release of hydrogen sulfide to the surface ocean and atmosphere during intervals of oceanic anoxia. *Geology* **33**, 397-400.

60. Chavez FP, Messié M (2009) A comparison of Eastern Boundary Upwelling Ecosystems. *Progress in Oceanography* **83**, 80-96.

61. Messié M, Ledesma J, Kolber DD, Michisaki RP, Foley DG, Chavez FP (2009) Potential new production estimates in four eastern boundary upwelling systems. *Progress in Oceanography* **83**, 151-158.

62. Smith SD (1980) Wind stress and heat flux over the ocean in gale force winds. *Journal of Physical Oceanography* **10**, 709-726.

63. Hasse L, Smith SD (1997) Local sea surface wind, wind stress, and sensible and latent heat fluxes. *Journal of Climate* **10**, 2711-2724.

64. Rykaczewski RR, Checkley DM (2008) Influence of ocean winds on the pelagic ecosystem in upwelling regions. *Proceedings of the National Academy of Sciences USA* **105**, 1965-1970.

65. Chelton DB, de Szoeke RA, Schlax MG, El Naggar K, Siwertz N (1998) Geographical variability of the first baroclinic Rossby radius of deformation. *Journal of Physical Oceanography* **28**, 433-460.

66. Estrade P, Marchesiello P, De Veridére AC, Roy C (2008) Cross-shelf structure of coastal upwelling: A two-dimensional extension of Ekman's theory and a mechanism for inner shelf upwelling shut down. *Journal of Marine Research* **66**, 589-616.

67. Garcia HE, Gordon LI (1992) Oxygen solubility in seawater: Better fitting equations. *Limnology & Oceanography* **37**, 1307-1312.

68. Wanninkhof R (1992) Relationship between wind speed and gas exchange over the ocean. *Journal of Geophysical Research* **97**, 7373-7382.

69. Sharqawy MH, Lienhard JH, Zubair SM (2010) Thermophysical properties of seawater: a review of existing correlations and data. *Desalination and Water Treatment* **16**, 354-380.

70. Schulz HD (2006) Quantification of early diagenesis: Dissolved constituents in pore water and signals in the solid phase. *In* Schulz HD, Zabel M (*eds*.), *Marine Geochemistry*. Springer, Heidelberg, Germany.

71. Emerson SR, Hedges JI (2008) *Chemical Oceanography and the Marine Carbon Cycle*. Cambridge University Press, New York, NY.

72. Anderson DM, Brock JC, Prell WL (1992) Physical upwelling processing, upper ocean environment and the sediment record of the southwest monsoon. *Geological Society Special Publications* **64**, 121-129.

73. Anderson LA, Sarmiento JL (1994) Redfield ratios of remineralization determined by nutrient data analysis. *Global Biogeochemical Cycles* **8**, 65-80.

74. Sarmiento JL, Gruber N (2006) *Ocean Biogeochemical Dynamics*. Princeton University Press, Princeton, NJ.

75. Emerson D, Fleming EJ, McBeth JM (2010) Iron-oxidizing bacteria: An environmental and genomic perspective. *Annual Reviews of Microbiology* **64**, 561-583.

76. Reeburgh WS (2007) Oceanic methane biogeochemistry. *Chemical Reviews* **107**, 486-513.

77. Pavlov AA, Kasting JF (2002) Mass-independent fractionation of sulfur isotopes in Archean sediments: Strong evidence for an anoxic Archean atmosphere. *Astrobiology* **2**, 27-41.

78. Pavlov AA, Brown LL, Kasting JF (2001) UV shielding of NH_3 and O_2 by organic hazes in the Archean atmosphere. *Journal of Geophysical Research* **106**, 23267-23287.

79. Claire MW, Catling DC, Zahnle KJ (2006) Biogeochemical modelling of the rise in atmospheric oxygen. *Geobiology* **4**, 239-269.

80. Holland HD (2003) The geological history of seawater. *In* Holland HD, Turekian KK (*eds*.), *Treatise on Geochemistry* **6**, 583-625.

81. Canfield, DE (2005) The early history of atmospheric oxygen: Homage to Robert M. Garrels. *Annual Review of Earth and Planetary Sciences* **33**, 1-36.

82. Morris RC (1993) Genetic modelling for banded iron-formation of the Hamersley Group, Pilbara Craton, Western Australia. *Precambrian Research* **60**, 243-286.

83. Knab NJ, Dale AW, Lettmann K, Fossing H, Jørgensen BB (2008) Thermodynamics and kinetic control on anaerobic oxidation of methane in marine sediments. *Geochimica et Cosmochimica Acta* **72**, 3746-3757.

84. Riedinger N, Brunner B, Lin Y-S, Voßmeyer A, Ferdelman TG, Jørgensen BB (2010) Methane at the sediment-water transition in Black Sea sediments. *Chemical Geology* **274**, 29-37.

85. Canfield DE, Habicht KS, Thamdrup, B (2000) The Archean sulfur cycle and the early history of atmospheric oxygen. *Science* **288**, 658-661.

86. Habicht KS, Gade M, Thamdrup B, Berg P, Canfield DE (2002) Calibration of sulfate levels in the Archean ocean. *Science* **298**, 2372-2374.

87. Crowe SA, Katsev S, Leslie K, Sturm A, Magen C, Nomosatryo S, Pack MA, Kessler JD, Reeburgh WS, Roberts JA, González L, Haffner GD, Mucci A, Sundby B, Fowle DA. The methane cycle in ferruginous Lake Matano. *Geobiology* **9**, 61-78.

88. Goldhaber MB (1983) Experimental study of metastable sulfur oxyanion formation during pyrite oxidation at pH 6-9 and 30ºC. *American Journal of Science* **283**, 193-217.

89. McKibben MA, Barnes HL (1986) Oxidation of pyrite in low temperature acidic solutions: Rate laws and surface textures. *Geochimica et Cosmochimica Acta* **50**, 1509-1520.

90. Moses CO, Nordstrom DK, Herman JS, Mills AL (1987) Aqueous pyrite oxidation by dissolved oxygen and by ferric iron. *Geochimica et Cosmochimica Acta* **51**, 1561-1571.

91. Moses CO, Herman JS (1991) Pyrite oxidation at circumneutral pH. *Geochimica et Cosmochimica Acta* **55**, 471-482.

92. Langmuir D (1997) *Aqueous Environmental Geochemistry*. Prentice Hall, NJ.

93. de Waal SA, Calk LC (1973) The sulfides in the garnet pyroxenite xenoliths from Salt Lake Crater, Oahu. *Journal of Petrology* **16**, 134-153.

94. Aftabi A, Ghodrati Z, MacLean WH (2006) Metamorphic textures and geochemistry of the Cyprus-type massive sulfide lenses at Zurabad, Khoy, Iran. *Journal of Asian Earth Sciences* **27**, 523-533.

95. Taylor KG, Macquaker JHS (2011) Iron minerals in marine sediments record chemical environments. *Elements* **7**, 113-118.

96. Meysman FJR, Galaktionov OS, Madani S, Middelburg JJ (2005) Modelling biological interactions in aquatic sediments as coupled reactive transport. *Coastal and Estuarine Studies* **60**, 359-388.

97. Berner RA (1964) An idealized model of dissolved sulfate distribution in recent sediments. *Geochimica et Cosmochimica Acta* **28**, 1497-1503.

98. Boudreau BP, Ruddick BR (1991) On a reactive continuum representation of organic matter diagenesis. *American Journal of Science* **291**, 507-538.

99. Rothman DH, Forney DC (2007) Physical model for the decay and preservation of marine organic carbon. *Science* **316**, 1325-1328.

100. Berner, RA (1978) Sulfate reduction and the rate of deposition of marine sediments. *Earth and Planetary Science Letters* **37**, 492-498.

101. Berner RA (1980) *Early Diagenesis: A Theoretical Approach*. Princeton Univ. Press, Princeton, NJ.

102. Aller RC, Mackin JE (1984) Preservation of reactive organic matter in marine sediments. *Earth and Planetary Science Letters* **70**, 260-266.

103. Boudreau BP, Westrich JT (1984) The dependence of bacterial sulfate reduction on sulfate concentration in marine sediments. *Geochimica et Cosmochimica Acta* **48**, 2503-2516.

104. Westrich JT, Berner RA (1984) The role of sedimentary organic matter in bacterial sulfate reduction: The *G* model tested. *Limnology & Oceanography* **29**, 236-249.

105. Carignan R, Lean DRS (1991) Regeneration of dissolved substances in a seasonally anoxic lake: The relative importance of processes occurring in the water column and in the sediments. *Limnology & Oceanography* **36**, 683-707.

106. Rabouille C, Gaillard J-F (1991a) Towards the EDGE: Early diagenetic global explanation. A model depicting the early diagenesis of organic matter, O_2, NO_3, Mn, and PO_4. *Geochimica et Cosmochimica Acta* **55**, 2511-2525.

107. Rabouille C, Gaillard J-F (1991b) A coupled model representing the deep-sea organic carbon mineralization and oxygen consumption in surficial sediments. *Journal of Geophysical Research* **96**, 2761-2776.

108. Van Cappellen P, Want Y (1996) Cycling of iron and manganese in surface sediments: A general theory for the coupled transport and reaction of carbon, oxygen, nitrogen, sulfur, iron, and manganese. *American Journal of Science* **296**, 197-243.

109. Wang Y, Van Cappellen P (1996) A multicomponent reactive transport model of early diagenesis: Application to redox cycling in coastal marine sediments. *Geochimica et Cosmochimica Acta* **60**, 2993-3014.

110. Berg P, Rysgaard S, Thamdrup B (2003a) Dynamic modeling of early diagenesis and nutrient cycling. A case study in an Arctic marine sediments. *American Journal of Science* **303**, 905-955.

111. Katsev S, Sundby B, Mucci A (2006) Modeling vertical excursions of the redox boundary in sediments: Application to deep basins of the Arctic Ocean. *Limnology & Oceanography* **51**, 1581-1593.

112. Rabouille C, Gaillard J-F, Relexans J-C, Tréguer P, Vincendeau M-A (1998) Recycling of organic matter in Antarctic sediments: A transect through the polar front in the Southern Ocean (Indian Sector). *Limnology & Oceanography* **43**, 420-432.

113. Middelburg JJ, Soetaert K, Herman PMJ, Heip CHR (1996) Denitrification in marine sediments: A model study. *Global Biogeochemical Cycles* **10**, 661-673.

114. Middelburg JJ, Soetaert K, Herman PMJ (1997) Empirical relationships for use in global diagenetic models. *Deep-Sea Research I* **44**, 327-344.

115. Soetaert K, Herman PMJ, Middelburg JJ (1996) A model of early diagenetic processes from the shelf to abyssal depths. *Geochimica et Cosmochimica Acta* **60**, 1019-1040.

116. Middelburg JJ (1989) A simple rate model for organic matter decomposition in marine sediments. *Geochimica et Cosmochimica Acta* **53**, 1577-1581.

117. Middelburg JJ, Vlug T, van der Nat FJWA (1993) Organic matter mineralization in marine systems. *Global and Planetary Change* **8**, 47-58.

118. Tromp TK, Van Cappellen P, Key RM (1995) A global model for the early diagenesis of organic carbon and organic phosphorus in marine sediments. *Geochimica et Cosmochimica Acta* **59**, 1259-1284.

119. Revsbech NP, Sørensen J, Blackburn TH, Lomholt JP (1980) Distribution of oxygen in marine sediments measured with microelectrodes. *Limnology & Oceanography* **25**, 403-411.

120. Archer D, Emerson S, Smith CR (1989) Direct measurement of the diffusive sublayer at the deep sea floor using oxygen microelectrodes. *Nature* **340**, 623-626.

121. Jørgensen BB, Revsbech NP (1985) Diffusive boundary layers and the oxygen uptake of sediments and detritus. *Limnology & Oceanography* **30**, 111-122.

122. Gundersen JK, Jørgensen BB (1990) Microstructure of diffusive boundary layers and the oxygen uptake of the sea floor. *Nature* **345**, 604-607.

123. Archer D, Devol A (1992) Benthic oxygen fluxes on the Washington shelf and slope: A comparison of in situ microelectrode and chamber flux measurements. *Limnology & Oceanography* **37**, 614-629.

124. Rasmussen H, Jørgensen BB (1992) Microelectrode studies of seasonal oxygen uptake in a coastal sediments: role of molecular diffusion. *Marine Ecology Progress Series* **81**, 289-303.

125. Thamdrup B, Glud RN, Hansen JW (1994) Manganese oxidation and in situ manganese fluxes from a coastal sediments. *Geochimica et Cosmochimica Acta* **58**, 2563-2570.

126. Reimers CE, Ruttenberg KC, Canfield DE, Christiansen MB, Martin JB (1996) Porewater pH and authigenic phases formed in the uppermost sediments of the Santa Barbara Basin. *Geochimica et Cosmochimica Acta* **60**, 4037-4057.

127. Berg P, Risgaard-Petersen N, Rysgaard S (1998) Interpretation of measured concentration profiles in sediment pore water. *Limnology & Oceanography* **43**, 1500-1510.

128. Berg P, Røy H, Janssen F, Meyer V, Jørgensen BB, Huettel M, de Beer D (2003b) Oxygen uptake by aquatic sediments measured with a novel non-invasive eddy-correlation technique. *Marine Ecology Progress Series* **261**, 75-83.

129. Rabouille C, Denis L, Dedieu K, Stora G, Lansard B, Grenz C (2003) Oxygen demand in coastal marine sediments: comparing in situ microelectrodes and laboratory core incubations. *Journal of Experimental Marine Biology and Ecology* **285-286**, 49-69.

130. Glud RN, Berg P, Fossing H, Jørgensen BB (2007) Effect of the diffusive boundary layer on benthic mineralization and O_2 distribution: A theoretical modeling analysis. *Limnology & Oceanography* **52**, 547-557.

131. Henrichs SM, Reeburgh WS (1987) Anaerobic mineralization of marine sediment organic matter: Rates and the role of anaerobic processes in the oceanic carbon economy. *Geomicrobiology Journal* **5**, 191-237.

132. Canfield DE, Thamdrup B, Hansen JW (1993) The anaerobic degradation of organic matter in Danish coastal sediments: Iron reduction, manganese reduction, and sulfate reduction. *Geochimica et Cosmochimica Acta* **57**, 3867-3883.

133. Schlesigner WH (1990) Evidence from chronosequence studies for a low carbon-storage potential of soils. *Nature* **348**, 232-234.

134. Taylor A, Blum JD (1995) Relation between soil age and silicate weathering rates determined from the chemical evolution of a glacial chronosequence. *Geology* **23**, 979-982.

135. Pillans B (1997) Soil development at snail's pace: evidence from a 6 Ma soil chronosequence on basalt in north Queensland, Australia. *Geoderma* **80**, 117-128.

136. Torn MS, Trumbore SE, Chadwick OA, Vitousek PM, Hendricks DM (1997) Mineral control of soild organic carbon storage and turnover. *Nature* **389**, 170-173.

137. Targulian VO, Krasilnikov PV (2007) Soil system and pedogenic processes: Self-organization, time scales, and environmental significance. *Catena* **71**, 373-381.

138. Gleisner M, Herbert RB, Kockum PCF (2006) Pyrite oxidation by *Acidothiobacillus ferrooxidans* at various concentrations of dissolved oxygen. *Chemical Geology* **225**, 16-29.

139. Singer PC, Stumm W (1970) Acidic mine drainage: The rate-determining step. *Science* **167**, 1121-1123

140. Konhauser KO, Lalonde SV, Planavsky NJ, Pecoits E, Lyons TW, Mojzsis SJ, Rouxel OJ, Barley ME, Rosíere C, Fralick PW, Kump LR, Bekker A (2011) Aerobic bacterial pyrite oxidation and acid rock drainage during the Great Oxidation Event. *Nature* **478**, 369-373.

141. Planavsky N, Bekker A, Rouxel OJ, Kamber B, Hofmann A, Knudsen A, Lyons TW (2010) Rare Earth element and yttrium compositions of Archean and Paleoproterozoic Fe formations revisited: New perspectives on the significance and mechanisms of deposition. *Geochimica et Cosmochimica Acta* **74**, 6387-6405.

142. Zahnle K, Claire M, Catling D (2006) The loss of mass-independent fractionation in sulfur due to a Palaeoproterozoic collapse of atmospheric methane. *Geobiology* **4**, 271-283.

143. Waldbauer JR, Newman DK, Summons RE (2011) Microaerobic steroid biosynthesis and the molecular fossil record of Archean life. *Proceedings of the National Academy of Sciences USA* **108**, 13409-13414.

144. Haqq-Misra J, Kasting JF, Lee S (2011) Availability of O_2 and H_2O_2 on pre-photosynthetic Earth. *Astrobiology* **11**, 293-302.

145. Sverjensky DA, Lee N (2010) The Great Oxidaiton Event and mineral diversification. *Elements* **6**, 31-36.

146. Watanabe Y, Stewart BW, Ohmoto H (2004) Organic- and carbonate-rich soil formation ~2.6 billion years ago at Schagen, East Transvaal district, South Africa. *Geochimica et Cosmochimica Acta* **68**, 2129-2151.

147. Seckbach J, Oren A (2007) Oxygenic photosynthetic microorganisms in extreme environmenst: Possibilities and limitations. *Cellular Origin, Life in Extreme Habitats and Astrobiology* **11**, 3-25.

148. Cockell CS, Raven JA (2007) Ozone and life on the Archaean Earth. *Philosophical Transactions of the Royal Society A* **365**, 1889-1901.

CHAPTER 4

LONG-TERM SEDIMENTARY RECYCLING OF RARE SULFUR ISOTOPE ANOMALIES AND ITS SIGNIFICANCE FOR RECONSTRUCTING ATMOSPHERIC EVOLUTION

Preface:

The contents of this chapter represent a manuscript in preparation for submission to the journal *Nature.* This is reflected in the formatting.

Introduction:

The accumulation of significant quantities of O_2 in the atmosphere has come to control the chemistry and ecological structure of Earth's surface, ultimately allowing for the evolution and expansion of complex life. Over the last decade, non-mass-dependent (NMD) sulphur isotope anomalies within the rock record (*1*) have been the central tool used to reconstruct the redox history of the early atmosphere. The generation and initial delivery of these anomalies to marine sediments requires low partial pressures of atmospheric O_2 (pO_2; *2, 3*), and it is now widely assumed that atmospheric oxygen levels remained extremely low for the first ~2 billion years of Earth's history. Here, we show with a model designed to capture the long-term surface recycling of crustal NMD anomalies that the record of this geochemical signal is likely to show a 'crustal memory effect' following increases in atmospheric pO_2 above ~10^{-5} times the present atmospheric level (PAL). Once NMD anomalies have been buried into the upper crust they are extremely resistant to removal and can only be erased through successive cycles of weathering, dilution, and burial in a mass-dependent, oxygenated world. This recycling results in the residual incorporation of NMD anomalies into the sedimentary record long after synchronous atmospheric generation of the isotopic signal has ceased, with measurable signals likely preserving for 50-100 million years subsequent to a rise of atmospheric oxygen beyond 10^{-5} PAL. Our results can reconcile geochemical evidence for strong oxidative weathering despite the maintenance of NMD anomalies on the early Earth (*4-6*) and suggest that future work should be aimed at testing our assertion that the generation of new NMD sulphur isotope anomalies under vanishingly small O_2 concentrations in the atmosphere must have ceased long before their ultimate disappearance from the rock record.

Main Article:

One of the most important recent advances in studies of Earth's early atmospheric chemistry has been the demonstration that non-mass-dependent (NMD) sulphur isotope anomalies, often of very large magnitude, are preserved in sedimentary sulphide and sulphate minerals prior to ~2.32 billion years ago (*1, 7*). The generation of these anomalies requires (1) active and widespread tropospheric photochemistry involving SO_2 dissociation at short wavelengths, which in turn implies minimal ozone column depth (*2*); (2) a strongly reducing atmosphere, such that multiple exit channels for sulphur at different redox states can be maintained (*3*, *8*); and, (3) minimal metabolic overprinting of atmospherically derived isotope anomalies within marine environments (*9*). The latter two conditions result from simple mass balance—even if NMD anomalies are generated in the atmosphere, isotopically complementary sulphur pools must be removed from the atmosphere and transported to marine sediments with minimal homogenization by inorganic or biological processes. Under these conditions, photochemically derived sulphur with NMD isotope anomalies will be delivered to the hydrosphere and ultimately buried as a constituent of various sulphur-bearing mineral phases, such as pyrite (FeS_2). The presence of these anomalies at varying magnitude between the earliest sedimentary record at ~3.8 Ga and ~2.32 Ga is interpreted to reflect a strongly reducing atmosphere over this entire interval, with the implication that atmospheric pO_2 was extremely low for over half of Earth's history (Fig. 4.1a). Implicit in this framework is the notion that the generation and transfer of these anomalies into the upper crust through the burial of authigenic marine minerals provides an effectively instantaneous record of ambient atmospheric chemistry, but this assumption ignores the potential importance of sedimentary recycling.

There is a striking asymmetry in the $\Delta^{33}S$ record through Archean time (Fig. 4.1a, b), with the data skewed in favor of positive $\Delta^{33}S$ values. Importantly, it is the preservation (and associated crustal recycling) of this NMD sulphur isotope asymmetry that allows for the possibility of a temporal lag between generation and ultimate removal of the signal from the oceanic sulphur reservoir. We emphasize that although there are likely several mechanistic explanations for this pattern (*10-12*), what matters foremost for our purposes is the veracity of this empirical observation, regardless of mechanism. This observed asymmetry would only be misleading if (1) a sedimentary sulphate reservoir with a complementary negative isotopic composition were deposited synchronous with the generation of the record shown in Fig. 4.1 but has not been preserved through geologic time, or (2) seawater sulphate with the negative $\Delta^{33}S$ complement was thermochemically or microbially reduced and buried into a weatherable sedimentary sulphide reservoir, but this reservoir has been strongly undersampled.

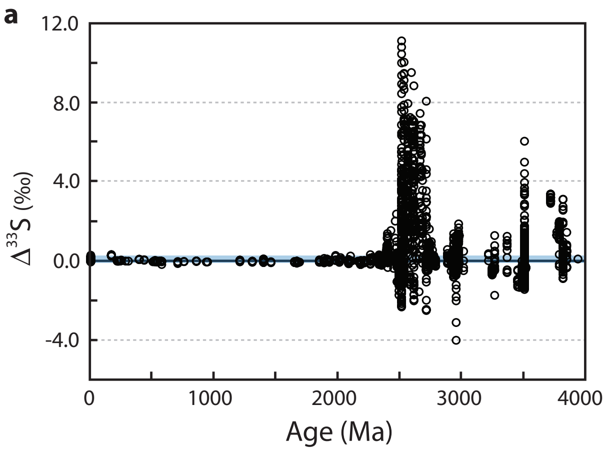

Figure 4.1. The rare sulphur isotope record through time. **a**, Data are cast as $\Delta^{33}S$ [where $\Delta^{33}S = \delta^{33}S - 0.515*\delta^{34}S$; reported in permil (‰)] versus time, in millions of years before the present (Ma). The shaded box denotes the average ±2SD of all post-2200 Ma data. **b**, The cumulative average $\Delta^{33}S$ anomaly as a function of database age. Filled circles show the cumulative average $\Delta^{33}S$ value for the database through time, with the blue boxes denoting the 95% confidence interval. See Supplementary Information for database details.

In the first case, analysis of the more abundant sulphur isotopes (^{34}S and ^{32}S) indicates that essentially all sulphur entering the Earth surface system was removed as a constituent of pyrite during the Archean (*13*, *14*), leaving little scope for an isotopically complementary reservoir that has left no trace on the modern Earth. Consistent with this, extremely low seawater sulphate concentrations during the Archean (*15*) would likely have rendered large-scale evaporite formation and burial extremely difficult. In the second case, the cumulative average for published $\Delta^{33}S$ values has continued to point to a predominance of positive values as the Archean rare sulphur isotope database increases in size, while the confidence interval around the mean has continually decreased (Fig. 4.1b). This relationship strongly suggests that the asymmetry towards positive values does not reflect a sampling bias.

To explore the implications of this for long-term recycling of NMD sulphur isotope anomalies we utilize a well-established numerical modeling approach to quantify the importance of recycling $\Delta^{33}S$ signals between the ocean and upper crust (Fig. 4.2). The model begins with a variation on a class of simple box models used to describe the surface cycling of carbon and sulphur during Phanerozoic time, termed "rapid recycling" models (*16-19*). This group of models and our specific approach are variants on models for global C-S-O cycling that have been used for decades to explore the dynamics of these biogeochemical cycles at Earth's surface (*20*, *21*). Such models have been used extensively to derive atmospheric O_2 and CO_2 predictions that compare well with independent proxy reconstructions of atmospheric composition during the Phanerozoic (*22*, *23*).

Our model, which tracks only sulphur, partitions sulphur into three reservoirs—the oceanic sulphate pool and two crustal reservoirs of sedimentary pyrite (Fig. 4.2). The two crustal reservoirs are referred to as 'young' and 'old', and the primary difference between them other than their overall mass is the speed at which they are recycled. The models build from geologically reasonable premise that the most recently deposited sediments are more likely to be recycled on a short time scale, but that the overall size of this sedimentary reservoir is relatively small. Fluxes between reservoirs are predominantly first-order; their magnitude depends on the size of the reservoir from which the flux is derived. Two notable exceptions are volcanic inputs, imposed as a constant flux and meant to encompass all processes introducing isotopically normal (non-NMD) sulphur to the ocean, and the flux between the two crustal pyrite reservoirs, which is set equal to the weathering flux from the old pyrite reservoir such that the mass of this reservoir does not change (*16*).

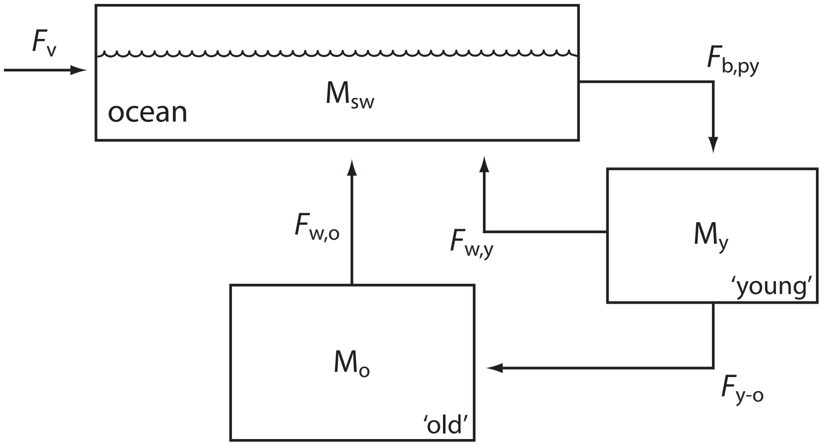

Figure 4.2. Schematic of the sulphur isotope mass balance model used in this study. Arrows denote flux terms (labeled "F_i"), while boxes denote various oceanic and crustal sulphur reservoirs (labeled "M_i").

Our main interest here is tracking the Δ^{33}S of seawater sulphate, as this signal will be directly incorporated into sedimentary sulphide minerals under the logical assumption that all subsequent isotope fractionations are mass-dependent. We note, however, that there may have been spatial isotopic heterogeneity within the ocean if marine sulphate concentrations were low. In effect, the NMD sulphur isotope signal behaves as a conservative tracer when cycled through a purely mass-dependent Earth surface sulphur cycle. In our model, the isotopic composition of seawater sulphate will evolve through time according to (see Supplementary Information):

$$M_{sw}\frac{d\delta_{sw}^{3x}}{dt} = \sum_{i} F_i(\delta_i^{3x} - \delta_{sw}^{3x}) - F_{b,py}\Delta_{py}^{3x} \, , \tag{4.1}$$

where M_{sw} is the oceanic mass of seawater sulphate, i refers to input fluxes to the ocean (volcanic and weathering fluxes), $F_{b,py}$ refers to the pyrite burial flux, Δ refers to the isotopic fractionation between seawater sulphate and sedimentary pyrite, and $x = 3, 4, 6$.

The model tracks all four stable sulphur isotopes and includes a parameterization of biologically induced isotope fractionation, but we restrict our attention here to the Δ^{33}S composition of sedimentary pyrite formed from chemical or microbial reduction of seawater sulphate, which is derived primarily from the weathering of pyrite. To most clearly illustrate the importance of sedimentary recycling of Δ^{33}S signals, it is assumed at the beginning of each model run that atmospheric pO_2 increases instantaneously above values that allow for the generation/preservation of NMD sulphur anomalies. All isotope fractionations imposed thereafter are mass-dependent and are controlled by metabolic fractionation during microbial sulphate reduction described as a function of ambient seawater sulphate concentration (see Supplementary Information). For the purposes of illustration, our simulations are initialized with a conventional Archean seawater sulphate concentration of 200 μM (*15*), a Δ^{33}S value for seawater sulphate of -1.0‰ [consistent with expectations from photochemical experiments[2] and analyses of Archean sulphates (*1*, *24*, *25*) and seafloor sulphide minerals (*8*, *24*)], and various values for the initial Δ^{33}S of rapidly weathering sedimentary pyrite. We stress, however, that these starting values are only meant to be illustrative. Our goal is to explore the time scales at which crustal recycling of NMD isotope anomalies can be expected to leave an imprint on the isotopic composition of the oceanic sulphate reservoir rather than to simulate specific features of the sedimentary NMD sulphur record. That latter goal lies with future research.

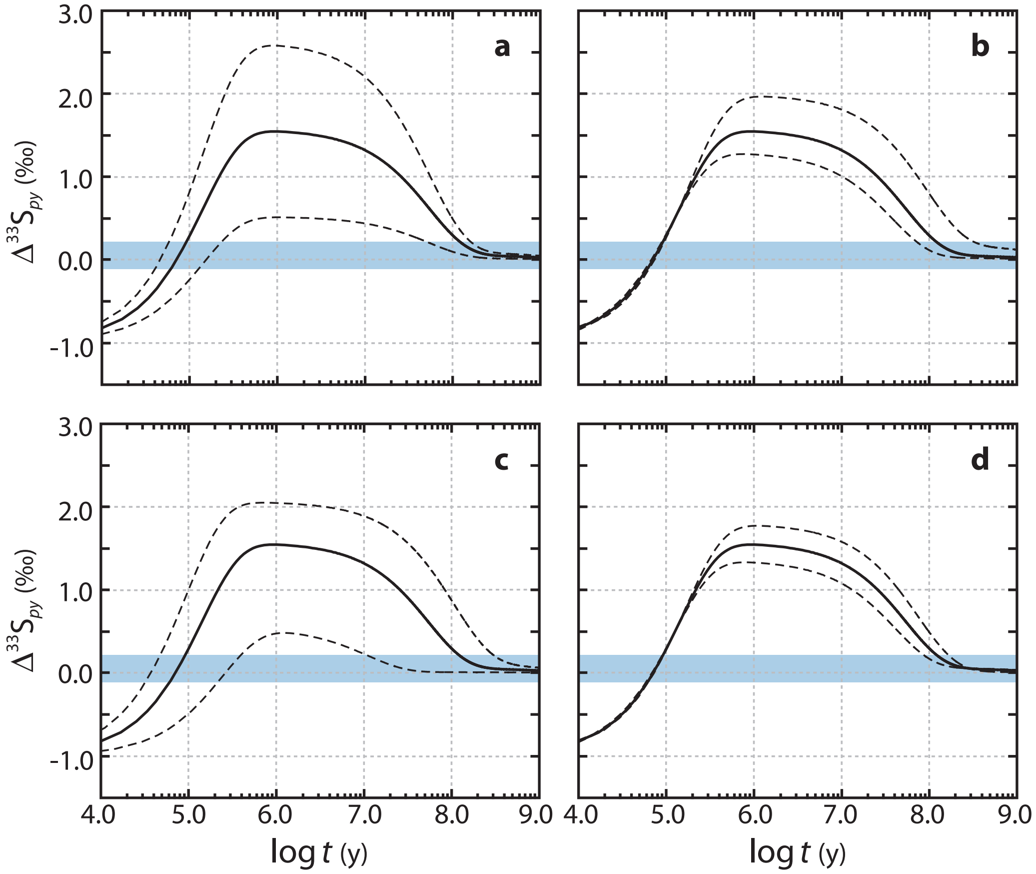

Figure 4.3. Overview of modeling results for the sedimentary recycling of rare sulphur isotope anomalies. The black solid curve in all cases represents the reference model (see Supplementary Information). Dashed curves represent sensitivity analyses as follows – increasing and decreasing the $\Delta^{33}S$ of the rapidly weathering pyrite reservoir by 2‰ (**a**); a range of mass-dependent sulphur fluxes between 2 x 10^{11} mol y^{-1} and 1 x 10^{12} mol y^{-1} (**b**); increasing and decreasing, by factors of 2 and 5, respectively, the initial size of the rapidly weathering pyrite reservoir (**c**); increasing and decreasing, by factors of 2 and 5, respectively, the size of the slowly weathering pyrite reservoir (**d**). The shaded box denotes the average ±2SD of all post-2200 Ma data. Note the log-scale with respect to time.

It is clear that there is a significant ‘memory effect’ associated with the sedimentary recycling of $\Delta^{33}S$ anomalies (Fig. 4.3a-d), the texture of which can vary depending on the time scale allowed for relaxation. This texture is difficult to avoid given what we consider to be reasonable parameter space. For example, a significant drop in the magnitude of residual $\Delta^{33}S$ values can be achieved by decreasing the size of the rapidly weathering pyrite reservoir from that in the reference model by a factor of 5 (Fig. 4.3c), but this results in geologically unreasonable fluxes and residence times relative to observed mass- and area-age distributions of weatherable sedimentary rocks (*26-28*) and time scales of cycling through the Earth surface sulphur reservoir (*29*). Rather ironically, once NMD isotope fractionations have been introduced into the system in an asymmetric fashion the best “taphonomic” conditions for their preservation involve a world in which all isotope fractionations are mass-dependent. This condition prevents homogenization, either locally or at a broad spatial scale, through mixing with isotopically complementary pools.

A residual NMD isotope signal that can be incorporated into sedimentary rocks can persist in our model on the order of ~100 million years or more beyond the cessation of its atmospheric production. However, it is difficult to extend the memory effect beyond ~200-250 million years (i.e., on the order of a single Wilson cycle; Fig. 4.3a-d). It can also decay on a time scale of ~20-50 million years, but the most plausible initial parameters (see Supplementary Information) yield our preferred estimate of approximately 50-100 million-years. In addition, the texture of the decay (regardless of the ultimate time scale of the memory effect) will depend strongly on the initial $\Delta^{33}S$

value of seawater sulphate and the initial size of the seawater sulphate reservoir—larger seawater sulphate concentrations will result in greater temporal inertia as the system moves towards the isotopic properties of the weathering input with positive $\Delta^{33}S$. An important outcome of this situation is that oscillations in atmospheric pO_2 near the threshold for the generation and synchronous preservation of NMD isotope anomalies may be expected to produce a wide range of temporal responses depending on the speed and fabric of the oscillation.

It is commonly argued that biological oxygen production preceded the broad-scale and effectively permanent accumulation of oxygen in Earth's atmosphere by perhaps 200 million years or more (*4-6*, *30-33*). Consistent with oxygenation prior to the so-called Great Oxidation Event (GOE), some data imply oxidative weathering over this interval (*4-6*). Our model suggests the possibility of perhaps long-lived excursions in atmospheric O_2 content above that required to generate and preserve NMD sulphur isotope anomalies in marine sediments long before the disappearance of these signals from the record, on time scales more than adequate to support extensive oxidative weathering of crustal minerals (*4*, *6*, *34*). The toggling of atmospheric generation of NMD isotope anomalies on a range of time scales (10^5 – 10^8 years) would not be immediately manifest in the removal of these signals from the rock record due to the recycling effect. It has been suggested that the behavior of O_2 in a relatively reducing atmosphere prior to its accumulation to significant levels is likely to be characterized by strong hysteresis[35]—such that excursions to 'high' O_2 (above ~10^{-5} PAL) may not be readily undone. Nevertheless, with atmospheric pO_2 values (and thus residence times) far below those characteristic of the modern Earth we would naturally expect high-frequency oscillations in atmospheric pO_2 in a world in which biological oxygen production was emergent and the interplay between this metabolism and inorganic buffering processes may have varied in ways that were periodic.

Importantly, our model implies that the ultimate disappearance of NMD sulphur isotope anomalies from the rock record should have been preceded by an irreversible rise in atmospheric O_2 during the late Archean by at least ~50-100 million years. As discussed above, the model also permits oscillatory behavior for the oxygen cycle during earlier portions of Archean time (*36*), as NMD signals would persists even as pO_2 rose and fell on timescales of millions of years. Combined, these results suggest that the texture of atmospheric redox evolution on the early Earth may have been highly dynamic and may call into question the notion of a Great Oxidation Event *sensu stricto*—in other words, that it is possible to pinpoint a moment in Earth history when oxygen rose permanently to levels above those required to support the production and preservation of NMD anomalies in the atmosphere. In this light, our model suggests that many of the climatological and geochemical upheavals witnessed by the Archean-Proterozoic transition, including the earliest recorded widespread glaciations (*37*) and the deposition of perhaps the largest iron and manganese deposits in all of Earth's history (*38*), may have been tied more directly to excursions in atmospheric O_2 content than current interpretations of the rare sulphur isotope record afford. The details of oscillatory redox behavior and the timing of oxygen's irreversible rise, along with placing further constraints on the input parameters controlling the fabric and lags in the NMD record, are fodder for future research. Nevertheless, recycling of crustal sulphur with relict NMD isotope anomalies must be considered in further attempts to quantitatively explore the paleoenvironmental and paleobiological implications of the Archean sulphur isotope record.

Supplementary Information:

Sulphur Isotope Database:

An extensive sulphur isotope database was used in the construction of Figure 4.1. These data were compiled from primary references (*1*, *7*, *10*, *30*, *39-69*), although in some cases age constraints for certain units were obtained from other sources (*70-73*) or estimated. For Figure 4.1b, we calculated the cumulative average $\Delta^{33}S$ value for all samples up to each year of publication. The average values reported here thus include some contribution from sulphate minerals. However, the overwhelming majority of the data are sulphide mineral phases, and given that most sulphate data are characterized by negative $\Delta^{33}S$ values their inclusion will largely attenuate the pattern emphasized here, rendering our argument conservative. The overall effect is quite small (Fig. 4.S1a,b). We also examined the effect of filtering data from analyses made via secondary ion mass spectrometry (SIMS) and analyses of macroscopic pyrite textures, which are not likely to be representative, but again note that the basic pattern remains unchanged (Fig. 4.S1a,b).

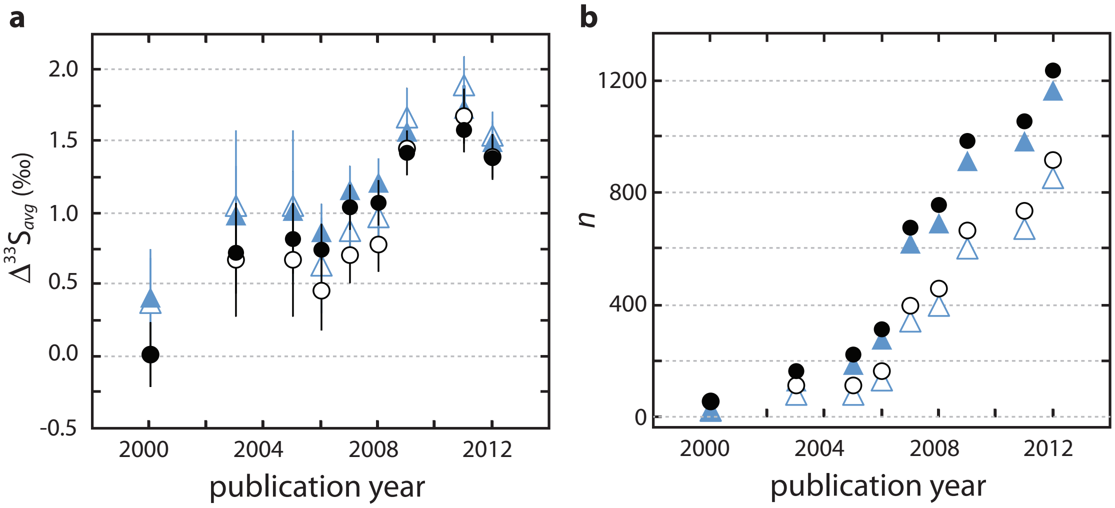

Figure 4.S1. Cumulative average $\Delta^{33}S$ value (**a**) and database size (**b**) as a function of publication year. Filled symbols show the entire database with (circles) and without (triangles) the inclusion of sulphate minerals. Open symbols show the filtered database, with data obtained through secondary ion mass spectrometry (SIMS) analyses and data from macroscopic (often secondary) sulphide textures removed. Open symbols show the filtered database with (circles) and without (triangles) the inclusion of sulphate minerals.

***Model Setup*:**

Our model tracks the material transfer and isotopic composition of three Earth surface sulphur reservoirs (Figure 4.2): an oceanic sulphate reservoir (M_{sw}) and two crustal sulphur reservoirs [referred to, following (*16-19*, *74*) as "young" (M_y) and "old" (M_o)]. The distinction between two crustal reservoirs of varying cycling speeds was initially introduced to more directly couple the carbon and sulphur isotope composition of fluxes out of the ocean to that of input fluxes to the ocean, in an effort to alleviate physically unrealistic shifts in atmospheric composition due to changes in measured isotope ratios of sedimentary carbonate and sulphate minerals (*16*, *18*). However, there is also ample geological justification for such a model configuration (*16-19, 29, 74, 75*), and subsequent work has shown that this assumption results in a good agreement between proxy-based reconstructions of Phanerozoic atmospheric composition and those derived from mass balance models (*19, 22, 23, 76, 77*).

The dynamics of the seawater sulphate reservoir (M_{sw}) through time are governed by the input fluxes of sulphur associated with weathering of sulphides from both of the modeled crustal reservoirs ($F_{w,y}$ and $F_{w,o}$) and volcanic sulphur emissions (F_v), balanced against the removal of sulphur from the ocean in association with the burial of sedimentary pyrite ($F_{b,py}$). The mass of the rapidly weathering pyrite reservoir (M_y) is similarly controlled by the balance between inputs associated with pyrite burial ($F_{b,py}$) and outputs due to both weathering at the surface ($F_{\mathrm{w,y}}$) and gradual removal into the old sulphur reservoir (*16-19*, *74*) (F_{y-o}). The mass of the slowly weathering pyrite reservoir (M_o) is regulated by the balance between inputs from the young reservoir and outputs due to weathering. These relationships can be summarized as:

$$\frac{dM_{sw}}{dt} = F_{w,y} + F_{w,o} + F_v - F_{b,py} \ , \tag{4.2}$$

$$\frac{dM_y}{dt} = F_{b,py} - F_{w,y} - F_{y-o} \ , \tag{4.3}$$

$$\frac{dM_o}{dt} = F_{y-o} - F_{w,o} \ . \tag{4.4}$$

We assume that the deep ocean is Fe^{2+}-buffered (*78-82*). Conceptually, this means that hydrothermal sulphide introduced to the ocean through seawater-basalt interaction is negligible due to near vent iron sulphide precipitation, and is thus assumed not to participate in the isotope mass balance of oceanic sulphur.

Isotope mass balance equations can be similarly obtained for each reservoir:

$$\frac{d}{dt}(M_{sw}\delta_{sw}^{3x}) = F_{w,y}\delta_{y}^{3x} + F_{w,o}\delta_{o}^{3x} + F_{v}\delta_{v}^{3x} - F_{b,py}\delta_{py}^{3x} , \tag{4.5}$$

$$\frac{d}{dt}(M_{y}\delta_{y}^{3x}) = F_{b,py}\delta_{py}^{3x} - F_{w,y}\delta_{y}^{3x} - F_{y-o}\delta_{y}^{3x} , \tag{4.6}$$

$$\frac{d}{dt}(M_{o}\delta_{o}^{3x}) = F_{y-o}\delta_{y}^{3x} - F_{w,o}\delta_{o}^{3x} , \tag{4.7}$$

where "δ" values refer to the isotopic composition of each reservoir, defined according to traditional delta notation in "permil" (‰), and x = 3, 4, or 6. All flux terms, with the exception of the volcanic flux (F_v), which is imposed as a constant, are first-order and of the form:

$$F_i = k_i M_i , \tag{4.8}$$

where the subscripts "i" refer to a given flux, and "k_i" refers to the rate constant associated with each flux parameterization. The magnitude of a given flux thus depends largely on the size of the reservoir from which the flux is derived.

The equations for material and isotope mass balance can be combined and simplified to yield equations describing how the isotopic composition of a given reservoir evolves with time as a function of the fluxes into and out of the reservoir and their isotopic composition:

$$M_{sw}\frac{d\delta_{sw}^{3x}}{dt} = \sum_{i} F_i(\delta_{i}^{3x} - \delta_{sw}^{3x}) - F_{b,py}\Delta_{py}^{3x} , \tag{4.9}$$

$$M_{y}\frac{d\delta_{y}^{3x}}{dt} = F_{b,py}(\delta_{py}^{3x} - \delta_{y}^{3x}) , \tag{4.10}$$

$$M_{o}\frac{d\delta_{o}^{3x}}{dt} = F_{y-o}(\delta_{y}^{3x} - \delta_{o}^{3x}) . \tag{4.11}$$

where *i* in Eq. 8 refers to a given component of the overall input flux to the ocean. Note that the isotopic fractionation between seawater sulphate and sedimentary pyrite (Δ^{34}_{py}) is expressed as a negative number in the above equations. This parameter is defined, with reference to ^{34}S, using a Monod-type limiting function:

$$\Delta^{34}_{py} = \Delta^{34}_{MAX} \frac{[\mathrm{SO}_4^{2-}]_{sw}}{K_m^{\Delta} + [\mathrm{SO}_4^{2-}]_{sw}} \ , \tag{4.12}$$

where Δ^{34}_{MAX} refers to the maximum metabolic fractionation associated with microbial sulphate reduction, $[\mathrm{SO}_4^{2-}]_{sw}$ is the ambient seawater sulphate concentration (calculated from M_{sw} assuming an ocean volume of 1.37 x 10^{21} L), and K_m^{Δ} represents a "pseudo-half-saturation" constant derived empirically from chemostat experiments with *A. fulgidus* (*83*). Our reference model uses Δ^{34}_{MAX} = 30‰ and K_m^{Δ} = 0.363 mM, but these values have no effect on the magnitude of the Δ^{33}S signal through time and will only influence model trajectories in δ^{34}S – Δ^{33}S space. Microbial fractionations are related to the other isotopes assuming mass-dependence:

$$\Delta^{33}_{py} = {}^{33}\lambda * \Delta^{34}_{py} \tag{4.13}$$

$$\Delta^{36}_{py} = {}^{36}\lambda * \Delta^{34}_{py} \tag{4.14}$$

where $^{33}\lambda = 0.515$ and $^{36}\lambda = 1.890$ (e.g., *84*).

Model parameters for our reference case (Fig. 4.3) are shown in Table 4.S1. Parameter values for the reference case were chosen to approximately satisfy known constraints on: (1) the overall size of the crustal sulphur reservoir (*13, 16, 20, 85*); (2) the residence time of sulphur as it cycles through the exogenic system (*21, 29*); (3) the fraction of overall sulphur input derived from the rapidly recycling sulphur reservoir (*19, 26, 27, 86*); (4) the residence time of sulphur in the rapidly recycling reservoir with respect to weathering (*16, 17*); and, (5) the residence time of sulphur in the rapidly recycling reservoir with respect to removal to the old reservoir (the "aging flux" of the young pyrite reservoir; *16, 19, 87*). The range of F_v values was chosen to encompass estimates of the modern volcanic sulphur flux and values scaled up to reflect the possibility of greater crustal heat flow and volcanic activity during Earth's early history. Estimates of the modern volcanic sulphur flux are typically on the order of ~2-3 x 10^{11} mol y^{-1} (*88-92*), and we use an estimate of 2 x 10^{11} mol y^{-1} as our low volcanic flux. Heat flow through the crust has declined with time, and as a result it is typically assumed that Earth's early history was characterized by increased rates of volcanism. Estimates vary, but it is unlikely that crustal heat flow during the Archean was more than 3-4 times that of the modern Earth (*93-96*). Thus, we use a volcanic sulphur input of 1 x 10^{12} mol y^{-1} as our high volcanic flux. We note, however, that the mass flux from *subaerial* volcanic activity need not scale directly with rates of heat flow through the crust.

Table 4.S1. Model parameters and values used in our reference model. See text for details.

Parameter	Description	Reference Model Value
M_{sw}	seawater sulphate mass	2.74 x 10^{17} mol
M_y	mass of rapidly weathering (young) pyrite reservoir	5 x 10^{19} mol
M_o	mass of slowly weathering (old) pyrite reservoir	3 x 10^{20} mol
M_{tot}	Earth surface sulphur reservoir mass	3.5 x 10^{20} mol
k_y	young pyrite weathering rate constant	2 x 10^{-8} y^{-1}
k_o	old pyrite weathering rate constant	1 x 10^{-9} y^{-1}
k_{avg}	overall crustal sulphur weathering rate constant	3.7 x 10^{-9} y^{-1}
τ_{weath}	residence time of rapidly weathering pyrite reservoir with respect to weathering	50 x 10^6 y
$\tau_{y\text{-}o}$	residence time of rapidly weathering pyrite reservoir with respect to conversion to old reservoir (“aging flux”)	170 x 10^6 y
τ_{mean}	mean residence time of surface crustal sulphur	270 x 10^6 y
F_y / F_{tot}	fraction of overall weathering flux derived from rapidly weathering sulphur reservoir	0.77

References:

1. Farquhar J, Bao H, Thiemens M (2000) Atmospheric influence of Earth's earliest sulfur cycle. *Science* **289**, 756-758.

2. Farquhar J, Savarino J, Airieau S, Thiemens MH (2001) Observation of wavelength-sensitive mass-independent sulfur isotope effects during SO_2 photolysis: Implications for the early atmosphere. *Journal of Geophysical Research* **106**, 32829-32839.

3. Pavlov AA, Kasting JF (2002) Mass-independent fractionation of sulfur isotopes in Archean sediments: Strong evidence for an anoxic Archean atmosphere. *Astrobiology* **2**, 27-41.

4. Anbar AD, Duan Y, Lyons TW, Arnold GL, Kendall B, Creaser RA, Kaufman AJ, Gordon GW, Scott C, Garvin J, Buick R (2007) A whiff of oxygen before the Great Oxidation Event? *Science* **317**, 1903-1906.

5. Frei R, Gaucher C, Poulton SW, Canfield DE (2009) Fluctuations in Precambrian atmospheric oxygenation recorded by chromium isotopes. *Nature* **461**, 250-253.

6. Reinhard CT, Raiswell R, Scott C, Anbar AD, Lyons TW (2009) A late Archean sulfidic sea stimulated by early oxidative weathering of the continents. *Science* **326**, 713-716.

7. Bekker A, Holland HD, Wang P-L, Rumble D, Stein HJ, Hannah JL, Coetzee LL, Beukes NJ (2004) Dating the rise of atmospheric oxygen. *Nature* **427**, 117-120.

8. Zahnle K, Claire M, Catling D (2006) The loss of mass-independent fractionation of sulfur due to a Palaeoproterozoic collapse of atmospheric methane. *Geobiology* **4**, 271-283.

9. Halevy I, Johnston DT, Schrag DP (2010) Explaining the structure of the Archean mass-independent sulfur isotope record. *Science* **239**, 204-207.

10. Farquhar J, Wing BA, McKeegan KD, Harris JW, Cartigny P, Thiemens MH (2002) Inclusions in diamond and sulfur recycling on early Earth. *Science* **298**, 2369-2372.

11. Farquhar J, Wing BA (2003) Multiple sulfur isotopes and the evolution of the atmosphere. *Earth Planet. Sci. Lett.* **213**, 1-13.

12. Bekker A, Barley ME, Fiorentini ML, Rouxel OJ, Rumble D, Beresford SW (2009) Atmospheric sulfur in Archean komatiite-hosted nickel deposits. *Science* **326**, 1086-1089.

13. Canfield DE (2004) The evolution of the Earth surface sulfur reservoir. *American Journal of Science* **304**, 839-861.

14. Canfield DE, Farquhar J (2009) Animal evolution, bioturbation, and the sulfate concentration of the oceans. *Proceedings of the National Academy of Sciences USA* **106**, 8123-8127.

15. Habicht KS, Gade M, Thamdrup B, Berg P, Canfield DE (2002) Calibration of sulfate levels in the Archean ocean. *Science* **298**, 2372-2374.

16. Berner RA (1987) Models for carbon and sulfur cycles and atmospheric oxygen: Application to Paleozoic geologic history. *American Journal of Science* **287**, 177-196.

17. Berner RA, Canfield DE (1989) A new model for atmospheric oxygen over Phanerozoic time. *American Journal of Science* **289**, 333-361.

18. Berner RA (2001) Modeling atmospheric O_2 over Phanerozoic time. *Geochimica et Cosmochimica Acta* **65**, 685-694.

19. Berner RA (2006) GEOCARBSULF: A combined model for Phanerozoic atmospheric O_2 and CO_2. *Geochimica et Cosmochimica Acta* **70**, 5653-5664.

20. Garrels RM, Lerman A (1984) Coupling of the sedimentary sulfur and carbon cycles – An improved model. *American Journal of Science* **284**, 989-1007.

21. Kump LR, Garrels RM (1986) Modeling atmospheric O_2 in the global sedimentary redox cycle. *American Journal of Science* **286**, 337-360.

22. Royer DL, Berner RA, Beerling DJ (2001) Phanerozoic atmospheric CO_2 change: evaluating geochemical and paleobiological approaches. *Earth Science Reviews* **54**, 349-392.

23. Scott AC, Glasspool IJ (2006) The diversification of Paleozoic fire systems and fluctuations in atmospheric oxygen concentration. *Proceedings of the National Academy of Sciences USA* **103**, 10861-10865.

24. Farquhar J, Wing BA (2005) The terrestrial record of stable sulphur isotopes: a review of the implications for evolution of Earth's sulfur cycle. *GSA Special Publications* **248**, 167-177.

25. Ueno Y, Ono S, Rumble D, Maruyama S (2008) Quadruple sulfur isotope analysis of ca. 3.5 Ga Dresser Formation: New evidence for microbial sulfate reduction in the early Archean. *Geochimica et Cosmochimica Acta* **72**, 5675-5691.

26. Blatt H, Jones RL (1975) Proportions of exposed igneous, metamorphic, and sedimentary rocks. *GSA Bulletin* **86**, 1085-1088.

27. Bluth GJS, Kump LR (1991) Phanerozoic paleogeology. *American Journal of Science* **291**, 284-308.

28. Gregor CB (1985) The mass-age distribution of Phanerozoic sediments. *Memoirs of the Geological Society* **10**, 284-289.

29. Garrels RM, Mackenzie FT (1972) A quantitative model for the sedimentary rock cycle. *Marine Chemistry* **1**, 27-41.

30. Kaufman AJ, Johnston DT, Farquhar J, Masterson AL, Lyons TW, Bates S, Anbar AD, Arnold GL, Garvin J, Buick R (2007) Late Archean biospheric oxygenation and atmospheric evolution. *Science* **317**, 1900-1903.

31. Wille M, Kramers JD, Nägler TF, Beukes NJ, Schröder S, Meisel T, Lacassie JP, Voegelin AR (2007) Evidence for a gradual rise of oxygen between 2.6 and 2.5 Ga from Mo isotopes and Re-PGE signatures in shales. *Geochimica et Cosmochimica Acta* **71**, 2417-2435.

32. Garvin J, Buick R, Anbar AD, Arnold GL, Kaufman AJ (2009) Isotopic evidence for an aerobic nitrogen cycle in the lastest Archean. *Science* **323**, 1045-1048.

33. Duan Y, Anbar AD, Arnold GL, Lyons TW, Gordon GW, Kendall B (2010) Molybdenum isotope evidence for mild environmental oxygenation before the Great Oxidation Event. *Geochimica et Cosmochimica Acta* **74**, 6655-6668.

34. Canfield DE, Habicht KS, Thamdrup B (2000) The Archean sulfur cycle and the early history of atmospheric oxygen. *Science* **288**, 658-661.

35. Goldblatt C, Lenton TM, Watson AJ (2006) Bistability of atmospheric oxygen and the Great Oxidation. *Nature* **443**, 683-686.

36. Ono S, Beukes NJ, Rumble D, Fogel ML (2006) Early evolution of atmospheric oxygen from multiple-sulfur and carbon isotope records of the 2.9 Ga Mozaan Group of the Pongola Supergroup, Southern Africa. *South African Journal of Geology* **109**, 97-108.

37. Evans DA, Beukes NJ, Kirschvink JL (1997) Low-latitude glaciation in the Palaeoproterozoic era. *Nature* **386**, 262-266.

38. Maynard JB (2010) The chemistry of manganese ores through time: A signal of increasing diversity of Earth-surface environments. *Economic Geology* **105**, 535-552.

39. Hu G, Rumble D, Wang P-L (2003) An ultraviolet laser microprobe for the in situ analysis of multisulfur isotopes and its use in measuring Archean sulfur isotope mass-independent anomalies. *Geochimica et Cosmochimica Acta* **67**, 3101-3117.

40. Mojzsis SJ, Coath CD, Greenwood JP, McKeegan KD, Harrison TM (2003) Mass-independent isotope effects in Archean (2.5 to 3.8 Ga) sedimentary sulphides determined by ion microprobe analysis. *Geochimica et Cosmochimica Acta* **67**, 1635-1658.

41. Ono S, Eigenbrode JL, Pavlov AA, Kharecha P, Rumble III D, Kasting JF, Freeman KH (2003) New insights into Archean sulfur cycle from mass-independent sulfur isotope records from the Hamersley Basin, Australia. *Earth and Planetary Science Letters* **213**, 15-30.

42. Johnston DT, Wing BA, Farquhar J, Kaufman AJ, Strauss H, Lyons TW, Kah LC, Canfield DE (2005) Active microbial sulfur disproportionation in the Mesoproterozoic. *Science* **310**, 1477-1479.

43. Papineau D, Mojzsis SJ, Coath CD, Karhu JS, McKeegan KD (2005) Multiple sulfur isotopes of sulphides from sediments in the aftermath of Paleoproterozoic glaciations. *Geochimica et Cosmochimica Acta* **69**, 5033-5060.

44. Whitehouse MJ, Kamber BS, Fedo CM, Lepland A (2005) Integrated Pb- and S-isotope investigation of sulphide minerals from the early Archaean of southwest Greenland. *Chemical Geology* **222**, 112-131.

45. Cates NL, Mojzsis SJ (2006) Chemical and isotope evidence for widespread Eoarchean metasedimentary enclaves in southern West Greenland. *Geochimica et Cosmochimica Acta* **70**, 4229-4257.

46. Johnston DT, Poulton SW, Fralick PW, Wing BA, Canfield DE, Farquhar J (2006) Evolution of the oceanic sulfur cycle at the end of the Paleoproterozoic. *Geochimica et Cosmochimica Acta* **70**, 5723-5739.

47. Ohmoto H, Watanabe Y, Ikemi H, Poulson SR, Taylor BE (2006) Sulphur isotope evidence for an oxic Archaean atmosphere. *Nature* **442**, 908-911.

48. Ono S, Wing B, Johnston D, Farquhar J, Rumble D (2006) Mass-dependent fractionation of quadruple stable sulfur isotope system as a new tracer of sulfur biogeochemical cycles. *Geochimica et Cosmochimica Acta* **70**, 2238-2252.

49. Ono S, Wing B, Rumble D, Farquhar J (2006) High precision analysis of all four stable isotopes of sulfur (^{32}S, ^{33}S, ^{34}S and ^{36}S) at nanomole levels using a laser flourination isotope-ratio-monitoring gas chromatography-mass spectrometry. *Chemical Geology* **225**, 30-39.

50. Bao H, Rumble III D, Lowe DR (2007) The five stable isotope compositions of Fig Tree barites: Implications on sulfur cycle in ca. 3.2 Ga oceans. *Geochimica et Cosmochimica Acta* **71**, 4868-4879.

51. Farquhar J, Peters M, Johnston DT, Strauss H, Masterson A, Wiechert U, Kaufman AJ (2007) Isotopic evidence for Mesoarchaean anoxia and changing atmospheric sulphur chemistry. *Nature* **449**, 706-709.

52. Hou KJ, Li YH, Wan DF (2007) Constraints on the Archean atmospheric oxygen and sulfur cycle from mass-independent sulfur records from Anshan-Benxi BIFs, Liaoning Province, China. *Science in China Series D – Earth Sciences* **50**, 1471-1478.

53. Kamber BS, Whitehouse MJ (2007) Micro-scale sulphur isotope evidence for sulphur cycling in the late Archean shallow ocean. *Geobiology* **5**, 5-17.

54. Ono S, Shanks III WC, Rouxel OJ, Rumble D (2007) S-33 constraints on the seawater sulphate contribution in modern seafloor hydrothermal vent sulphides. *Geochimica et Cosmochimica Acta* **71**, 1170-1182.

55. Papineau D, Mojzsis SJ, Schmitt AK (2007) Multiple sulfur isotopes from Paleoproterozoic Huronian interglacial sediments and the rise of atmospheric oxygen. *Earth and Planetary Science Letters* **255**, 188-212.

56. Philippot P, Van Zuilen M, Lepot K, Thomazo C, Farquhar J, Van Kranendonk MJ (2007) Early Archaean microorganisms preferred elemental sulfur, not sulphate. *Science* **317**, 1534-1537.

57. Domagal-Goldman SD, Kasting JF, Johnston DT, Farquhar J (2008) Organic haze, glaciations and multiple sulfur isotopes in the Mid-Archean Era. *Earth and Planetary Science Letters* **269**, 29-40.

58. Johnston DT, Farquhar J, Summons RE, Shen Y, Kaufman AJ, Masterson AL, Canfield DE (2008) Sulfur isotope biogeochemistry of the Proterozoic McArthur Basin. *Geochimica et Cosmochimica Acta* **72**, 4278-4290.

59. Johnston DT, Farquhar J, Habicht KS, Canfield DE (2008)Sulphur isotopes and the search for life: strategies for identifying sulphur metabolisms in the rock record and beyond. *Geobiology* **6**, 425-435.

60. Partridge MA, Golding SD, Baublys KA, Young E (2008) Pyrite paragenesis and multiple sulfur isotope distribution in late Archean and early Paleoproterozoic Hamersley Basin sediments. *Earth and Planetary Science Letters* **272**, 41-49.

61. Ueno Y, Ono S, Rumble D, Maruyama S (2008) Quadruple sulfur isotope analysis of ca. 3.5 Ga Dresser Foromation: New evidence for microbial sulphate reduction in the early Archean. *Geochimica et Cosmochimica Acta* **72**, 5675-5691.

62. Guo Q, Strauss H, Kaufman AJ, Schröder S, Gutzmer J, Wing B, Baker MA, Bekker A, Jin Q, Kim S-T, Farquhar J (2009) Reconstructing Earth's surface oxidation across the Archean-Proterozoic transition. *Geology* **37**, 399-402.

63. Ono S, Beukes NJ, Rumble D (2009) Origin of two distinct multiple-sulfur isotope compositions of pyrite in the 2.5 Ga Klein Naute Formation, Griqualand West Basin, South Africa. *Precambrian Research* **169**, 48-57.

64. Ono S, Kaufman AJ, Farquhar J, Sumner DY, Beukes NJ (2009) Lithofacies control on multiple-sulfur isotope records and Neoarchean sulfur cycles. *Precambrian Research* **169**, 58-67.

65. Shen Y, Farquhar J, Masterson A, Kaufman AJ, Buick R (2009) Evaluating the role of microbial sulphate reduction in the early Archean using quadruple isotope systematics. *Earth and Planetary Science Letters* **279**, 383-391.

66. Thomazo C, Ader M, Farquhar J, Philippot P (2009) Methanotrophs regulated atmospheric sulfur isotope anomalies during the Mesoarchean (Tumbiana Formation, Western Australia). *Earth and Planetary Science Letters* **279**, 65-75.

67. Wu N, Farquhar J, Strauss H, Kim S-T, Canfield DE (2010) Evaluating the S-isotope fractionation associated with Phanerozoic pyrite burial. *Geochimica et Cosmochimica Acta* **74**, 2053-2071.

68. Zerkle AL, Claire MW, Domagal-Goldman SD, Farquhar J, Poulton SW (2012) A bistable organic-rich atmosphere on the Neoarchaean Earth. *Nature Geoscience* **5**, 359-363.

69. Guy BM, Ono S, Gutzmer J, Kaufman AJ, Lin Y, Fogel ML, Beukes NJ (2012) A multiple sulfur and organic carbon isotope record from non-conglomeratic sedimentary rocks of the Mesoarchean Witwatersrand Supergroup, South Africa. *Precambrian Research* **216-219**, 208-231.

70. Nelson DR, Trendall AF, Altermann W (1999) Chronological correlations between the Pilbara and Kaapvaal cratons. *Precambrian Research* **97**, 165-189.

71. Rasmussen B, Blake TS, Fletcher IR (2005) U-Pb zircon age constraints on the Hamersley spherule beds: Evidence for a single 2.63 Ga Jeerinah-Carawine impact ejecta layer. *Geology* **33**, 725-728.

72. Anbar AD, Duan Y, Lyons TW, Arnold GL, Kendall B, Creaser RA, Kaufman AJ, Gordon GW, Scott C, Garvin J, Buick R (2007) A whiff of oxygen before the Great Oxidation Event? *Science* **317**, 1903-1906.

73. Knoll AH, Beukes NJ (2009) Introduction: Initial investigations of a Neoarchean shelf margin-basin transition (Transvaal Supergroup, South Africa). *Precambrian Research* **169**, 1-14.

74. Berner RA (1989) Biogeochemical cycles of carbon and sulfur and their effect on atmospheric oxygen over Phanerozoic time. *Palaeogeography, Palaeoclimatology, Palaeoecology* **75**, 97-122.

75. Garrels RM, Mackenzie FT (1969) Sedimentary rock types: Relative proportions as a function of geological time. *Science* **163**, 570-571.

76. Royer DL, Berner RA, Park J (2007) Climate sensitivity constrained by CO_2 concentrations over the past 420 million years. *Nature* **446**, 530-532.

77. Berner RA, Kothavala Z (2001) GEOCARB III: A revised model of atmospheric CO_2 over Phanerozoic time. *American Journal of Science* **301**, 182-204.

78. Holland HD (1973) The oceans: A possible source of iron in iron-formations. *Economic Geology* **68**, 1169-1172.

79. Holland HD (1984) *The Chemical Evolution of the Atmosphere and Oceans*. Princeton University Press, Princeton, NJ.

80. Sumner DY (1997) Carbonate precipitation and oxygen stratification in late Archean seawater as deduced from facies and stratigraphy of the Gamohaan and Frisco formations, Transvaal Supergroup, South Africa. *American Journal of Science* **297**, 455-487.

81. Canfield DE (2005) The early history of atmospheric oxygen: Homage to Robert M. Garrels. *Annual Review of Earth and Planetary Sciences* **33**, 1-36.

82. Kump LR, Seyfried Jr. WE (2005) Hydrothermal Fe fluxes during the Precambrian: Effect of low oceanic sulphate concentrations and low hydrostatic pressure on the composition of black smokers. *Earth and Planetary Science Letters* **235**, 654-662.

83. Habicht KS, Salling L, Thamdrup B, Canfield DE (2005) Effect of low sulphate concentrations on lactate oxidation and isotope fractionation during sulphate reduction by *Archaeoglobus fulgidus* Strain Z. *Applied and Environmental Microbiology* **71**, 3770-3777.

84. Farquhar J, Johnston DT, Wing BA, Habicht KS, Canfield DE, Airieau S, Thiemens MH (2003) Multiple sulphur isotopic interpretations of biosynthetic pathways: implications for biological signatures in the sulphur isotope record. *Geobiology* **1**, 27-36.

85. Li Y-H (1972) Geochemical mass balance among lithosophere, hydrosphere, and atmosphere. *American Journal of Science* **272**, 119-137.

86. Garrels RM, Lerman A, Mackenzie FT (1976) Controls of atmospheric O_2 and CO_2: Past, present, and future. *American Scientist* **64**, 306-315.

87. Berner RA (1991) A model for atmospheric CO_2 over Phanerozoic time. *American Journal of Science* **291**, 339-376.

88. Berresheim H, Jaeschke W (1983) The contribution of volcanoes to the global atmospheric sulfur budget. *Journal of Geophysical Research* **88**, 3732-3740.

89. Walker JCG, Brimblecombe P (1985) Iron and sulfur in the pre-biologic ocean. *Precambrian Research* **28**, 205-222.

90. Andres RJ, Kasgnoc AD (1998) A time-averaged inventory of subaerial volcanic sulfur emissions. *Journal of Geophysical Research* **103**, 25251-25261.

91. Halmer MM, Schmincke H-U, Graf H-F (2002) The annual volcanic gas input into the atmosphere, in particular to the stratosphere: a global data set for the past 100 years. *Journal of Volcanology and Geothermal Research* **115**, 511-528.

92. Canfield DE, Rosing MT, Bjerrum C (2006) Early anaerobic metabolisms. *Philosophical Transactions of the Royal Society B* **361**, 1819-1836.

93. Schubert G, Stevenson D, Cassen P (1980) Whole planet cooling and the radiogenic heat source contents of the Earth and Moon. *Journal of Geophysical Research* **85**, 2531-2538.

94. Christensen, U.R. Thermal evolution models for the Earth. *J. Geophys. Res.* **90**, 2995-3007 (1985).

95. Lenardie A (2006) Continental growth and the Archean paradox. *Geophysocal Monograph Series* **164**, 33-45.

96. Padhi CM, Korenaga J, Ozima M (2012) Thermal evolution of Earth with xenon degassing: A self-consistent approach. *Earth and Planetary Science Letters* **341-344**, 1-9.

CHAPTER 5

A COUPLED MASS BALANCE APPROACH FOR RECONSTRUCTING OCEANIC REDOX LANDSCAPES: PROTEROZOIC CASE STUDY

Preface:

The contents of this chapter represent a manuscript in preparation for submission to the journal *Proceedings of the National Academy of Sciences USA*. This is reflected in the formatting.

Introduction:

The partial pressure of oxygen in Earth's atmosphere has increased dramatically through time. However, the trajectory and mechanisms controlling Earth's oxygenation are still poorly constrained, and even less is known regarding attendant changes in ocean ventilation and seafloor redox. We have a particularly poor understanding of ocean chemistry for a billion-year period during the mid-Proterozoic (from ~1.8 to 0.8 billion years ago), when the deep oceans are hypothesized to have been either oxic, anoxic and sulfidic (euxinic), or anoxic and Fe-rich (ferruginous). Given the coupling between redox-sensitive trace element cycles and planktonic ecosystem productivity, each of these models implies very different effects on the global biogeochemical cycling of major elements and trace nutrients, as well as potential ecological constraints on emerging eukaryotic life. Here, we exploit the differing redox behavior of molybdenum (Mo) and chromium (Cr) to provide new constraints on seafloor redox evolution by coupling a large database of sedimentary enrichments to a mass balance approach that includes a first-order description of spatially variant metal burial rates. We find that the Mo and Cr record necessitates a Proterozoic ocean that was pervasively anoxic relative to the Phanerozoic (at a minimum of ~40-50% of modern seafloor area and potentially much more) but was characterized by a relatively small extent of euxinic seafloor (less than ~1-10% of modern seafloor area). Our model also suggests that the oceanic Mo reservoir is extremely sensitive to very small perturbations in the extent of sulfidic seafloor and that the record of Mo and Cr enrichments through time is fully consistent with the possibility of a Mo co-limited marine biosphere during many periods of Earth's history, including the mid-Proterozoic.

Main Article:

The chemical composition of the oceans has changed dramatically with the oxidation of Earth's surface (*1*), and this process has profoundly influenced and been influenced by the evolutionary and ecological history of life (*2*). The early Earth was characterized by a reducing ocean-atmosphere system, while the Phanerozoic Eon (<0.542 billion years ago) is known for a stably oxygenated biosphere conducive to the radiation of large, metabolically demanding animal body plans and the development of complex ecosystems (*3*). The redox characteristics of surface environments during Earth's middle age (1.8 to 0.542 billion years ago [Ga]) are less well known. The ocean was historically envisaged to have become ventilated around 1.8 Ga, based on the disappearance of economic iron deposits (banded iron formations; *2*). However, over the past decade it has been commonly assumed that the mid-Proterozoic Earth was home to a globally euxinic ocean, a model derived from theory (*4*) and supported by evidence for at least local sulfidic conditions in Proterozoic marine systems (*5-8*).

More recently, it has been proposed that the deep ocean remained anoxic until the close of the Proterozoic, but that euxinia was limited to marginal settings with high organic matter loading (*9-12*). In anoxic settings with low dissolved sulfide levels, ferrous iron will accumulate—thus these anoxic but non-sulfidic settings have been termed 'ferruginous' (*9*). This model has also found support in at least local evidence for ferruginous marine conditions during the mid-Proterozoic (*11, 12*). However, it has been notoriously difficult to estimate the extent of this redox state on a global scale, even in the much more recent ocean—largely because most of the ancient deep seafloor has been subducted.

Independent of seafloor lost to subduction, trace metal enrichments in anoxic shales can record information about seafloor redox on a global scale. Following the establishment of pervasive oxidative weathering after the initial rise of atmospheric oxygen at ~2.4 Ga (*13*), the concentration of redox-sensitive elements in the ocean has been primarily controlled by marine redox conditions. For example, in today's well-oxygenated oceans, Mo is the most abundant transition metal in seawater (~107 nM; *14*), despite its very low crustal abundance (~1-2 ppm; *15*). Under sulfidic marine conditions the burial fluxes of Mo exceed those in oxygenated settings by several orders of magnitude (*16*). Hence, it follows that when sulfidic conditions are more widespread than today, global seawater concentrations of Mo will be much lower. Because the enrichment of Mo in sulfidic shales scales with dissolved seawater Mo concentrations (*17*), Mo enrichments in marine shales (independently elucidated as being deposited under euxinic conditions with a strong connection to the open ocean) can be used to track the global extent of sulfidic conditions (*18*). Substantial Mo enrichment in an ancient euxinic marine shale, such as occurs in modern euxinic marine sediments, implies that sulfidic bottom waters represent a very small extent of the global seafloor. In principle, a similar approach can be employed with other metals, such as Cr, which, importantly, will also be reduced and buried in sediments under anoxic conditions but without the requirement of free sulfide. In the case of Cr, it is readily immobilized as $(Fe,Cr)(OH)_3$ under ferruginous conditions (*19, 20*), and will be reduced and rendered insoluble by reaction with a wide range of other reductants under sulfidic or even denitrifying conditions (*21-24*). Thus, comparing Mo enrichments in independently constrained euxinic shales and Cr enrichments in independently constrained anoxic shales can offer a unique and complementary perspective on the global redox landscape of the ocean.

A better understanding of the marine Mo cycle in Proterozoic oceans may also illuminate key controlling factors in biological evolution and ecosystem development during the emergence of eukaryotic life. The biogeochemical cycles of marine trace elements form a crucial link between the inorganic chemistry of seawater and the biological modulation of atmospheric composition. The availability of iron, for example, has been invoked as a primary control on local carbon export fluxes and atmospheric $p\mathrm{CO}_2$ on glacial-interglacial timescales (*25, 26*). However, the leverage exerted by Fe on recent oceanic carbon fixation is most fundamentally driven by the sparing solubility of Fe in an ocean that is well-ventilated by an oxygen-rich atmosphere. By analogy, on a more reducing Earth surface Mo is likely to be a key co-limiting trace nutrient given its importance in biological nitrogen fixation, assimilatory/dissimilatory nitrate reduction, and a number of other metabolically significant electron transfer processes (*27-29*).

In order to move forward in our understanding of Proterozoic redox evolution, we present a novel view of Cr and Mo enrichments in anoxic shales and a complementary modeling approach to interpret these data. From this vantage, we present the first evidence that anoxic conditions must have been a globally important feature in the mid-Proterozoic ocean. In our analysis, we take anoxic environments to include those that are euxinic (anoxic and H_2S – rich), ferruginous (anoxic and Fe^{2+} – rich), and NO_3^- – buffered (i.e., anoxic but with low concentrations of both H_2S and Fe^{2+}). We note, however, that the latter environments are likely to be spatially and temporally limited, given the relatively low concentration (and thus redox buffering capacity) of NO_3^- in seawater.

In spite of evidence for pervasive marine anoxia, we highlight that euxinia covered only a small portion of the seafloor. On this basis, we present a new framework for linking Mo enrichments to seawater Mo concentrations, which points towards Mo co-limitation in the Proterozoic ocean. Therefore, despite a more limited extent of euxinia than previously envisaged, life in the Proterozoic ocean was heavily influenced by extents of sulfide in the water column that far exceeded the small amounts of euxinia that characterize the modern ocean.

The Mid-Proterozoic Geochemical Record

We present a new record of Cr and Mo enrichments in anoxic and euxinic shales through time (Fig. 5.1). Samples for this study (*n* > 3,000) come from our analytical efforts and a literature survey (Appendix B). Our own data include new results from over 300 Precambrian samples and modern anoxic systems. Samples were filtered for basic lithology (fine-grained siliciclastics) using a combination of basic sedimentary petrology and major-element thresholds. We relied on well-established paleoproxies rooted in Fe-S systematics to infer the redox state of the water column overlying the site of shale deposition. Importantly, these paleoredox proxies are calibrated to delineate anoxic settings (where Cr will be reduced and buried) and euxinic settings (where both Cr and Mo will be reduced/sulfidized and buried). The Fe-S paleo-proxies have recently been reviewed in detail (*30, 31*), and full information on sample filters is provided in the Supplementary Information. It is important to emphasize the non-circularity of our approach—specifically, we constrained paleoredox to have been anoxic or euxinic with no appeal to sedimentary metal enrichments as fingerprints of those conditions. This approach allows us to use the metal enrichments themselves as proxies for the *global* ocean redox state and its control on the ocean-wide inventories of those metals.

There are significant Mo enrichments in mid-Proterozoic euxinic shales (Fig. 5.1b). However, these enrichments are significantly lower than those observed in late Proterozoic (0.8 – 0.54 Ga) and Phanerozoic euxinic equivalents (*17*). Proterozoic enrichments range from less than 10 to greater than 100 ppm, compared to concentrations on the order of ~1-2 ppm in average upper crust (*15*). The total mean for temporally binned mid-Proterozoic shale data (2000-740 Ma) is 40.5 ppm (±22.5 at the 95% confidence level) compared to the Phanerozoic where the total mean is 170.2 ppm (±33.4 ppm at the 95% confidence level).

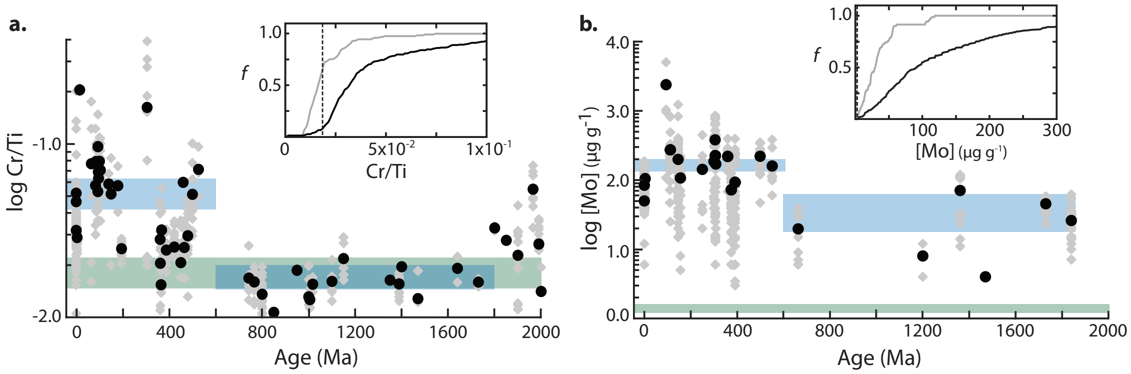

Figure 5.1. Sedimentary Cr **(a)** and Mo **(b)** enrichments in anoxic and euxinic black shales through time. Because of the relatively high Cr content of typical detrital material, Cr enrichments are expressed as Cr/Ti ratios. Grey diamonds represent all filtered data, while black circles represent temporally binned averages. Blue boxes show the total mean (±95% confidence interval) of temporally binned averages for the mid-Proterozoic and Phanerozoic (see SI Discussion). Insets show the cumulative frequency distribution of enrichments for the mid-Proterozoic (grey curve) and the Phanerozoic (black curve). Green boxes show the composition of average post-Archean upper crust (*31-33*), used to approximate the detrital input. Note the log-scale.

In strong contrast to the Mo record, there are no discernable Cr enrichments in mid-Proterozoic anoxic shales. We report Cr enrichments by normalizing to Ti content, as detrital inputs of Cr to marine sediments can be substantial and are greatly in excess of those for Mo. The total mean for Cr/Ti values for mid-Proterozoic anoxic shales is 1.69 x 10^{-2} (ppm/ppm), and the 95% confidence interval (1.45 x 10^{-2} – 1.93 x 10^{-2}) is indistinguishable from post-Archean average upper crust (*32-34*) (Fig. 5.1). There is a marked increase in Cr/Ti ratios after the late Proterozoic, with Phanerozoic shales showing Cr/Ti values indicating enrichments of 10s to 100s of ppm. This pattern is mirrored in the sharp rise in Mo enrichments through the same interval.

We hypothesize that the enrichment trends for both metals reflect the progressive expansion of marine anoxia between 2.0 and 1.8 Ga, followed by widespread anoxia and oceanic Cr drawdown during the mid-Proterozoic. Because of the different conditions required for the reduction, immobilization, and accumulation in sediments for Cr (anoxic) and Mo (euxinic), we suggest that a relatively small proportion of oceanic anoxia was represented by euxinic conditions, which allowed a moderate though muted seawater Mo reservoir to coexist with a strongly depleted Cr reservoir. In contrast, the Phanerozoic record is generally characterized by elevated enrichments of both elements, suggesting that for most of the Phanerozoic both anoxic and euxinic conditions were less spatially and/or temporally widespread. Comparatively short-lived Phanerozoic oceanic anoxic events, such as those famously expressed in the Mesozoic, are a notable exception. We suggest that combining enrichment records for elements that respond to the presence of free HS^- in anoxic marine environments (Mo, Zn, etc.) with elements that respond to anoxia more generally (Cr, Re, V, etc.) may allow us to place more rigorous constraints on the fabric of seafloor redox and bioinorganic feedbacks throughout Earth's history. We can expand this approach in a quantitative direction when the data are interpreted within a framework of the global mass balance.

Interpreting the Enrichment Record: A Model for Global Mass Balance and Burial in Marine Sediments

Our quantitative model begins with a conventional mass balance formulation (*35-37*), in which the ocean is treated as a single well-mixed reservoir (Fig. 5.2) — a reasonable assumption given the relatively long residence times of the elements of interest. The globally averaged concentration of a metal in the ocean evolves as:

$$\frac{d}{dt}\int_{v}[\mathrm{Me}]dv = F_{in} - F_{out} \text{ ,} \tag{5.1}$$

where [Me] represents the seawater concentration of a given metal (Mo or Cr for our purposes), integrated over ocean volume v. The terms F_{in} and F_{out} represent input and output fluxes, respectively. In both cases, input fluxes associated with riverine delivery and/or seawater-basalt interaction are grouped into a single input term (F_{in}; see Supplementary Information), while output fluxes (F_{out}) are broken into burial terms specific to each metal cycle (Fig. 5.2). Riverine input dominates the overall input flux for both metals, and this flux is not likely to have varied significantly (relative to variations in the removal fluxes) after Earth's initial oxygenation. Sink fluxes (burial in sediments) are a function of the characteristic burial rate and areal extent of a given sink environment (i):

$$F_{out}^{i} = k\int_{A_i} b_i^{ini} dA \text{ ,} \tag{5.2}$$

where A_i represents the seafloor area of each sink environment (oxic, ferruginous, euxinic, etc.), and b_i^{ini} represents the globally averaged initial burial rate characteristic of that environment. In this equation, k is a reaction coefficient that relates the burial flux to the seawater concentration. For a strictly first-order model, $k = [\mathrm{Me}]_t/[\mathrm{Me}]_\mathrm{M}$, where $[\mathrm{Me}]_t$ is the mean oceanic concentration of a given metal at time t, and $[\mathrm{Me}]_\mathrm{M}$ is the modern seawater concentration. As previously noted (*38*), this kind of first-order mass balance approach to specifying removal fluxes is a specific variant of the more generalized case:

$$F_{out}^{i} = k^{\alpha} \int_{A_i} b_i^{ini} dA \ , \tag{5.3}$$

where $\alpha = 1.0$.

Combining the above terms yields an expression for each removal flux:

$$F_{out}^{i} = A_i b_i^{ini} \{[\mathrm{Me}]_t / [\mathrm{Me}]_\mathrm{M}\}^{\alpha} \ . \tag{5.4}$$

Following previous approaches, we first assume that $\alpha = 1.0$ (i.e., a first-order mass balance relationship). This approach is grounded in the notion that the burial rate of a metal in a given sink environment will scale in a roughly linear fashion with the ambient seawater reservoir size (*17, 35-37*). After substitution and rearrangement of the above equations, and by specifying:

$$\gamma = \frac{\sum A_i b_i^{ini}}{[\mathrm{Me}]_\mathrm{M}} \ , \tag{5.5}$$

we arrive at a generalized mass balance equation for both metals:

$$\frac{d}{dt} \int_{v} [\mathrm{Me}] dv = F_{in} - \gamma [\mathrm{Me}]_t \ . \tag{5.6}$$

Because we are mainly interested in broad (~10^6 year) shifts in deep ocean redox, we assume steady-state conditions for both metal systems. Assuming steady state (i.e.,

$d[\mathrm{Me}]/dt = 0$) yields an expression for the average oceanic concentration of a given metal:

$$[\mathrm{Me}]_t = \frac{F_{in}}{\gamma} \ . \tag{5.7}$$

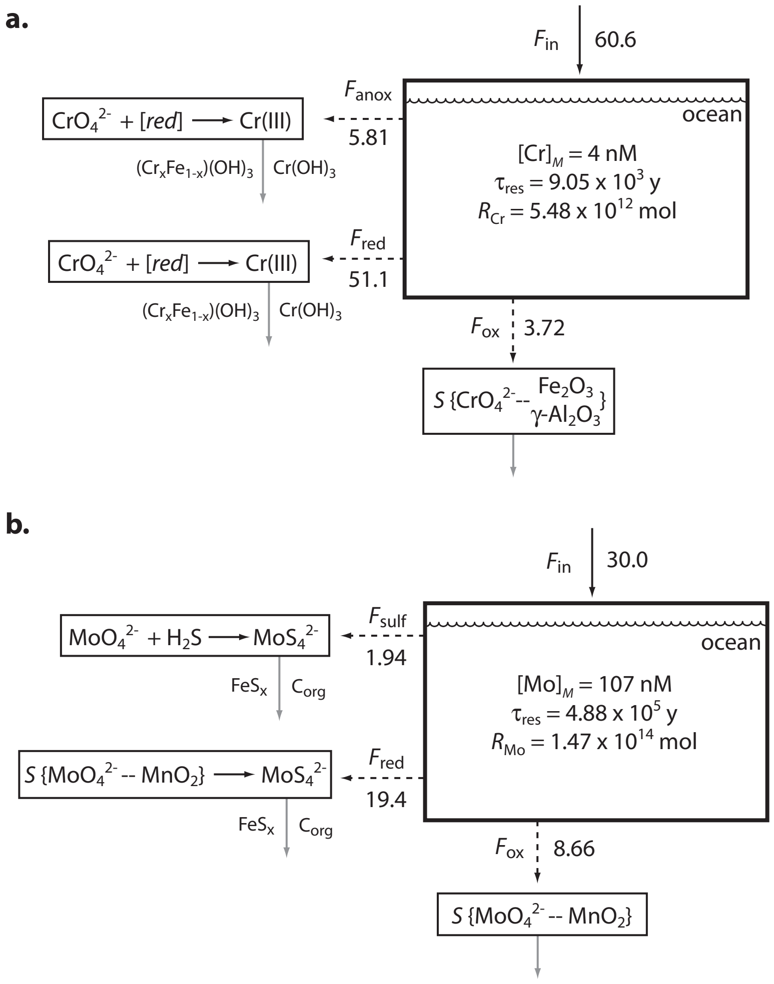

Figure 5.2. Schematic of the global Cr (**a**) and Mo (**b**) mass balance models, showing the modern balanced state. Dominant authigenic removal processes are depicted schematically for each sink. Terms with shown as $S\{x \text{ -- } y\}$ denote sorption processes. Hydrothermal fluxes are neglected in our treatment here (see Supplementary Information for further details). Fluxes are in 10^7 mol y^{-1}.

An important component of our model is the specification of spatially variant metal burial rates. Most past treatments of oceanic metal mass balance suffer from the physically unrealistic assumption that the metal burial rates characteristic of modern environments, typically encountered in restricted or marginal settings such as the Black Sea and Cariaco Basin where overall sediment and carbon fluxes are high, can be scaled to very large regions of the abyssal seafloor where bulk sediment delivery and TOC fluxes are typically much lower (*39-41*). We have attempted to avoid the same oversimplification by coupling an algorithm that addresses carbon flux to the seafloor as a function of depth (*42*) to a polynomial function fitted to bathymetric data (*43*), and by tuning an imposed burial ratio parameter ($\phi_{Me/C}$) to reproduce the modern globally averaged burial rate for each metal (see Supplementary Information).

The essential assumption here is that a given region of the seafloor will have a characteristic "burial capacity" for Mo and Cr, regulated to first-order by carbon flux to the sediment, and that this capacity will only be realized if the environment is anoxic (in the case of Cr) or euxinic (in the case of Mo). From a mechanistic perspective, this approach builds from clear evidence that the burial in sediments of many redox sensitive metals in anoxic settings scales strongly with carbon flux to the sediments (*17, 44-46*). We hold that this approach allows for a more realistic depiction of perturbations to seawater metal inventories as a function of seafloor redox dynamics by smoothly decreasing globally averaged burial rates as larger regions of the seafloor become anoxic (Cr) or euxinic (Mo).

Interpreting the Enrichment Record: Model Results

Our approach assumes, by definition, that the burial rate of a given metal in an authigenically active environment (i.e., environments that remove Cr and/or Mo from seawater and sequester them within the sediment column) scales with the ambient concentration in seawater:

$$b_i = b_i^{ini}\{[\mathrm{Me}]_t / [\mathrm{Me}]_\mathrm{M}\}^{\alpha} \tag{5.8}$$

The seawater reservoir is controlled largely by how this relationship is expressed on a global scale, but this relationship will also apply to individual settings or regions of the seafloor. As a result, we can envision a generalized authigenically active setting and estimate sedimentary metal enrichments as a function of seawater concentration, in turn controlled by the relative areas of different redox environments on a global scale.

The results of such an exercise are shown in Figure 5.3. Here, we have used as our starting point burial rates and overall sediment mass accumulation rates from one of the best characterized perennially euxinic basins on the modern Earth, the Cariaco Basin in Venezuela. Our purpose here is to depict a generalized setting accumulating Cr and Mo within sediments that has an open connection to the seawater metal reservoir(s), and for that reason we have chosen the Cariaco Basin over the highly restricted Black Sea, which shows clear local reservoir effects for Mo (*17*). In essence, we pose the question "how would an anoxic or euxinic continental margin environment, such as that represented in the marine black shale record, respond to a particular perturbation to seafloor redox state?" We can then scale this relationship to spatially varying C_{org} burial and bulk sedimentation to inform metal uptake away from the continental margin.

A striking pattern emerges when we consider the magnitude of enrichment that can be achieved in an authigenically active environment under different oceanic redox conditions (Fig. 5.3). If our model is correct, the negligible sedimentary Cr enrichments characteristic of the entire mid-Proterozoic would require extremely pervasive anoxic conditions. Our approach (which is likely conservative; see Supplementary Information) suggests that *at least* ~40-50% of the seafloor must have underlain anoxic deep waters in order to drive Cr enrichments to crustal values for sustained periods. We stress that this is a *minimum* estimate, and that our results are fully consistent with virtually complete seafloor anoxia.

The Mo enrichment record, however, tells a very different story. Enrichments in euxinic environments during this period are muted relative to the Phanerozoic, a pattern that emerges as a consequence of more widespread sulfidic deposition relative to most of the Phanerozoic and is reinforced when Mo enrichments are normalized to total organic carbon (*18*). However, Mo enrichments in Proterozoic euxinic environments that are mostly well above crustal values are inconsistent with pervasive, ocean-scale euxinia (Fig. 5.3). Instead, our model results point to roughly ~1-10% of the seafloor as being euxinic during the mid-Proterozoic, although there is likely to have been dynamic expansion/contraction of the area of euxinic seafloor area within and occasionally beyond this range—as related, for example, to spatiotemporal patterns of primary production along ocean margins. A similar range of euxinic seafloor is implied for some brief periods of the Phanerozoic (*47, 48*), but the record of appreciable Cr enrichment during this latter phase of Earth history indicates much more spatially and temporally restricted anoxia overall.

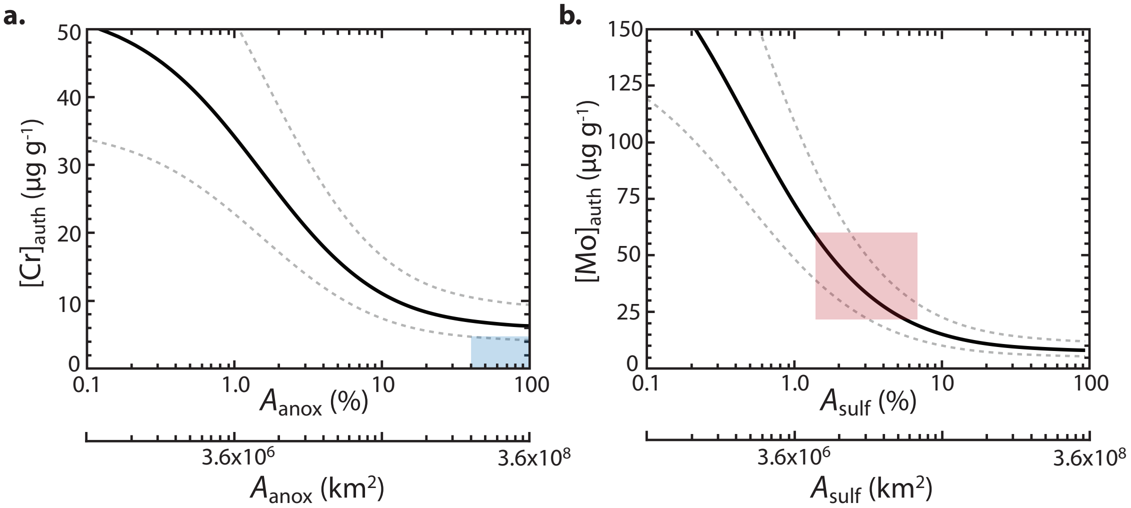

Figure 5.3. Estimated sedimentary enrichments for Cr (**a**) and Mo (**b**) in a generalized anoxic and/or euxinic setting, respectively. Black curves represent a bulk mass accumulation rate of 1.0 x 10^{-2} g cm^{-2} y^{-1}, while grey dotted curves represent a factor of 1.5 above and below this value. The blue box in (**a**) represents an enrichment threshold of 5 µg g^{-1}, a conservative value for our purposes given the negligible enrichments recorded by mid-Proterozoic anoxic shales. The red box in (**b**) shows the approximate euxinic seafloor area consistent with mid-Proterozoic Mo enrichments, and is scaled relative to the *y*-axis according to the 95% confidence interval of temporally binned averages shown in Fig. 5.1. Seafloor areas are shown as a percentage relative to modern seafloor area (%) and in terms of raw area (km^2).

A 'Biologically Sulfidic' Ocean

The record of Cr and Mo enrichment, when interpreted in light of our model results, necessitates that euxinia covered a relatively small fraction of overall seafloor area despite pervasive anoxic conditions on a global scale. Such a result adds to growing evidence that Proterozoic deep ocean chemistry was dominated by ferruginous conditions (*9, 11, 12*), in contrast to most modern anoxic marine settings that tend toward euxinia. Nevertheless, euxinia in the mid-Proterozoic ocean was likely orders of magnitude more widespread than today's estimate of ~0.1% of the seafloor, and the deleterious impacts on nutrient availability could have been enough to inhibit the early diversification of eukaryotic organisms. In effect, the sensitivity of the oceanic Mo reservoir to small perturbations in the extent of euxinia suggests that a distinction should be made between a *geochemically* sulfidic ocean, in which a large proportion of oceanic volume and basin- or global-scale areas of the seafloor (much more than our estimate of ~1-10%) are characterized by sulfidic waters, and a *biologically* sulfidic ocean, in which trace nutrient co-limitation of marine primary producers is strongly controlled by the extent of euxinic conditions.

To explore this possibility fully, we use the model to estimate globally averaged seawater [Mo] under variable scaling between the ambient seawater concentration and burial rate within sediments. The most common approach, as discussed above, is to assume strictly first-order (i.e., linear) scaling. Although data are somewhat limited and it is difficult to establish precisely what the form of this relationship should be, data from the most well-characterized perennially euxinic settings on the modern Earth suggest that this relationship may be non-linear (Fig. 5.4a). The effect of this parameter on steady-state globally averaged seawater [Mo] is shown in Figure 5.4b. Because lowering the value for α allows for a higher burial rate (and thus removal flux from the ocean) at a given value for seawater [Mo], the concentration is ultimately drawn down to much lower steady-state values for a given perturbation.

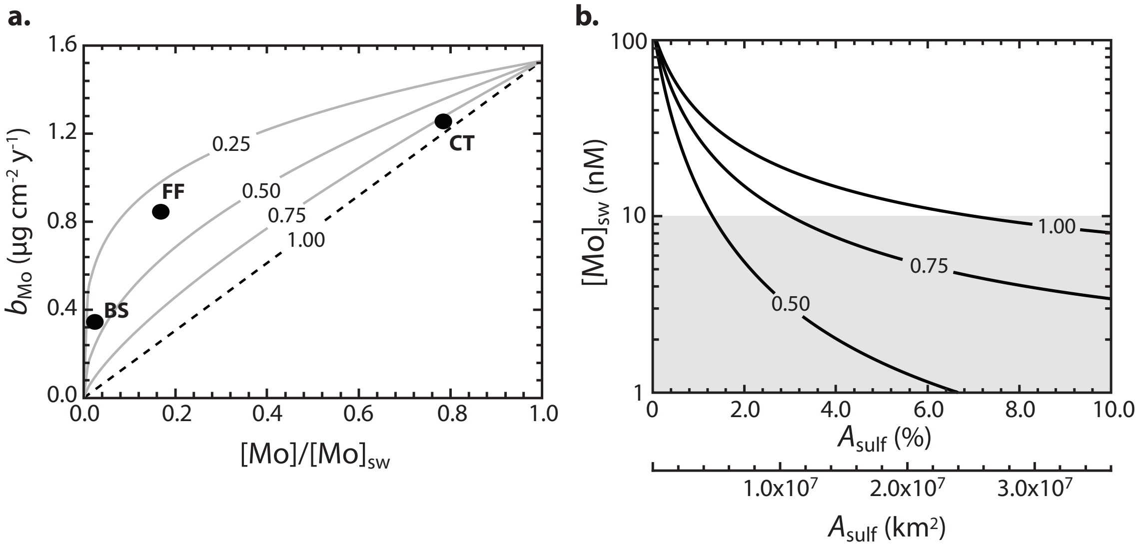

Figure 5.4. The effects of deviating from a strictly first-order model. Shown in (**a**) are Mo burial rates as a function of ambient dissolved Mo concentration (shown as a proportion of modern seawater, $[Mo]/[Mo]_{SW}$) for a range of α values between 1.0 (strict first-order) and 0.25. Curves are calculated assuming a modern globally averaged euxinic burial rate of 1.53 µg cm^{-2} y^{-1}. Black circles represent values for well-characterized perennially euxinic marine basins on the modern Earth [Black Sea (BS), Framvaren Fjord (FF) and the Cariaco Trench (CT); see Supplementary Information]. Shown in (**b**) are steady-state globally averaged seawater Mo concentrations as a function of euxinic seafloor area for different values of α. The shaded box depicts values below 10nM.

It is crucial to point out that although the term α regulates the scaling between ambient [Mo] and Mo burial rate on a global scale in an integrated sense across diverse redox settings, it will also do so within individual authigenically active environments. Importantly, this means that the sedimentary enrichments predicted by the model for a given extent of euxinic seafloor do not vary as a function of α. Changes in this parameter are reflected by the steady-state concentration of Mo in seawater (the same applies for Cr). It is clear from this exercise (Fig. 5.4) that even relatively small areas of the seafloor overlain by euxinic water masses (a fraction of modern continental shelf area) are sufficient to draw the ocean's average Mo concentration to ~10 nM (an order of magnitude below that seen in the modern ocean), even with strictly linear scaling between ambient [Mo] and burial flux.

Further work is needed to better pinpoint the levels of seawater Mo that should be considered biologically limiting, but available evidence is consistent with bio-limiting concentration in mid-Proterozoic oceans. Culturing experiments with modern strains of diazotrophic (nitrogen-fixing) organisms generally indicate that rates of nitrogen fixation and overall growth become impacted by Mo availability once concentrations fall to within the ~1-10 nM range (*49-53*). Some strains seem to show resilience to Mo scarcity until concentrations fall below ~5 nM (*52*), but in general there seems to be a sharp change in overall growth rates, cell-specific nitrogen fixation rates, and stoichiometric growth status within the 1-10 nM range. It is also important to point out that even small changes in relative rates of diazotrophy, if expressed globally and on protracted timescales, can be expected to have large effects on carbon and oxygen cycling.

Although Mo enrichments during the mid-Proterozoic do not approach those characteristic of comparable Phanerozoic settings, enrichment levels are nonetheless maintained well above crustal values. Thus, Mo enrichments in mid-Proterozoic euxinic marine settings seem poised within a very sensitive region of parameter space. We propose that such a relationship implies some kind of stabilizing feedback controlled by Mo co-limitation. In this scenario, widespread euxinic conditions would deplete the Mo reservoir, thereby limiting primary productivity and carbon export flux. This would reduce the amount of biomass oxidized via microbial sulfate reduction (which produces HS^-), limiting sulfide accumulation in marine settings. The ultimate result of this would be for Mo concentrations to rebound (a negative feedback; *18*). However, it would be difficult to transition from a Mo co-limited system to a more oxidizing, Mo replete ocean. Such a shift would need to be driven ultimately by a long-term increase in sedimentary burial of organic matter, but this would lead to a corresponding increase in Mo burial fluxes pushing the system back to Mo co-limitation. The link between primary production and Mo removal from the ocean would again be the microbial production of hydrogen sulfide needed for efficient Mo burial.

The response time of Mo in a Mo-depleted ocean should be short enough (relative to the residence time of oxygen in the ocean/atmosphere system) to induce a rapid and efficient stabilizing feedback on redox conditions. It is important to note that Fe will be orders of magnitude more soluble under any form of anoxia (euxinic or ferruginous) than it is in the modern ocean (*54*). In this light, in a reducing ocean, the coupled C-S-Fe-Mo biogeochemical cycles form an attractor—driving the marine system toward persistent trace metal-macronutrient co-limitation. This relationship is similar, in essence, to the control exerted by limited Fe solubility in an oxidizing and well-ventilated ocean, but we expect that the stabilizing feedbacks and sensitivity responses will be very different between the two systems.

Conclusions

Exploration of the Cr and Mo enrichment record in anoxic marine shales during the last ~2.0 Ga within a mass balance framework reveals that the mid-Proterozoic ocean was characterized by pervasive anoxic conditions, as manifested by negligible Cr enrichments in anoxic shales, but limited euxinia, as reflected in non-trivial Mo enrichments in euxinic shales that are nonetheless quite muted relative to most Phanerozoic equivalents. The Phanerozoic ocean appears to have been marked by more circumscribed anoxia on the whole, with anoxic shales typically showing substantial Cr enrichments. As a result, a potentially much larger *relative* fraction of this anoxia may have been represented by euxinic conditions, in particular during the Cretaceous oceanic anoxic events (OAEs) and periods of anomalously widespread anoxia during the Paleozoic (*48*). It remains to be explored if these episodes represent a fundamentally different mode of anoxic marine conditions or whether they can be viewed as temporary reversions to mid-Proterozoic conditions.

In addition, our model points toward a view in which the chemistry of small and dynamic regions of the seafloor exert fundamental control on biological carbon and oxygen cycling through bioinorganic feedbacks related to trace element availability (*18, 27*), in much the same way that carbon cycling and export in large regions of the modern well-ventilated ocean is controlled by the availability of Fe. Moving forward, it will be important to explore in detail, and with a wide range of organisms, the thresholds at which diazotrophs are strongly impacted by Mo availability. It will also be important to develop explicit ecological models aimed at delineating the constraints and feedbacks associated with Mo-N co-limited planktonic ecosystems. For example, elevated growth rates and doubling times due to greater overall Fe availability (as the solubility of Fe in any anoxic state will be orders of magnitude above that seen in oxic systems) may be able to compensate for lower cell-specific rates of nitrogen fixation within the context of ecosystem nitrogen supply. Further, little is known regarding the effects of Mo availability on assimilatory and/or dissimilatory nitrate reductase. Finally, it is clear that some diazotrophs show biochemical idiosyncrasies aimed at dealing with Mo scarcity (*53*), and recent work on the exquisite adaptation of some diazotrophic organisms to Fe limitation in the modern oceans (*55*) begs for a more thorough exploration of the biochemistry of Mo-limited diazotrophy.

In any case, our results provide strong independent evidence for an emerging first-order model of late Archean and Proterozoic ocean redox structure. In this model, the surface ocean is well-ventilated through air-sea gas exchange, but the deep ocean is anoxic as a result of initial equilibration of deep ocean water masses with atmospheric pO_2 at least 1-2 orders of magnitude below the modern value (*4*). The increased mobility and transport of dissolved Fe(II) under reducing conditions, combined with spatially heterogenous carbon fluxes through marine systems (as constrained by the intensity of vertical exchange through upwelling and eddy diffusion), yielded an ocean that was pervasively anoxic (i.e., redox-buffered by Fe^{2+} or NO_3^-) with localized regions of euxinia in marginal settings (*11, 12*). This emerging model provides a backdrop for the early evolution and ecological expansion of eukaryotic organisms (*26, 56*) and the biogeochemical feedbacks controlled by the progressive restructuring of primary producing communities (*57*). Finally, the sensitivity of the oceanic Mo reservoir to perturbation, combined with the existing Mo enrichment record in Proterozoic euxinic shales, implies that this redox structure may have been stable on long timescales as a function of Mo-co-limitation in the surface ocean. This hypothesis can be tested through the generation of more Proterozoic shale data, while further modeling might constrain how robust such a feedback could be and what conditions would have been required to surmount it during the later Proterozoic ventilation of the deep ocean and subsequent evolution of macroscopic life.

Supplementary Information:

Metal Enrichment Database and Filtering Protocols

Through our own analytical efforts and a literature survey, we have assembled a database of molybdenum (Mo) and chromium (Cr) concentrations for over 3,000 samples. Data sources are shown in Appendix B. Samples were initially filtered to represent solely fine-grained siliciclastic sediments, using basic petrographic observation and major element thresholds. Samples were required to contain weight percent (wt%) levels of iron (Fe) and aluminum (Al). Samples containing less than 1.0 wt% total organic carbon (TOC) were also removed.

The information contained within a particular degree of authigenic enrichment of Cr or Mo depends on local depositional redox. Thus, samples were further filtered such that Cr data was only analyzed from anoxic shales, and Mo data was only analyzed from euxinic shales. Anoxic shales were delineated as having $Fe_T/Al > 0.5$ (*58*) and/or $Fe_{HR}/Fe_T > 0.38$ (*7, 31, 59*), where Fe_{HR} designates "highly reactive" Fe (Fe that is reactive to dissolved H_2S on syngenetic or diagenetic timescales; *60*). Euxinic settings were delineated by combining the above thresholds for anoxia with either $Fe_{PY}/Fe_{HR} > 0.7$ (*7*, *61*), or with elevated values for degree of pyritization (DOP > 0.6; *30*), defined as (*62*):

$$\mathrm{DOP} = \frac{\mathrm{Fe}_{\mathrm{PY}}}{\mathrm{Fe}_{\mathrm{PY}} + \mathrm{Fe}_{\mathrm{HCl}}} \,, \tag{5.9}$$

where $\mathrm{Fe}_{\mathrm{HCl}}$ is Fe soluble in a 1-minute boiling concentrated HCl leach. Because elevated DOP has also been shown to require enhanced Fe mobility and transport (*30, 58*), and because it is an extremely robust analytical measurement, DOP > 0.8 supercedes all other redox filters in the designation of euxinia. In some cases, total sulfur content is used to calculate $\mathrm{DOP}_{\mathrm{T}}$, according to:

$$\mathrm{DOP}_{\mathrm{T}} = \frac{\mathrm{Fe}_{\mathrm{S}}}{\mathrm{Fe}_{\mathrm{S}} + \mathrm{Fe}_{\mathrm{T}}} \,, \tag{5.10}$$

where Fe_{S} denotes the inferred amount of sulfur-bound Fe assuming that total sulfur represents pyrite sulfur (*63*). Modern systems (such as the Black Sea and Cariaco Basin) were additionally filtered by site location, for extreme siliclastic dilution, and the presence of bioturbation.

Modern Molybdenum (Mo) Mass Balance

We begin by assuming steady state, wherein a single input flux (F_{in}) is balanced by removal via authigenic burial into three main sedimentary sinks: an oxic sink (F_{ox}), a reducing sediment sink (F_{red}), and a sulfidic sink (F_{sulf}). Our balanced modern Mo budget is shown in Table 5.S1, and individual removal terms are discussed below. The weathering flux of Mo on the modern Earth is dominated by the mobilization of Mo from sulfide mineral phases in sedimentary and igneous rocks and transport as dissolved $\mathrm{MoO_4}^{2-}$, and we set as F_{in} a recently obtained modern riverine flux of dissolved $\mathrm{MoO_4}^{2-}$ to the ocean (*64*). This flux is somewhat larger than those conventionally used, but is derived from the most extensive riverine database generated to date, representing 38 rivers across 5 continents and including 11 of 19 large-scale drainage areas. However, regardless of our choice of estimate for the riverine Mo flux, sensitivity analysis (Fig. 5.S1) indicates that our conclusions are weakly sensitive to the assumed value of the input flux over a wide range. We neglect hydrothermal fluxes of Mo to/from the ocean, as these are either poorly established or likely to be quantitatively small (see below).

Oxic settings are defined as those in which Mn is permanently removed from the ocean as an oxide phase (with associated adsorbed Mo). In many oxic deep sea settings, dissolved O_2 penetrates to the sediment-basalt interface (*65, 66*) and this Mn (and Mo) will effectively be buried permanently. In other settings, dissimilatory microbial Mn reduction deeper in the sediment column can remobilize Mn (and, presumably, associated Mo). However, when O_2 penetration depths are large (multiple cm or more) upward-diffusing Mn will be quantitatively oxidized at a steady state oxidation front (*67-69*), effectively removing Mn and Mo from the ocean on a timescale characteristic of tectonic recycling of seafloor sediments (on the order of ~10^8 years). Morford and Emerson (*37*) suggest that once O_2 penetration falls below ~1 cm, Mn and Mo will be recycled and released from shallow sediments. We therefore characterize oxic seafloor as being the areal extent of sediments in which O_2 penetration exceeds 1 cm. This is estimated using global diagenetic models (*70, 71*) to be ~3×10^8 km^2, or roughly 84% of modern seafloor area. We stress that there are fairly large regions of the seafloor that are essentially Mo neutral (see below), such that the total seafloor area for the entire budget need not sum to 100%. This area is then combined with a burial rate of 2.75×10^{-3} μg cm^{-2} y^{-1}, estimated by compiling Mo burial rates in oxic settings (*72*) and by combining Mn burial rates in oxic pelagic sediments (*73*) with a characteristic Mo/Mn ratio of 2 x 10^{-3} (*74*). The combined sink is shown in Table 5.S1.

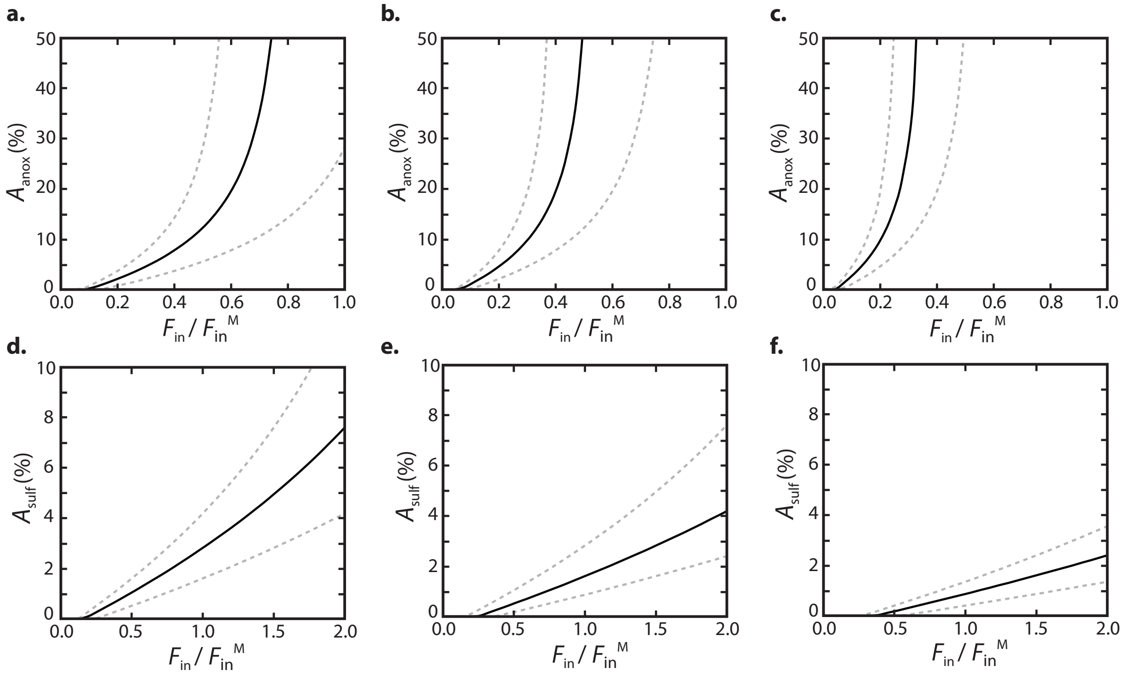

Figure 5.S1. The effect of changes in the assumed input flux on model results. Panels **a-c** apply to the Cr model. Each curve shows the areal extent of seafloor anoxia at which authigenic Cr enrichments decrease below 5 µg g^{-1}. Each panel represents a different bulk mass accumulation rate (increasing from left to right, with a range of a factor of 1.5 around 1.0 x 10^{-2} g cm^{-2} y^{-1}, the approximate value for deep sediments of the modern Cariaco Basin), while the curves represent low (dashed grey; 0.5 µg cm^{-2} y^{-1}), medium (black; 0.75 µg cm^{-2} y^{-1}) and high (dashed grey; 1.0 µg cm^{-2} y^{-1}) authigenic Cr burial rates. Panels **d-f** apply to the Mo model, with each curve showing the areal extent of sulfidic (euxinic) seafloor at which authigenic Cr enrichments decrease below 40 µg g^{-1} (the mid-Proterozoic total mean). The range of bulk MAR values is the same as in **a-c**, with the various curves in each panel representing low (dashed grey; 1.0 µg cm^{-2} y^{-1}), medium (black; 1.5 µg cm^{-2} y^{-1}) and high (dashed grey; 2.0 µg cm^{-2} y^{-1}) authigenic Mo burial rates.

Table 5.S1. Modern Mo budget.

Flux Term	Area	Area[a]	Burial Rate	F_i	F_i / F_{in}
-	km^2	%	µg cm^{-2} y^{-1}	mol y^{-1}	%
F_{in}	-	-	-	3.00 x 10^8	-
F_{ox}	3.02 x 10^8	83.89	2.75 x 10^{-3}	8.66 x 10^7	28.8
F_{red}	6.90 x 10^6	1.92	0.27	1.94 x 10^8	64.7
F_{sulf}	3.87 x 10^5	0.11	0.48[b]	1.94 x 10^7	6.5

[a]Assuming a global seafloor area of 3.6 x 10^8 km^2

[b]Note that although this is the correct value for use in balancing the modern budget, it is biased towards the Black Sea (see text).

Sulfidic settings are defined as environments in which dissolved H_2S accumulates at or above the sediment-water interface. This includes traditional euxinic settings (Black Sea, Cariaco Basin), but is also meant to include small areas of the seafloor below regions of intense upwelling (Peru margin, Namibian shelf), where dissolved H_2S is present at high levels essentially at the sediment-water interface and occasionally breaches into the water column (*75, 76*). Our sulfidic sink is calculated by combining estimates of seafloor area, authigenic enrichment, and bulk mass accumulation rate for modern sulfidic settings (*2*, *17, 46, 77-87*). The globally averaged sulfidic burial calculated through such an approach will be biased low – given that the modern extent of euxinic seafloor, on an areal basis, is dominated by the Black Sea, and this setting is characterized by low burial rates due to restricted exchange over the Bosporus sill and an evolved Mo reservoir (*17*). As a result, the global sulfidic burial rates implemented in the model are referenced to a modern globally averaged sulfidic burial rate that neglects the influence of the Black Sea. This is done in an effort to represent the burial capacity of marine settings with unfettered access to the seawater Mo reservoir (*18*).

The final sink is reducing sediments. This sink represents environments that have been referred to by the rather ambiguous term “suboxic”. We follow Scott et al. (*18*) in designating these environments as those in which dissolved H_2S accumulation is restricted to pore waters, but further point out that reducing sediments in which O_2 penetration is less than ~1 cm and H_2S accumulation occurs more deeply in the sediments do not effectively bury Mo (*37*). From a mechanistic perspective, these reducing sediment environments are typically associated with relatively low bottom water O_2, but the effectiveness of Mo sequestration in these settings is most likely a more complex function of Mn flux to sediments (and, thus, bottom water O_2), sedimentation rate, and labile organic carbon flux to the sediment-water interface. In any case, we use a somewhat moderate burial rate for reducing sediments of 0.27 $\mu g\ cm^{-2}\ y^{-1}$ (*84, 87, 88-90*), and use the remaining parameters of the budget to solve for the seafloor area represented by this sink (Table 5.S1). Although we present a revised approach for estimating this burial flux, our result is similar to previous estimates based on consideration of bulk burial rates (*18*) and isotope mass balance (*87*).

Modern chromium (Cr) mass balance

As for Mo, we begin by assuming steady state, with a single input flux (F_{in}) balanced by three authigenic burial fluxes: an oxic sink (F_{in}), a reducing sediment sink (F_{red}), and an anoxic sink (F_{anox}). In our modeling analysis, we take anoxic environments to include those that are euxinic (anoxic and H_2S – rich), ferruginous (anoxic and Fe^{2+} – rich), and NO_3^- – buffered (i.e., anoxic but with low concentrations of both H_2S and

Fe^{2+}). We note, however, that the latter environments are likely to be spatially and temporally limited, given the relatively low concentration (and thus redox buffering capacity) of NO_3^- in seawater. Potential hydrothermal fluxes to/from the ocean are neglected in our treatment of the modern Cr cycle, as currently available data suggest that these fluxes are quantitatively insignificant (see below). Our balanced modern Cr budget is presented in Table S3. The Cr mass balance is rather poorly constrained — compared to that for Mo. However, we suggest that although our mass balance is likely to be revised as better estimates of fluxes and reservoirs become available, this is very unlikely to change our fundamental conclusions.

Our input flux is calculated by combining an average dissolved riverine Cr concentration of 16 nM (*91*) with a global discharge rate of 3.7 x 10^4 km^3 y^{-1} (*92*). Combined with an average seawater concentration of 4 nM (*93*) and an ocean volume of 1.37 x 10^{21} L, this yields a residence time for Cr in the modern ocean of ~9,000 years (i.e., approximately a factor of 9 greater than the characteristic timescale of ocean mixing). To our knowledge, estimates of this sort are few, but ours is well in line previous attempts (e.g., *94*). As for Mo, sensitivity analysis (Fig. 5.S1) indicates that our conclusions are not likely to be fundamentally altered unless input fluxes to the ocean become extremely low.

Dissolved Cr(VI) species should become adsorbed onto the surface of metal- and Al-oxide phases (*95-97*). We therefore expect some non-trivial burial flux of Cr in oxic settings, although we note that sorption to Al-oxide phases decreases sharply when approaching circumneutral pH (*98*). The Cr content of pelagic red clays, although often elevated above crustal values with respect to Cr/Ti ratios, is rather variable. We use in our budget a relatively low oxic Cr burial rate of 1.0 x 10^{-3} µg cm^{-2} y^{-1}, of the same order as our much better constrained Mo burial flux. This corresponds to a sediment with a Cr/Ti ratio of 1.87 x 10^{-2}, consistent with typical values from pelagic red clays (*99-101*), accumulating at a burial rate of 1.0 x 10^{-3} g cm^{-2} y^{-1}. Because the burial of Cr in oxic settings should depend on the efficiency of metal oxide burial, this burial rate is then combined with the same areal extent of oxic seafloor (defined by sediment O_2 penetration depth) discussed above.

The anoxic sink for Cr is defined in a similar manner to the sulfidic sink for Mo, a natural result of the fact that on the modern Earth the relative mobility and transport of S and Fe are such that anoxic settings tend to become euxinic (anoxic and sulfidic). We use Cr/Ti ratios from the Cariaco Basin (*45, 81, 102, 103*) to obtain a modern anoxic burial rate of ~0.5 µg cm^{-2} y^{-1}, and scale this to the seafloor area of anoxic environments as discussed above for the modern Mo budget. This burial rate is roughly of the same order as that for Mo in euxinic settings, although we acknowledge that these estimates will improve with further generation and analysis of Cr data in anoxic marine systems. It is important to recognize, however, that Cr will be reduced and immobilized as Cr(III) via a wide range of reductants – dissolved H_2S is not necessary (*19, 20, 23*). Indeed, Cr(VI) reduction to Cr(III) has been shown to take place in the open water column of the eastern tropical Pacific, coincident with the onset of microbial denitrification (*24*). This provides a crucial distinction with the behavior of Mo, and forms the centerpiece of our analysis. The reducing sediment sink is again solved for using the other parameters of the budget.

We assume an authigenic burial rate of 0.15 μg cm^{-2} y^{-1}, derived from combining Cr/Ti ratios in the Gulf of California (*104*) with the requisite bulk mass accumulation rates (*105*). This aspect of the budget is not well constrained, but we consider it unlikely that such settings will authigenically bury Cr at rates much higher than this. In other words, we use what we consider to be a relatively high burial rate in order to avoid underestimating the magnitude of this sink relative to the anoxic sink. Parameters for our modern balanced Cr budget are shown in Table 5.S2.

Table 5.S2. Modern Cr budget.

Flux Term	Area	Area[a]	Burial Rate	F_i	F_i / F_{in}
-	km^2	%	μg cm^{-2} y^{-1}	mol y^{-1}	%
F_{in}	-	-	-	6.06 x 10^8	-
F_{ox}	3.02 x 10^8	83.89	1.00 x 10^{-3}	5.81 x 10^7	9.6
F_{red}	1.77 x 10^7	4.92	0.15	5.11 x 10^8	84.3
F_{anox}	3.87 x 10^5	0.11	0.50	1.94 x 10^7	6.1

[a] Assuming a global seafloor area of 3.6 x 10^8 km

Hydrothermal cycling of Mo and Cr

The systematics of Mo and Cr in hydrothermal systems and the effects of hydrothermal processes on the Earth surface cycles of Mo and Cr have note been explored in detail, but we can place some basic constraints on the possible effects of high- and low-temperature seawater-basalt interaction on the mass balances of Mo and Cr in the ocean. The water flux through a high-temperature hydrothermal system ($F_{(ht)}$; in kg y^{-1}) can be estimated as (*106*):

$$F_{(ht)} = \frac{Q_{(ht)}}{\Delta T_{(ht)} c_p} , \qquad (5.11)$$

where $Q_{(ht)}$ is the hydrothermal heat flux, $\Delta T_{(ht)}$ is the seawater temperature anomaly, and c_p is the specific heat of seawater (at seafloor pressure and vent fluid temperature). We can combine this with a concentration anomaly for a given metal ($\Delta[\mathrm{Me}] = [\mathrm{Me}]_{SW} - [\mathrm{Me}]_{fluid}$) to estimate a high temperature hydrothermal flux to/from seawater (F_{hyd}) as:

$$F_{hyd} = \frac{Q_{(ht)}}{\Delta T_{(ht)} c_p}([\mathrm{Me}]_{SW} - [\mathrm{Me}]_{fluid}) \ . \tag{5.12}$$

Results of this calculation for both Mo and Cr are shown in Table S4. These calculations suggest that high temperature seawater-basalt interaction represents a removal flux of both Mo and Cr that is quite small relative to the riverine flux of either element. We note that such estimates are inherently imprecise, given uncertainties in the magnitude of on-axis heat flow (*106* and references therein) and analytical difficulties associated with obtaining unadulterated fluid chemistry. In the case of high-temperature fluids, it is most likely that these concentrations have been perturbed by mixing with seawater Cr and/or Mo, which would cause us to underestimate the magnitude of these sink terms. However, this should have a negligible effect on our result, given that reported concentration anomalies indicate near complete removal of both elements during high-temperature seawater-basalt interaction (Table 5.S3). Assuming complete removal of seawater Mo from the circulating fluid (i.e., $\Delta[\mathrm{Mo}] = 107$ nM) would increase our estimated high-temperature removal flux from 0.85% to 0.91% of the total input flux. Making the same assumption for Cr (i.e., $\Delta[\mathrm{Cr}] = 4$ nM) would have a trivial effect on the estimated high-temperature removal flux.

Table 5.S3. Estimated high-temperature hydrothermal Mo and Cr fluxes.

	Mo		**Cr**	
$F_{(ht)}$[a]	Δ[Me][b]	F_{hyd} / F_{riv}	Δ[Me][c]	F_{hyd} / F_{riv}
kg y^{-1}	nM	%	nM	%
2.62 x 10^{13}	100	0.85	3.88	0.02

[a] Assuming: $Q_{(ht)}$ = 3.2 x 10^{12} W (*106*); $\Delta T_{(ht)}$ = 350ºC (*106*, *107*); c_p = 5.8 J g^{-1} K^{-1} (*106*)
[b] $[Mo]_{SW}$ from (*14*); $[Mo]_{fluid}$ from (*108*)
[c] $[Cr]_{SW}$ from (*93*); $[Cr]_{fluid}$ from (*109*)

Low-temperature, off-axis hydrothermal systems are a much more difficult problem to address. Pristine vent fluid composition is not well constrained for many settings, but, more importantly, the global water flux through such systems is very poorly constrained. Given that the temperature anomaly is probably small, a much larger water flux could be necessary to dissipate the requisite heat flow. As a result, even a very small concentration anomaly may result in a significant flux to/from seawater on a global scale. Magnesium (Mg^{2+}) substitutes readily for calcium (Ca^{2+}) during seafloor basalt alteration (*110*), and is removed from seawater during hydrothermal fluid evolution at both high- and low-temperature (*111-113*). Using the above method of calculation, the high-temperature removal flux of Mg^{2+} from seawater can be estimated as ~1.4 x 10^{12} mol y^{-1}. By combining the global discharge rate used above with a global average riverine Mg^{2+} concentration of 128 μmol kg^{-1} (*112*), we derive a global riverine Mg^{2+} flux of 4.7 x 10^{12} mol y^{-1}. If we assume that the balance between the riverine flux and removal during high-temperature seawater-basalt interaction is made up by low-temperature flow, we can use the Mg^{2+} concentration anomaly ($\Delta[Mg^{2+}] = [Mg^{2+}]_{SW} - [Mg^{2+}]_{fluid}$) to calculate an approximate water flux through low-temperature systems of 6.25 x 10^{13} kg y^{-1} .

Combining this estimated water flux with available chemical anomalies for Mo and Cr allows us to place rough limits on the magnitude of the low-temperature fluxes of these elements to seawater (Table 5.S4). These may be upper limits given available constraints, as the calculations assume no other removal fluxes of Mg^{2+} from seawater [i.e., uptake during carbonate burial or clay mineral alteration during "reverse weathering" reactions (*116*)]. We suggest that although low-temperature fluxes are likely to be somewhat larger than those that occur during on-axis fluid flow, they are still a relatively small fraction of the corresponding riverine fluxes. Given the framework outlined above, it is highly unlikely that the flux of either element will exceed ~10% of their respective riverine inputs. Furthermore, as stated above, sensitivity analysis indicates that our results are not strongly affected by reasonable changes in Cr and/or Mo input fluxes (Fig. 5.S1).

Table 5.S4. Estimated low-temperature hydrothermal Mo and Cr fluxes.

	Mo		**Cr**	
$F_{(1lt)}$[a]	Δ[Me][b]	F_{hyd} / F_{riv}	Δ[Me][c]	F_{hyd} / F_{riv}
kg y^{-1}	nM	%	nM	%
6.25×10^{13}	-190	4.07	-36	0.38

[a] Estimated assuming a Mg^{2+} removal flux of 1.4×10^{12} mol y^{-1} (see text)
[b] $[Mo]_{SW}$ from (*14*); $[Mo]_{fluid}$ from (*113*)
[c] $[Cr]_{SW}$ from (*93*); $[Cr]_{fluid}$ from (*115*)

Offshore scaling of metal burial rates in the model

Our modeling approach essentially involves balancing the modern steady state cycles of both Cr and Mo and applying a continuous range of perturbations to this balanced cycle to explore the new steady state attained under different oceanic redox regimes. In doing so, we begin with a conventional first-order mass balance formulation. This class of model, often employed to explore the dynamics of various chemical tracers in the ocean and their isotope systems, makes the implicit assumption that the burial fluxes characteristic of some particular environment (typically organic-rich continental margin sediments or marginal restricted basins) can be universally applied to extremely large regions of the seafloor. In other words, it is assumed that a burial rate characteristic of, say, the Peru margin can be applied to the abyssal realm of the ocean.

This is almost certainly physically unrealistic, as open ocean settings are characterized by much lower bulk sediment fluxes, and, in particular, organic carbon fluxes (*39, 40, 117, 118*). As a result, if a particular region of the abyssal ocean becomes authigenically active for some chemical constituent of seawater, it can be expected that the removal rates of that constituent into the sediment column will be much lower than those seen in more marginal settings. The net result will be a system that is overly sensitive to perturbation, as burial fluxes in large regions of the deep sea will be overestimated. This dilemma, inherent in conventional first-order mass balance analysis, has been noted by some previous work (*38, 119*) but has not been explored in detail. This problem is particularly acute for redox sensitive transition metals, like Mo and Cr, given that the organic matter flux is typically thought to be directly involved in metal sequestration (e.g., *17*).

We have attempted to alleviate this problem by adding a "pseudo-spatial" dimension to the conventional 1-box ocean mass balance approach. We take an algorithm employed in global diagenetic models (*42*) for organic carbon flux to the seafloor as a function of depth, which is then coupled to a polynomial function fitted to bathymetric data for the modern ocean (*43*). We then use a burial flux ratio ($\phi_{Me/C}$, where Me refers to Mo or Cr) for each element, a tuned parameter resulting in a relationship that encodes a decrease in local (and globally averaged) metal burial rates as larger regions of the seafloor become authigenically active. Values for $\phi_{Me/C}$ are tuned to reproduce the modern condition (i.e., the modern globally averaged burial rates at ~0.1% seafloor anoxia; Fig. 5.S2). The essential concept here is that a given region of the seafloor has a characteristic burial capacity for either Cr or Mo, regulated to first order by the relative carbon flux through the water column and to the sediments, and that this burial capacity will only be reached when a region of the ocean achieves the requisite redox characteristics for each metal.

We stress that because the metal burial rates are derived by using a tunable ratio, this pattern is not explicitly dependent on the *absolute value* of the carbon flux to the seafloor at a given depth – rather, it hinges on the observation that carbon fluxes to the seafloor will decrease as one moves out into the deep sea, with the first-order topology depicted in Figure 5.S2. This is important, as dramatically different redox structures within the ocean, extreme differences in the composition of primary producing communities, mineral ballasting, etc., might be expected to result in significant differences in the absolute value of the carbon flux to the seafloor within different regions of the ocean. However, we consider it unlikely that the basic pattern of an offshore decrease in carbon fluxes has changed much throughout Earth's history on a global scale. In addition, although the basic bathymetry of the ocean has doubtless changed throughout

Earth's history, we consider the modern depth-area curve to represent a reasonable first approximation.

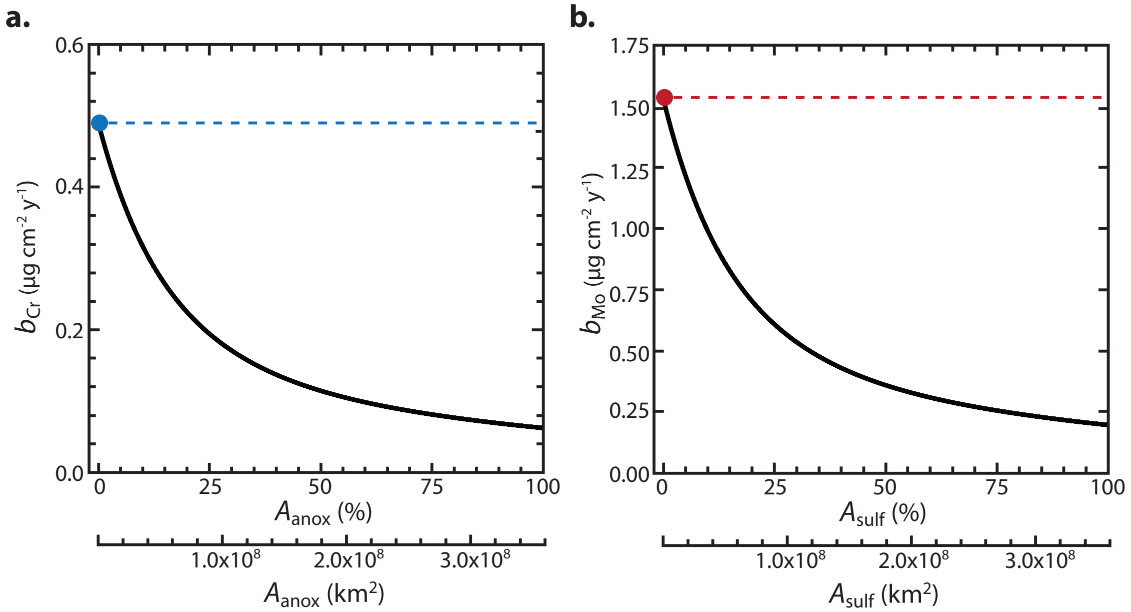

Figure 5.S2. Parameterization of offshore metal burial rate scaling in the model. Globally averaged authigenic Cr burial rates are shown in (**a**) as a function of anoxic seafloor area. The blue filled circle represents the modern state, with the blue dotted line depicting a constant burial rate decoupled from the extent of anoxic seafloor area. Globally averaged authigenic Mo burial rates are shown in (**b**) as a function of sulfidic (euxinic) seafloor area. The red filled circle represents the modern state, with the red dotted line depicting a constant burial rate decoupled from the extent of euxinic seafloor area (essentially the models employed in *18, 38, 119, 120*) .

This approach must ultimately be refined if used in efforts to delineate more subtle changes in ocean redox, or if applied to periods during which continental configuration and/or bathymetry are better constrained, but we contend that it provides a much more realistic depiction of the sensitivity of Cr and Mo mass balance to perturbation than previous model treatments. Further work should focus on the development and implementation of more spatially explicit approaches for dealing with the effects of seafloor redox perturbation on biogeochemical cycling and isotope systematics, for example coupling efficient models of benthic diagenesis that can be forced by gridded domains (*121*) to Earth system models of intermediate complexity (e.g., GENIE; *122*).

Prescribed perturbations in the model and the role of reducing sediments

As discussed above, our model analysis involves balancing the modern steady state cycles of Cr and Mo, applying a continuous range of perturbations to seafloor redox state, and establishing the ultimate steady state conditions and local burial rates attained by the model system. Because our model includes a representation of offshore decreases in authigenic burial rates, essentially a spatial component, we must make some explicit assumptions about the basic seafloor environments in which perturbations begin and expand.

We assume first that ~5% of the shallow seafloor remains essentially authigenically neutral unless it becomes absolutely necessary to encroach upon this area (i.e., above 95% seafloor anoxia or euxinia). This assumption is meant to encompass coastal sediments deposited within the well-oxygenated mixed layer of the ocean. Perturbations are then applied by expanding a given redox state (anoxic or euxinic) from the shallow shelf out into the deep sea. An important corollary of this approach is that during a given perturbation the first environments to become authigenically active are characterized by the highest metal burial rates. We view this as generally justifiable on mechanistic grounds, particularly in the case of expanding euxinia within the Mo model, as carbon fluxes through the water column and water column oxidant depletion are most commonly seen along ocean margins.

However, it is important to entertain the possibility that the nature of perturbations to seafloor redox may not be the same for Cr and Mo. For example, given that deep-sea anoxia during the mid-Proterozoic was most likely caused by gas exchange constraints expressed in deep water formation regions (*4*), rather than local reductant (i.e., carbon) input, it may be argued that large regions of the deep sea would first become anoxic and authigenically active for Cr while euxinic environments driven by the *combined effects* of more reducing source waters and local carbon flux would be limited to marginal environments. In effect, this would result in less efficient Cr removal and similar Mo removal compared to the results presented here, which would in turn require a larger area of marine anoxia for a given Cr reservoir change. Thus, in order to remain conservative we prescribe that perturbations to both models begin and expand from settings where metal accumulation rates are highest. The reverse scenario, in which euxinia develops first in the abyssal realm of the ocean but anoxia is confined to the shelves, is difficult to imagine simply because of regional variability in carbon flux.

Another important assumption that is made in our modeling exercise is that the seafloor area of reducing sediments is fixed at a constant value (~1.9% for the Mo model and ~4.9% for the Cr model). However, it is reasonable to expect that if the ocean becomes less oxygenated on a global scale there should be a first-order expansion of reducing sediment environments. With respect to our basic conclusions, it is clear that this is a much larger concern for Cr than for Mo. Expanding the reducing sediment sink in the Mo model would only serve to decrease the extent of euxinic seafloor inferred for a given calculated enrichment. In other words, our interpretation that the mid-Proterozoic

Mo enrichment record in euxinic shales implies relatively limited euxinic seafloor is rendered *conservative* by neglecting the expansion of reducing sediments in the model, and our conclusion that euxinia represents a small relative fraction of overall anoxia will remain unchanged.

In the case of Cr, it might be argued that expansion of the reducing sediment sink together with expanding anoxia could result in our model significantly over-estimating the amount of anoxic seafloor necessary to drive shifts in the seawater Cr reservoir. We consider this unlikely for two reasons. First, in our model experiments we have artificially enhanced the impact of the reducing sediment sink, by choosing a relatively high Cr burial rate and by specifying that this burial rate applies to ~5% of the seafloor *in addition* to the expansion of anoxia in shelf environments. When we consider that the offshore scaling of metal burial rates (Fig. S2) should equally well apply to reducing sediment environments, this essentially amounts to "double counting" ~5% of the seafloor as being both reducing sediments *and* anoxic, with the highest metal burial rates specified for both. Alternatively, we can envision this as representing the exclusive expansion of anoxia in marginal settings while ~5% of the seafloor offshore is covered by reducing sediments with unrealistically high burial rates. In either case, alternative approaches would need to either expand the reducing sediment sink at the expense of anoxic environments on the shelf, or expand it within the deep sea where metal burial capacity decreases sharply (Fig. 5.S2). Both approaches would yield a comparable (and in some cases smaller) overall removal flux into reducing sediment environments.

Lastly, it is unlikely for very large regions of the seafloor to be characterized by this type of chemical environment on long timescales. Environments on the modern Earth that fall into the reducing sediment category are generally marked by relatively low bottom water O_2 (often below analytical detection). It is difficult to imagine this kind of system persisting on an extremely large scale, as it is poorly redox-buffered – small changes to circulation or carbon flux will result in the development of either true anoxia or increased bottom water O_2 such that the environment becomes effectively oxic with respect to metal burial.

Using the model to calculate authigenic metal enrichments

From a qualitative perspective, it is difficult to avoid the conclusion that the coupled enrichment records require much more pervasive anoxia than that implied by equivalent Phanerozoic settings, but also that the relative fraction of anoxia represented by sulfidic deposition was not large. Our attempt to place more quantitative constraints on this conceptual interpretation involves using the scaling between seawater reservoir size and metal burial rates (inherent in a first-order mass balance model) to estimate sedimentary enrichments by assuming a bulk mass accumulation rate (MAR) in a hypothetical siliciclastic-dominated continental margin setting.

It is important to realize that these two parameters (authigenic metal burial rate and bulk sediment mass accumulation rate) *should not be arbitrarily decoupled*. This is true arithmetically, as metal burial rates in modern settings are in fact derived from bulk MARs. It is also expected on mechanistic grounds, as higher bulk MARs result in more rapid delivery of reactive mineral surfaces and organic carbon, and more rapid and efficient burial of authigenically sequestered elements. Indeed, there is good evidence from a range of modern (*123*) and ancient (*124*) settings that metal burial rates will scale in a general sense with bulk sediment MARs. This issue is similar to that discussed above, in that an arbitrary decoupling of metal burial rates from bulk MARs is akin to applying a metal burial rate from a continental margin setting to the abyssal realm of the ocean, an approach we consider physically unrealistic.

Because this scaling between metal burial rate and bulk MAR is a somewhat broad relationship, we use well-constrained recent Cariaco Basin sediment data as a guide. We separate the range of Cr and Mo burial rates and bulk MAR values constrained for the Cariaco Basin over the last ~20,000 years, and sequentially combine them to explore the effect of a slight decoupling between these two parameters (Fig. 5.S3). In an effort to render our estimates conservative, we choose combinations of metal burial rate and bulk MAR that result in relatively low enrichments for Cr and relatively high enrichments for Mo, and these are presented in the main text (Fig. 5.S3).

No single combination of parameters will be adequate to describe the entire shale record, but we view this broad range as sufficient to encompass the vast majority of environments represented in our database. It is apparent from this exercise that a very strong decoupling between metal burial rate and bulk MAR values, which we consider unrealistic, is necessary to invalidate our basic conclusions. Furthermore, this condition would need to pertain to every mid-Proterozoic anoxic shale in our database over ~1.5

billion years, while fortuitously being alleviated during the early Phanerozoic, a combination of circumstances that that would be improbable.

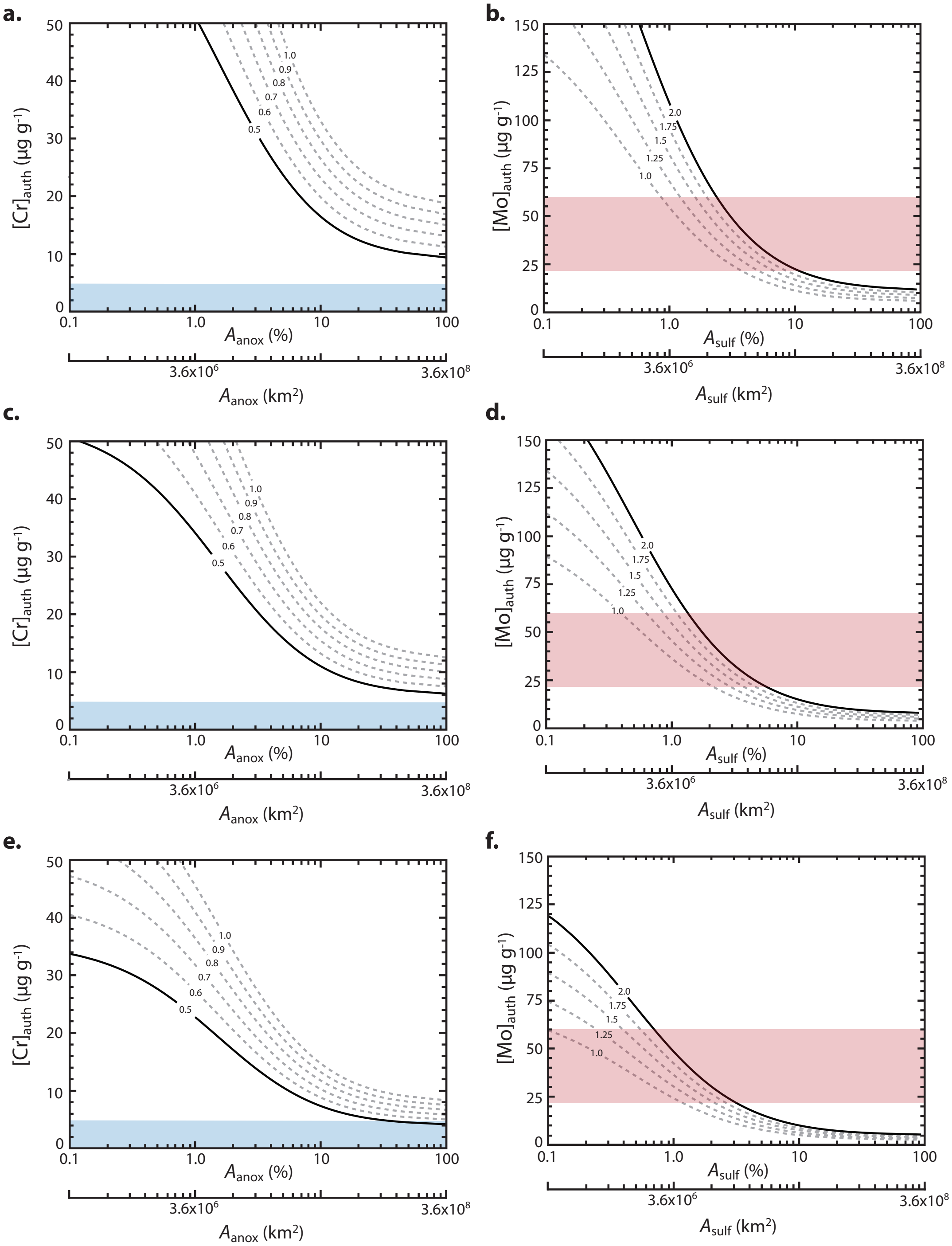

Figure 5.S3 (opposite). The range of metal burial rates and bulk sediment mass accumulation rates explored in the model. Panels **a**, **c**, and **e** depict estimated authigenic Cr enrichments as a function of anoxic seafloor area at a range of plausible metal burial rates and bulk sediment mass accumulation rates. The blue box represents our conservative threshold for Cr enrichment as constrained by the shale record. Panels **b**, **d**, and **f** depict estimated authigenic Mo enrichments as a function of sulfidic (euxinic) seafloor area at a range of plausible metal burial rates and bulk sediment mass accumulation rates. The red box represents the 95% confidence interval around the overall mean for the mid-Proterozoic shale enrichment record. Each panel represents a different bulk MAR (increasing from top to bottom, and depicting a range of a factor of 1.5 around 1.0 x 10^{-2} g cm^{-2} y^{-1}, the approximate value for deep sediments of the modern Cariaco Basin) and the contours are labeled by authigenic metal burial rate (in μg cm^{-2} y^{-1}). The solid black curves are those depicted in the main text.

References:

1. Holland HD (1984) *The Chemical Evolution of the Atmosphere and Oceans*. Princeton University Press, Princeton, NJ.

2. Cloud P (1972) A working model of the primitive Earth. *American Journal of Science* **272**, 537-548.

3. Payne JL, Boyer AG, Brown JH, Finnegan S, Kowalewski M, Krause Jr. RA, Lyons SK, McLain CR, McShea DW, Novack-Gottshall PM, Smith FA, Stempien JA, Wang SC (2009) Two-phase increase in the maximum size of life over 3.5 billion years reflects biological innovation and environmental opportunity. *Proceedings of the National Academy of Sciences USA* **106**, 24-27.

4. Canfield DE (1998) A new model for Proterozoic ocean chemistry. *Nature* **396**, 450-453.

5. Shen Y, Canfield DE, Knoll AH (2002) Middle Proterozoic ocean chemistry: Evidence from the McArthur Basin, Northern Australia. *American Journal of Science* **302**, 81-109.

6. Shen Y, Knoll AH, Walter, MR (2003) Evidence for low sulphate and anoxia in a mid-Proterozoic marine basin. *Nature* **423**, 632-635.

7. Poulton SW, Fralick PW, Canfield DE (2004) The transition to a sulphidic ocean ~1.84 billion years ago. *Nature* **431**, 173-177.

8. Brocks JJ, Love GD, Summons RE, Knoll AH, Logan GA, Bowden SA (2005) Biomarker evidence for green and purple sulphur bacteria in a stratified Palaeoproterozoic sea. *Nature* **437**, 866-870.

9. Canfield DE, Poulton SW, Knoll AH, Narbonne GM, Ross G, Goldberg T, Strauss H (2008) Ferruginous conditions dominated later Neoproterozoic deep-water chemistry. *Science* **321**, 949-952.

10. Lyons TW, Reinhard CT, Scott C (2009) Redox redux. *Geobiology* **7**, 489-494.

11. Poulton SW, Fralick PW, Canfield DE (2010) Spatial variability in oceanic redox structure 1.8 billion years ago. *Nature Geoscience* **3**, 486-490.

12. Planavsky NJ, McGoldrick P, Scott CT, Li C, Reinhard CT, Kelly AE, Chu X, Bekker A, Love GD, Lyons TW (2011) Widespread iron-rich conditions in the mid-Proterozoic ocean. *Nature* **477**, 448-451.

13. Bekker A, Holland HD, Wang P-L, Rumble III D, Stein HF, Hannah JL, Coetzee LL, Beukes NJ (2004) Dating the rise of atmospheric oxygen. *Nature* **427**, 117-120.

14. Collier RW (1985) Molybdenum in the Northeast Pacific Ocean. *Limnology & Oceanography* **30**, 1351-1354.

15. Taylor SR, McLennan SM (1995) The geochemical evolution of the continental crust. *Reviews of Geophysics* **33**, 241-265.

16. Emerson SR, Huested SS (1991) Ocean anoxia and the concentrations of molybdenum and vanadium in seawater. *Marine Chemistry* **34**, 177-196.

17. Algeo TJ, Lyons TW (2006) Mo-total organic carbon covariation in modern anoxic marine environments: Implications for analysis of paleoredox and paleohydrographic conditions. *Paleoceanography* **21**, doi:10.1029/2004PA001112.

18. Scott C, Lyons TW, Bekker A, Shen Y, Poulton SW, Chu X, Anbar AD (2008) Tracing the stepwise oxygenation of the Proterozoic ocean. *Nature* **452**, 456-459.

19. Eary LE, Rai D (1989) Kinetics of chromate reduction by ferrous ions derived from hematite and biotite at 25ºC. *American Journal of Science* **289**, 180-213.

20. Fendorf SE, Li G (1996) Kinetics of chromate reduction by ferrous iron. *Environmental Science & Technology* **30**, 1614-1617.

21. Pettine M, Millero FJ, Passino R (1994) Reduction of chromium (VI) with hydrogen sulfide in NaCl media. *Marine Chemistry* **46**, 335-344.

22. Graham AM, Bouwer EJ (2010) Rates of hexavalent chromium reduction in anoxic estuarine sediments: pH effects and the role of acid volatile sulfides. *Environmental Science & Technology* **44**, 136-142.

23. Bond DL, Fendorf S (2003) Kinetics and structural constraints of chromate reduction by green rusts. *Environmental Science & Technology* **37**, 2750-2757.

24. Rue EL, Smith GJ, Cutter GA, Bruland KW (1997) The response of trace element redox couples to suboxic conditions in the water column. *Deep-Sea Research I* **44**, 113-134.

25. Martin JH (1990) Glacial-interglacial CO_2 change: The iron hypothesis. *Paleoceanography* **5**, 1-13.

26. Behrenfeld MJ, Kolber ZS (1999) Widespread iron limitation of phytoplankton in the South Pacific Ocean. *Science* **283**, 840-843.

27. Anbar AD, Knoll AH (2002) Proterozoic ocean chemistry and evolution: A bioinorganic bridge? *Science* **297**, 1137-1142.

28. Schwarz G, Mendel RR, Ribbe MW (2009) Molybdenum cofactors, enzymes and pathways. *Nature* **460**, 839-847.

29. Glass JB, Wolfe-Simon F, Anbar AD (2009) Coevolution of metal availability and nitrogen assimilation in cyanobacteria and algae. *Geobiology* **7**, 100-123.

30. Lyons TW, et al. (2009) Tracking euxinia in the ancient ocean: A multiproxy perspective and Proterozoic case study. *Annual Review of Earth and Planetary Sciences* **37**, 507-534.

31. Poulton SW, Canfield DE (2011) Ferruginous conditions: A dominant feature of the ocean through Earth's history. *Elements* **7**, 107-112.

32. Condie KC (1993) Chemical composition and evolution of the upper continental crust: Constrasting results from surface samples and shales. *Chemical Geology* **104**, 1-37.

33. McLennan SM (2001) Relationships between the trace element composition of sedimentary rocks and upper continental crust. *Geochemistry, Geophysics, Geosystems* **2**, doi:2000GC000109.

34. Rudnick RL, Gao S (2003) Composition of the Continental Crust. *In* Holland HD, Turekian KK (*eds*.), *Treatise on Geochemistry* **3**, 1-64.

35. Rosenthal Y, Boyle EA, Labeyrie L, Oppo D (1995) Glacial enrichments of authigenic Cd and U in Subantarctic sediments: A climate control on the elements' oceanic budget? *Paleoceanography* **10**, 395-413.

36. Hastings DW, Emerson SR, Mix AC (1996) Vanadium in foraminiferal calcite as a tracer for changes in the areal extent of reducing sediments. *Paleoceanography* **11**, 665-678.

37. Morford JL, Emerson S (1999) The geochemistry of redox sensitive trace metals in sediments. *Geochimica et Cosmochimica Acta* **63**, 1735-1750.

38. Dahl TW, Canfield DE, Rosing MT, Frei RE, Gordon GW, Knoll AH, Anbar AD (2011) Molybdenum evidence for expansive sulfidic water masses in ~750 Ma oceans. *Earth ad Planetary Science Letters* **311**, 264-274.

39. Jahnke RA (1996) The global ocean flux of particulate organic carbon: Areal distribution and magnitude. *Global Biogeochemical Cycles* **10**, 71-88.

40. Middelburg JJ, Soetaert K, Herman PMJ (1997) Empirical relationships for use in global diagenetic models. *Deep-Sea Research I* **44**, 327-344.

41. Dunne JP, Sarmiento JL, Gnanadesikan A (2007) A synthesis of global particle export from the surface ocean and cycling through the ocean interior and on the seafloor. *Global Biogeochemical Cycles* **21**, doi:10.1029/2006GB002907.

42. Middelburg JJ, Soetaert K, Herman PMJ, Heip CHR (1996) Denitrification in marine sediments: A model study. *Global Biogeochemical Cycles* **10**, 661-673.

43. Menard HW, Smith SM (1966) Hypsometry of ocean basin provinces. *Journal of Geophysical Research* **71**, 4305-4325.

44. Algeo TJ, Maynard JB (2004) Trace-element behavior and redox facies in core shales of Upper Pennsylvanian Kansas-type cyclothems. *Chemical Geology* **206**, 289-318.

45. Dean WE (2007) Sediment geochemical records of productivity and oxygen depletion along the margin of western North America during the past 60,000 years: teleconnections with Greenland Ice and the Cariaco Basin. *Quaternary Science Reviews* **26**, 98-114.

46. Lyons TW, Werne JP, Hollander DJ, Murray RW (2003) Contrasting sulfur geochemistry and Fe/Al and Mo/Al ratios across the last oxic-to-anoxic transition in the Cariaco Basin, Venezuela. *Chemical Geology* **195**, 131-157.

47. Pearce CR, Cohen AS, Coe AL, Burton KW (2008) Molybdenum isotope evidence for global ocean anoxia coupled with perturbations to the carbon cycle during the Early Jurassic. *Geology* **36**, 231-234.

48. Gill BC, Lyons TW, Young SA, Kump LR, Knoll AH, Saltzman MR (2011) Geochemical evidence for widespread euxinia in the Later Cambrian ocean. *Nature* **469**, 80-83.

49. Fay P, de Vasconcelos, L (1974) Nitrogen metabolism and ultrastructure in *Anabaena cylindrica. Archives of Microbiology* **99**, 221-230.

50. Jacobs R, Lind O (1977) The combined relationship of temperature and molybdenum concentration to nitrogen fixation by *Anabaena Cylindrica*. *Microbial Ecology* **3**, 205-217.

51. Zahalak M, Pratte B, Werth KJ, Thiel T (2004) Molybdate transport and its effect on nitrogen utilization in the cyanobacterium *Anabaena variabilis* ATCC 29413. *Molecular Microbiology* **51**, 539-549.

52. Zerkle AL, House CH, Cox RP, Canfield DE (2006) Metal limitation of cyanobacterial N_2 fixation and implications for the Precambrian nitrogen cycle. *Geobiology* **4**, 285-297.

53. Glass JB, Wolfe-Simon F, Elser JJ, Anbar AD (2010) Molybdenum-nitrogen co-limitation in freshwater and coastal heterocystous cyanobacteria. *Limnology & Oceanography* **55**, 667-676.

54. Spencer DW, Brewer PG (1971) Vertical advection diffusion and redox potentials as controls on the distribution of manganese and other trace metals dissolved in waters of the Black Sea. *Journal of Geophysical Research* **76**, 5877-5892.

55. Saito MA, Bertrand EM, Dutkiewicz S, Bulygin VV, Moran DM, Monteiro FM, Follows MJ, Valois FW, Waterbury JB (2011) Iron conservation by reduction of metalloenzyme inventories in the marine diazotroph *Crocosphaera watsonii*. *Proceedings of the National Academy of Sciences USA* **108**, 2184-2189.

56. Javaux EJ, Knoll AH, Walter MR (2004) Morphological and ecological complexity in early eukaryotic ecosystems. *Nature* **412**, 66-69.

57. Johnston DT, Wolfe-Simon F, Pearson A, Knoll AH (2009) Anoxygenic photosynthesis modulated Proterozoic oxygen and sustained Earth's middle age. *Proceedings of the National Academy of Sciences USA* **106**, 16925-16929.

58. Lyons TW, Severmann S (2006) A critical look at iron paleoredox proxies: New insights from modern euxinic marine basins. *Geochimica et Cosmochimica Acta* **70**, 5698-5722.

59. Poulton SW, Canfield DE (2005) Development of a sequential extraction procedure for iron: implications for iron partitioning in continentally derived particulates. *Chemical Geology* **214**, 209-221.

60. Canfield DE (1989) Reactive iron in marine sediments. *Geochimica et Cosmochimica Acta* **53**, 619-632.

61. März C, Poulton SW, Beckmann B, Küster K, Wagner T, Kasten S (2008) Redox sensitivity of P cycling during marine black shale formation: Dynamics of sulfidic and anoxic, non-sulfidic bottom waters. *Geochimica et Cosmochimica Acta* **72**, 3703-3717.

62. Raiswell R, Buckley R, Berner RA, Anderson TF (1988) Degree of pyritization of iron as a paleoenvironmental indicator of bottom-water oxygenation. *Journal of Sedimentary Petrology* **58**, 812-819.

63. Algeo TJ, Maynard JB (2008) Trace-metal covariation as a guide to water-mass conditions in ancient anoxic marine environments. *Geosphere* **4**, 872-887.

64. Miller CA, Peucker-Ehrenbrink B, Walker BD, Marcantonio F (2011) Re-assessing the surface cycling of molybdenum and rhenium. *Geochimica et Cosmochimica Acta* **75**, 7146-7179.

65. D'Hondt S, Spivack AJ, Pockalny R, Ferdelman TG, Fischer JP, Kallmeyer J, Abrams LF, Smith DC, Graham D, Hasiuk F, Schrum H, Stancin AM (2009) Subseafloor sedimentary life in the South Pacific Gyre. *Proceedings of the National Academy of Sciences USA* **106**, 11651-11656.

66. Fischer JP, Ferdelman TG, D'Hondt S, Røy H, Wenzhöfer F (2009) Oxygen penetration deep into the sediment of the South Pacific gyre. *Biogeosciences* **6**, 1467-1478.

67. Froelich PN, Klinkhammer GP, Bender ML, Luedtke NA, Heath GR, Cullen D, Dauphin P, Hammond D, Hartman B, Maynard V (1979) Early oxidation of organic matter in pelagic sediments of the eastern equatorial Atlantic: suboxic diagenesis. *Geochimica et Cosmochimica Acta* **43**, 1075-1090.

68. Finney BP, Lyle MW, Heath GR (1988) Sedimentation at MANOP Site H (Eastern Equatorial Pacific) over the past 400,000 years: Climatically induced redox variations and their effects on transition metal cycling. *Paleoceanography* **3**, 169-189.

69. Burdige DJ (1993) The biogeochemistry of manganese and iron reduction in marine sediments. *Earth-Science Reviews* **35**, 249-284.

37. Morford JL, Emerson S (1999) The geochemistry of redox sensitive trace metals in sediments. *Geochimica et Cosmochimica Acta* **63**, 1735-1750.

70. Meile C, Van Cappellen P (2003) Global estimates of enhanced solute transport in marine sediments. *Limnology & Oceangraphy* **48**, 777-786.

71. Thullner M, Dale AW, Regnier P (2009) Global-scale quantification of mineralization pathways in marine sediments: A reaction-transport modeling approach. *Geochemistry, Geophysics, Geosystems* **10**, doi:10.1029/2009GC002484.

72. Bertine KK, Turekian KK (1973) Molybdenum in marine deposits. *Geochimica et Cosmochimica Acta* **37**, 1415-1434.

73. Bender ML, Ku T-L, Broecker WS (1970) Accumulation rates of manganese in pelagic sediments and nodules. *Earth and Planetary Science Letters* **8**, 143-148.

74. Shimmield GB, Price NB (1986) The behaviour of molybdenum and manganese during early sediment diagenesis – offshore Baja California, Mexico. *Marine Chemistry* **19**, 261-280.

75. Brüchert V, et al. (2003) Regulation of bacterial sulfate reduction and hydrogen sulfide fluxes in the central Namibian coastal upwelling zone. *Geochimica et Cosmochimica Acta* **67**, 4505-4518.

76. Brüchert V, Currie B, Peard KR (2009) Hydrogen sulphide and methane emissions on the central Namibian shelf. *Progress in Oceanography* **83**, 169-179.

77. Francois R (1988) A study on the regulation of the concentrations of some trace metals (Rb, Sr, Zn, Pb, Cu, V, Cr, Ni, Mn and Mo) in Saanich Inlet sediments, British Columbia, Canada. *Marine Geology* **83**, 285-308.

78. Ravizza G, Turekian KK, Hay BJ (1991) The geochemistry of rhenium and osmium in recent sediments from the Black Sea. *Geochimica et Cosmochimica Acta* **55**, 3741-3752.

79. Murray JW (1991) Black Sea oceanography: Results of the 1988 Black Sea Expedition. *Deep Sea Research* **38**, S655-S1266.

80. Buesseler KO, Benitez CR (1994) Determination of mass accumulation rates and sediment radionuclide inventories in the deep Black Sea. *Deep-Sea Research I* **41**, 1605-1615.

81. Dean WE, Piper DZ, Peterson LC (1999) Molybdenum accumulation in Cariaco basin sediment over the past 24 k.y.: A record of water-column anoxia and climate. *Geology* **27**, 507-510.

82. Giraudeau J, Meyers, PA, Christensen BA (2002) Accumulation of organic and inorganic carbon in Pliocene-Pleistocene sediments along the SW African margin. *Marine Geology* **180**, 49-69.

83. Borchers SL, Schnetger B, Böning P, Brumsack H-J (2005) Geochemical signatures of the Namibian diatom belt: Perennial upwelling and intermittent anoxia. *Geochemistry, Geophysics, Geosystems* **6**: doi:10.1029/2004GC000886.

84. McManus J, Berelson WM, Severmann S, Poulson RL, Hammond DE, Klinkhammer GP, Holm C (2006) Molybdenum and uranium geochemistry in continental margin sediments: Paleoproxy potential. *Geochimica et Cosmochimica Acta* **70**, 4643-4662.

85. Sifeddine A, Gutiérrez D, Ortlieb L, Boucher H, Velazco F, Field D, Vargas G, Boussafir M, Salvatteci R, Ferriera V, García M, Valdés J, Caquineau S, Mandeng-Yogo

M, Cetin F, Solis J, Soler P, Baumgartner T (2008) Laminated sediments from the central Peruvian continental slope: A 500 year record of upwelling system productivity, terrestrial runoff and redox conditions. *Progress in Oceanography* **79**, 190-197.

86. Gutiérrez D, Sifeddine A, Field DB, Ortlieb L, Vargas G, Chávez FP, Velazco F, Ferriera V, Tapia P, Salvatteci R, Boucher H, Morales MC, Valdés J, Ress J-L, Campusano A, Boussafir M, Mandeng-Yogo M, García M, Baumgartner T (2009) Rapid reorganization in ocean biogeochemistry off Peru towards the end of the Little Ice Age. *Biogeosciences* **6**, 835-848.

87. Poulson Brucker RL, McManus J, Severmann S, Berelson WM (2009) Molybdenum behavior during early diagenesis: Insights from Mo isotopes. *Geochemistry, Geophysics, Geosystems* **10**, doi:10.1029/2008GC002180.

88. Brumsack H-J (1989) Geochemistry of recent TOC-rich sediments from the Gulf of California and the Black Sea. *Geologische Rundschau* **78**, 851-882.

89. Zheng Y, Anderson RF, van Geen A, Kuwabara J (2000) Authigenic molybdenum formation in marine sediments: A link to pore water sulfide in the Santa Barbara Basin. *Geochimica et Cosmochiicam Acta* **64**, 4165-4178.

90. Poulson RL, Siebert C, McManus J, Berelson WM (2006) Authigenic molybdenum isotope signatures in marine sediments. *Geology* **34**, 617-620.

91. Rauch JN, Pacyna JM (2009) Earth's global Ag, Al, Cr, Cu, Fe, Ni, Pb, and Zn cycles. *Global Biogeochemical Cycles* **23**, doi:10.1029/2008GB003376.

92. Martin J-M, Meybeck M (1979) Elemental mass-balance of material carried by major world rivers. *Marine Chemistry* **7**, 173-206.

93. Jeandel C, Minster JF (1987) Chromium behavior in the ocean: Global versus regional processes. *Global Biogeochemical Cycles* **1**, 131-154.

94. van der Weijden CH, Reith M (1982) Chromium(III) – chromium(VI) interconversions in seawater. *Marine Chemistry* **11**, 565-572.

95. Ellis AS, Johnson TM, Bullen TD (2004) Using chromium stable isotope ratios to quantify Cr(VI) reduction: Lack of sorption effects. *Environmental Science & Technology* **38**, 3604-3607.

96. Smith E, Ghiassi K (2006) Chromate removal by an iron sorbent: Mechanism and modeling. *Water Environment Research* **78**, 84-93.

97. Zachara JM, Girvin DC, Schmidt RL, Resch CT (1987) Chromate adsorption on amorphous iron oxyhydroxide in the presence of major groundwater ions. *Environmental Science & Technology* **21**, 589-594.

98. Zachara JM, Cowan CE, Schmidt RL, Ainsworth CC (1988) Chromate adsorption by kaolinite. *Clays and Clay Minerals* **36**, 317-326.

99. Turekian KK, Imbrie J (1966) The distribution of trace elements in deep-sea sediments of the Atlantic Ocean. *Earth and Planetary Science Letters* **1**, 161-168.

100. Chester R, Hughes MJ (1969) The trace element geochemistry of a North Pacific pelagic clay core. *Deep-Sea Research* **16**, 639-654.

101. Cronan DS (1969) Average abundances of Mn, Fe, Ni, Co, Cu, Pb, Mo, V, Cr, Ti and P in Pacific pelagic clays. *Geochimica et Cosmochimica Acta* **33**, 1562-1565.

102. Piper DZ, Dean WE (2002) Trace-element deposition in the Cariaco Basin under sulfate reducing conditions – a history of the local hydrography and global climate, 20 ka to present. *USGS Professional Paper 1670*, 41p.

103. Lyons TW, *unpublished data*

104. Brumsack H-J, Gieskes JM (1983) Interstitial water trace-metal chemistry of laminated sediments from the Gulf of California, Mexico. *Marine Chemistry* **14**, 89-106.

105. Calvert SE (1966) Accumulation of diatomaceous silica in sediments of the Gulf of California. *GSA Bulletin* **77**, 569-596.

106. Elderfield H, Schultz A (1996) Mid-ocean ridge hydrothermal fluxes and the chemical composition of the ocean. *Annual Review of Earth and Planetary Sciences* **24**, 191-224.

107. Stein CA, Stein S, Pelayo AM (1995) Heat flow and hydrothermal circulation. *AGU Geophysical Monographs*. **91**, 425-445.

108. Kishida K, Sohrin Y, Okamura K, Ishibashi J (2004) Tungsten enriched in submarine hydrothermal fluids. *Earth and Planetary Science Letters* **222**, 819-827.

109. German CR, Campbell AC, Edmond JM (1991) Hydrothermal scavenging at the Mid-Atlantic Ridge: Modification of trace element dissolved fluxes. *Earth and Planetary Science Letters* **107**, 101-114.

110. Berner RA (2004) A model for calcium, magnesium and sulfate in seawater over Phanerozoic time. *American Journal of Science* **304**, 438-453.

111. Seyfried, Jr. WE, Mottle MJ (1982) Hydrothermal alteration of basalt by seawater under seawater-dominated conditions. *Geochimica et Cosmochimica Acta* **46**, 985-1002.

112. Von Damm KL, Edmond JM, Measures CI, Grant B (1985) Chemistry of submarine hydrothermal solutions at Guymas Basin, Gulf of California. *Geochimica et Cosmochimica Acta* **49**, 2221-2237.

113. Wheat CG, Mottl MJ, Rudnicki M (2002) Trace element and REE composition of a low-temperature ridge-flank hydrothermal spring. *Geochimica et Cosmochimica Acta* **66**, 3693-3705.

114. Emerson S, Hedges J (2008) *Chemical Oceanography and the Marine Carbon Cycle*. Cambridge University Press, New York, NY.

115. Sander S, Koschinsky A (2000) Onboard-ship redox speciation of chromium in diffuse hydrothermal fluids from the North Fiji Basin. *Marine Chemistry* **71**, 83-102.

116. Michalopoulos P, Aller RC (1995) Rapid clay mineral formation in Amazon Delta sediments: Reverse weathering and oceanic elemental cycles. *Science* **270**, 614-617.

117. Sarmiento JL, Gruber N (2006) *Ocean Biogeochemical Dynamics*. Princeton University Press, Princeton, NJ.

118. Dunne JP, Sarmiento JL, Gnanadesikan A (2007) A synthesis of global particle export from the surface ocean and cycling through the ocean interior and on the seafloor. *Global Biogeochemical Cycles* **21**, doi:10.1029/2006GB002907.

119. Dahl TW, Hammarlund EU, Anbar AD, Bond DPG, Gill BC, Gordon GW, Knoll AH, Nielsen AT, Schovsbo NH, Canfield DE (2010) Devonian rise in atmospheric oxygen correlated to the radiations of terrestrial plants and large predatory fish. *Proceedings of the National Academy of Sciences USA* **107**, 17911-17915.

120. Kendall B, Creaser RA, Gordon GW, Anbar AD (2009) Re-Os and Mo isotope systematics of black shales from the Middle Proterozoic Velkerri and Wollogorang Formations, McArthur Basin, northern Australia. *Geochimica et Cosmochimoca Acta* **73**, 2534-2558.

121. Archer DE, Morford JL, Emerson SR (2002) A model of suboxic sedimentary diagenesis suitable for automatic tuning and gridded global domains. *Global Biogeochemical Cycles* **16**, doi:10.1029/2000GB001288.

122. Ridgwell A, Hargreaves JC, Edwards NR, Annan JD, Lenton TM, Marsh R, Yool A, Watson A (2007) Marine geochemical data assimilation in an efficient Earth System Model of global biogeochemical cycling. *Biogeosciences* **4**, 87-104.

123. Meyers SR, Sageman BB, Lyons TW (2005) Organic carbon burial rate and the molybdenum proxy: Theoretical framework and application to Cenomanian-Turonian oceanic anoxic event 2. *Paleoceanography* **20**, doi:10.1029/2004PA001068.

124. Hetzel A, Böttcher ME, Wortmann UG, Brumsack H-J (2009) Paleo-redox conditions during OAE 2 reflected in Demerara Rise sediment geochemistry (ODP Leg 207) *Palaeogeography, Palaeoclimatology, Palaeoecology* **273**, 302-328.

CHAPTER 6

CONCLUSIONS

Through decades of important research, many of the first-order features of the chemical evolution of the atmosphere and oceans are relatively well established. For example, it is apparent that much of Earth's early history (the Archean Eon) was marked by pervasively reducing conditions in the ocean and atmosphere. Although it is suggested here that the temporal fidelity of the rare sulfur isotope record in fingerprinting the presence of a continuous and uninterrupted reducing atmospheric condition should be revisited, it is nonetheless clear that there are stark difference in Earth surface chemistry between the Archean and Proterozoic. However, the richness of potential information embedded in the rare sulfur isotope record, and the relative infancy of our understanding, will drive formative research on Earth's early chemical history for years to come.

Perhaps even less is understood about the mechanistic and temporal coupling between the accumulation of O_2 in the atmosphere and the ventilation of deep (and intermediate) ocean waters. For example, the strength of the biological carbon pump within the ocean has almost certainly changed with time, due to secular and periodic changes in the structure and functionality of planktonic ecosystems and the evolution of biogenic mineral precipitation. Quantitative relationships between atmospheric O_2 levels and the ventilation potential of the deep ocean remain to be elaborated, and the detailed evolution of oceanic redox structure as a function of atmospheric O_2 levels, with its attendant effects on trace nutrient availability, biological evolution, and global element cycling, remain ripe avenues for theoretical and empirical exploration.

APPENDIX A: ANALYTICAL DATA FOR THE ABDP-9 CORE

Table A1. Analytical data for the Mt. McRae Shale.

Depth (m)	**Fe_T (wt%)**	**Fe_{carb} (wt%)**	**Fe_{Ox} (wt%)**	**Fe_{mag} (wt%)**	**Fe_{PY} (wt%)**	**Fe_{HR} (wt%)**	**Fe_{HR}/Fe_T**	**Fe_{PY}/Fe_{HR}**
126.15	3.0	0.22	0.04	0.15	0.24	0.65	0.22	0.37
127.25	3.2	0.09	0.03	0.04	0.59	0.75	0.24	0.79
128.17	3.1	0.00	0.02	0.04	0.75	0.81	0.26	0.93
129.01	3.1	0.10	0.02	0.05	0.87	1.04	0.34	0.84
130.06	2.5	0.04	0.02	0.05	0.43	0.54	0.22	0.80
130.71	7.3	0.08	0.03	0.05	4.28	4.44	0.61	0.96
130.76	2.4	0.04	0.03	0.33	0.33	0.73	0.30	0.45
132.13	2.5	0.07	0.04	0.08	0.41	0.60	0.24	0.68
133.97	4.2	0.06	0.03	0.17	0.42	0.68	0.16	0.62
135.58	13.7	0.44	0.03	0.04	9.79	10.30	0.75	0.95
136.15	4.4	0.00	0.01	0.08	2.97	3.06	0.70	0.97
136.67	6.1	0.00	0.01	0.02	3.77	3.80	0.62	0.99
136.94	9.3	0.08	0.02	0.01	6.75	6.86	0.74	0.98
137.31	7.4	0.08	0.02	0.01	4.66	4.77	0.64	0.98
137.68	9.8	0.06	0.02	0.01	7.63	7.72	0.79	0.99
137.96	6.8	0.08	0.02	0.08	4.78	4.96	0.73	0.96
138.38	6.8	0.12	0.05	0.01	4.79	4.97	0.73	0.96
138.74	6.9	0.11	0.01	0.01	4.55	4.68	0.68	0.97
139.01	11.9	0.15	0.01	0.09	9.38	9.63	0.81	0.97
139.65	6.8	0.08	0.02	0.01	5.31	5.42	0.80	0.98
139.97	4.7	0.08	0.46	0.09	3.61	4.24	0.90	0.85
140.25	6.1	0.07	0.01	0.02	5.08	5.18	0.85	0.98
140.50	4.5	0.36	0.02	0.01	3.75	4.14	0.92	0.91
140.95	5.3	0.54	0.02	0.03	4.47	5.06	0.95	0.88
141.17	5.8	0.07	0.01	0.01	4.81	4.90	0.84	0.98
141.47	5.2	0.11	0.01	0.01	4.12	4.25	0.82	0.97
141.72	4.9	0.05	0.01	0.01	4.01	4.08	0.83	0.98
142.08	4.3	0.05	0.01	0.01	3.39	3.46	0.80	0.98
142.60	3.4	0.05	0.44	0.00	2.03	2.52	0.74	0.81
143.45	7.9	0.43	0.03	0.03	5.37	5.86	0.74	0.92
144.36	5.4	0.09	0.02	0.08	1.78	1.97	0.36	0.90
145.61	5.1	0.11	0.05	0.25	1.04	1.45	0.28	0.72
146.45	7.1	0.13	0.05	0.06	4.07	4.31	0.61	0.94
147.30	4.5	0.12	0.52	0.09	1.34	2.07	0.46	0.65
148.27	3.8	0.07	0.03	0.10	1.12	1.32	0.35	0.85
149.30	4.3	0.09	0.02	0.06	2.57	2.74	0.64	0.94
150.24	4.6	0.09	0.04	0.11	1.65	1.89	0.41	0.87
152.65	3.9	0.16	0.04	0.06	0.62	0.88	0.23	0.70

153.08	-	1.26	0.04	0.11	0.84	2.25	-	0.37
153.18	2.7	0.00	0.03	0.10	0.38	0.51	0.19	0.74
157.80	8.0	0.79	0.09	0.77	1.69	3.34	0.42	0.51
158.91	5.9	1.16	0.09	0.22	1.06	2.53	0.43	0.42
165.56	18.1	4.23	0.13	1.22	0.58	6.16	0.34	0.09
167.76	15.0	2.83	0.15	1.18	0.41	4.57	0.30	0.09
168.36	16.0	5.01	0.29	1.12	0.65	7.07	0.44	0.09
168.90	19.7	4.72	0.41	1.28	1.82	8.23	0.42	0.22
169.68	12.8	2.21	0.18	0.78	1.15	4.32	0.34	0.27
169.94	21.2	4.61	0.46	1.47	2.46	9.00	0.42	0.27
170.17	15.7	1.99	0.29	0.88	1.62	4.78	0.30	0.34
170.39	18.5	3.86	0.47	1.67	2.31	8.31	0.45	0.28
170.55	16.2	3.76	0.15	0.77	0.52	5.20	0.32	0.10
170.86	13.7	3.09	0.15	0.85	1.41	5.50	0.40	0.26
170.94	16.6	3.30	0.17	0.82	3.75	8.04	0.48	0.47
171.22	13.8	2.14	0.15	1.26	2.87	6.42	0.47	0.45
173.09	13.0	1.84	0.17	0.73	1.27	4.01	0.31	0.32
173.50	13.9	0.84	0.09	0.53	2.80	4.26	0.31	0.66
173.73	16.8	2.55	0.24	1.33	1.44	5.56	0.33	0.26
174.67	4.8	1.55	0.12	0.72	2.44	4.83	1.01	0.50
143.45	7.9	0.43	0.03	0.03	5.37	5.86	0.74	0.92
144.36	5.4	0.09	0.02	0.08	1.78	1.97	0.36	0.90
145.61	5.1	0.11	0.05	0.25	1.04	1.45	0.28	0.72
146.45	7.1	0.13	0.05	0.06	4.07	4.31	0.61	0.94
147.30	4.5	0.12	0.52	0.09	1.34	2.07	0.46	0.65
148.27	3.8	0.07	0.03	0.10	1.12	1.32	0.35	0.85
149.30	4.3	0.09	0.02	0.06	2.57	2.74	0.64	0.94
150.24	4.6	0.09	0.04	0.11	1.65	1.89	0.41	0.87
152.65	3.9	0.16	0.04	0.06	0.62	0.88	0.23	0.70
153.08	-	1.26	0.04	0.11	0.84	2.25	-	0.37
153.18	2.7	0.00	0.03	0.10	0.38	0.51	0.19	0.74
157.80	8.0	0.79	0.09	0.77	1.69	3.34	0.42	0.51
158.91	5.9	1.16	0.09	0.22	1.06	2.53	0.43	0.42
165.56	18.1	4.23	0.13	1.22	0.58	6.16	0.34	0.09
167.76	15.0	2.83	0.15	1.18	0.41	4.57	0.30	0.09
168.36	16.0	5.01	0.29	1.12	0.65	7.07	0.44	0.09
168.90	19.7	4.72	0.41	1.28	1.82	8.23	0.42	0.22
169.68	12.8	2.21	0.18	0.78	1.15	4.32	0.34	0.27
169.94	21.2	4.61	0.46	1.47	2.46	9.00	0.42	0.27
170.17	15.7	1.99	0.29	0.88	1.62	4.78	0.30	0.34
170.39	18.5	3.86	0.47	1.67	2.31	8.31	0.45	0.28
170.55	16.2	3.76	0.15	0.77	0.52	5.20	0.32	0.10
170.86	13.7	3.09	0.15	0.85	1.41	5.50	0.40	0.26
170.94	16.6	3.30	0.17	0.82	3.75	8.04	0.48	0.47

171.22	13.8	2.14	0.15	1.26	2.87	6.42	0.47	0.45
173.09	13.0	1.84	0.17	0.73	1.27	4.01	0.31	0.32
173.50	13.9	0.84	0.09	0.53	2.80	4.26	0.31	0.66
173.73	16.8	2.55	0.24	1.33	1.44	5.56	0.33	0.26
174.67	4.8	1.55	0.12	0.72	2.44	4.83	1.01	0.50
175.51	9.2	1.05	0.16	0.52	1.51	3.24	0.35	0.47
177.10	8.8	0.40	0.08	0.80	1.95	3.23	0.37	0.60
178.61	7.3	0.00	0.05	0.34	2.02	2.41	0.33	0.84
179.05	7.6	0.00	0.06	0.45	2.04	2.55	0.34	0.80
180.33	9.3	0.45	0.10	0.54	1.87	2.96	0.32	0.63
181.20	10.1	0.98	0.12	0.71	1.71	3.52	0.35	0.49
182.50	5.1	0.22	0.07	0.22	0.99	1.50	0.29	0.66
183.65	8.0	0.53	0.08	1.16	1.49	3.26	0.41	0.46
185.43	10.2	3.54	0.17	1.04	0.84	5.59	0.55	0.15
188.01	6.7	0.16	0.11	0.19	2.03	2.49	0.37	0.81
188.87	7.0	0.26	0.15	0.38	1.05	1.84	0.26	0.57

APPENDIX B: SOURCES FOR THE CHROMIUM AND MOLYBDENUM SHALE ENRICHMENT DATABASE

Table B1. Age and geologic setting of units compiled for this study.

Unit	Location	Age (Ma)	Metamorphic Grade	Basin Type	Setting	Ref.
Cariaco Basin	Venezuelan Borderlands	mod	N/A	pull-apart basin	shelfal marine (upwelling)	(B1)
Peru margin	Offshore Peru	0.1-0	N/A	active margin	shelfal marine (upwelling)	(B2, B3)
Namibian margin	Offshore namibia	0.1-0	N/A	passive margin	shelfal marine (upwelling)	(B3)
Black Sea Unit I, II	Black Sea	0.1-0	N/A	silled marine basin	deep marine	(B3)
Gulf of California	Baja Peninsula	0.1-0	N/A	passive margin	shallow marine (upwelling)	(B3)
Mediterranean sapropel	Med. Sea (Pleistocene Tyrrhenian Sea)	0.7-3.6	N/A	silled marine basin	deep marine	(B4, B5)
IODP Leg 302	Lomonosov Ridge, Arctic Ocean	55.8	N/A	oceanic rift basin	shallow marine	(B6)
Mugi/Ryujin shales, Shimanto Supergroup	Japan	67	sub-greenschist	forearc/accretionary complex	pelagic to turbididic	(B7)
Pembina/Gammoan (Pierre Fm.)	Cretaceous interior seaway, Manitoba	83	sub-greenschist	foredeep/ epicontinental sea	shallow to deep marine	(B8)

Unit	Location	Age (Ma)	Metamorphic Grade	Basin Type	Setting	Ref.
La Luna Fm.	Maracaibo Basin, Venezuela	85-100	sub-greenschist	passive margin	shelfal marine	(B9)
Niobrara Fm.	Cretaceous interior seaway, Manitoba	89	sub-greenschist	foredeep/ epicontinental sea	shallow to deep marine	(B8)
Demarara Rise	Surinam, Guyana	91	sub-greenschist	rift to passive margin	shallow marine	(B10)
Assiniboine Mbr., Favel Fm., Morden Shale	Cretaceous interior seaway, Manitoba	93	sub-greenschist	foredeep/ epicontinental sea	shallow to deep marine	(B8)
ODP Site 103-641A	Galician Margin, N.W. Spain	93.6	sub-greenschist	post-rift passive margin	deep marine	(B11)
DSDP 530A	Angola Basin, Namibia	89.3-99.6	sub-greenschist	passive continental margin	offshore pelagic (upwelling)	(B12)
Hatteras Fm. (ODP Site 1276)	Newfoundland Basin, proto-North Atlantic	99.6-112	sub-greenschist	passive continental margin	deep marine	(B13)
Machiques Mbr., Apon Fm.	Maracaibo Basin, Venezuela	107.5	sub-greenschist	passive margin	shallow marine	(B14)
Julia Creek Shale	Eromanga and Carpentania Basins, Queensland, Australia	112	sub-greenschist	epicontinental sea	shallow marine	(B15)
Norwegian Shelf black shales	Norwegian Shelf/Barents Sea	130-155	sub-greenschist	epicontinental sea	shallow to deep marine	(B16)
Paska Fm.	Siberian Platform	145.5	sub-greenschist	epicontinental sea	shallow marine (upwelling	(B17)

Unit	Location	Age (Ma)	Metamorphic Grade	Basin Type	Setting	Ref.
Kimmeridge Clay Fm.	Yorkshire, U.K.	155	sub-greenschist	oceanic rift basin	deep marine	(B18, B19)
Posidonia Shale	N.W. Germany	183	sub-greenschist	epicontinental sea	shallow to deep marine	(B20)
Jet Rock, Whitby Mudstone Fm.	Yorkshire, U.K.	183	sub-greenschist	epicontinental sea	deep marine	(B21)
Gordondale Mbr., Fernie Fm.	Western Canadian Sedimentary Basin, Canada	189.6	sub-greenschist	silled epicontinental sea	deep marine	(B22)
Kupferschiefer Shale (unmineralized)	Zechstein Basin, Poland	247	greenschist	foreland	marine turbidite	(B23)
Meade Peak Mbr., Phosphoria Fm.	S.E. Idaho	270.6	sub-greenschist	epicratonic basin (Phosphoria Sea)	shallow marine	(B24)
Stark Shale, Mecca Quary Shale Mbr.	Midcontinent Basin, Central U.S.	300	sub-greenschist	epicontinental sea	shallow to deep marine	(B25)
Hushpuckney Shale Mbr., Coffeyville Fm.	Midcontinent Basin, Central U.S.	300	sub-greenschist	epicontinental sea	offshore marine	(B26)
Excello Shale	Midcontinent Basin, Central U.S.	305	sub-greenschist	epicontinental sea	deep marine	(B27)
Oakley, Unnamed, Anna, Little Osage Fms.	Midcontinent Basin, Central U.S.	308	sub-greenschist	epicontinental sea	offshore (deep) marine	(B28)
Lost Branch Shale	Kansas	308	sub-greenschist	epicontinental sea	shallow marine	(B29)

Unit	Location	Age (Ma)	Metamorphic Grade	Basin Type	Setting	Ref.
Golata Fm.	Western Canadian Sedimentary Basin, British Columbia	328.3	sub-greenschist	epicontinental sea	shallow to deep marine	(B30)
Rhinestreet Shale	Appalachain Basin, N.Y.	345.3	sub-greenschist	foreland	deltaic	(B31)
Bakken Fm.	Williston Basin, S.W. Manitoba	361	sub-greenschist	epicontinental sea	shallow to deep marine	(B32)
Exshaw Fm.	Midcontinent Basin, Central U.S.	361	sub-greenschist	epicontinental sea	deep marine	(B33)
Sunbury Shale	Midcontinent Basin, Central U.S.	361	sub-greenschist	epicontinental sea	deep marine	(B34)
Henley Subunit, Borden Fm.	Midcontinent Basin, Kentucky, U.S.	361	sub-greenschist	epicontinental sea	deltaic	(B34)
Big Valley and Exshaw Fms.	Alberta Platform, Canada	365	sub-greenschist	epicontinental sea	distal shelf	(B35)
Chattanooga Shale	Midcontinent Basin, Central U.S.	365	sub-greenschist	epicontinental sea	shallow marine	(B36)
Ohio Shale (Cleveland, Three Lick, Huron Mbrs.), upper Olentangy Fm.	Central U.S.	365	sub-greenschist	epicontinental sea	marine turbidites	(B34)
Grassy Creek Shale	Illinois Basin, Central U.S.	365	lower greenschist	epicontinental sea	deep marine	(B37)
Annulata Black Shales	Holy Cross Mountains, Poland	374.5	sub-greenschist	epicontinental sea	shallow to deep marine	(B38)

Unit	Location	Age (Ma)	Metamorphic Grade	Basin Type	Setting	Ref.
Upper Besa River, Fort Simpson, Muskwa, Lower Besa River Fms.	Western Canadian Sedimentary Basin, British Columbia	374.5-391.8	sub-greenschist	epicontinental sea	shallow to deep marine	(B30)
Oatka Creek Fm.	Appalachain Basin, N.Y.	387.5	sub-greenschist	foreland basin	shallow marine	(B39)
Zdanow Shales	Bardzkie Mtns., Poland	416	sub-greenschist	trench-volcanic arc	accretionary prism	(B40)
Monograptus leptotheca band (Derwenlas Fm.)	Welsh Basin, Wales, U.K.	443.7	sub-greenschist	rift	turbidite	(B41)
Unterer Graptolithenschiefer	Graefenthal Horst, Bavaria, Germany	443.7	lower greenschist	passive margin	shallow marine	(B42)
Rastrites Shale	Baltic Basin, Sweden	443.7	greenschist	epicontinental sea to foreland	shallow to deep marine	(B43, B44)
Dicellograptus Shale	Baltic Basin, Sweden	460.9	greenschist	epicontinental sea	shallow to deep marine	(B43)
Winnipeg Fm.	Williston Basin, S. Manitoba	460	sub-greenschist	epicontinental sea	shallow marine	(B45)
Bright Eye, Patrick Brook Fms.	Miramichi Highlands, New Brunswick	478.5	sub-greenschist	oceanic back-arc	deep marine	(B46, B47)
Toyen Shale	Baltic Basin, Sweden	478.6	greenschist	epicontinental sea	shallow to deep marine	(B43)
Alum Shale	Fennoscandian Shield, Sweden	499	greenschist	epicontinental sea	shallow to deep marine	(B48)

Unit	Location	Age (Ma)	Metamorphic Grade	Basin Type	Setting	Ref.
Yuanshan, Shiyantou Fms.	Yangtze Platform, S. China	521-526.5	sub-greenschist	passive margin	deep marine	(B49)
Nuititang Fm.	Yangtze Platform, S. China	536-542	sub-greenschist	passive margin	deep marine	(B50)
Yuertushi Fm.	Tarim Basin, China	542	sub-greenschist	passive margin	shelfal marine	(B51)
Guojiaba, Jiumenchong Fms.	S. China	542	sub-greenschist	passive margin	shallow to deep marine	(B52)
Nama Group	Kalahari Craton, Namibia	548	greenschist	foreland basin	shallow to deep marine	(B53)
Doushantuo Fm.	Yangtze Block, S. China	620-551	sub-greenschist	passive margin	deep marine	(B54)
Datangpo Fm.	Yangtze Block, S. China	654	sub-greenschist	passive margin	shallow to deep marine	(B55)
Mineral Fork, Cottonwood Fms.	Utah, U.S.	766	sub-greenschist	epicontinental sea (?)	distal shelf	(B56-B58)
Wynniatt Fm., Shaler Supergroup	Amundsen Basin, Victoria Island, N.W. Territories, Canada	~850	greenschist	epicontinental sea	shallow (open) marine; deltaic	(B56, B59)
Kandyk, Ryaninovsk Fms.	S.E. Russia	~1005-950	greenschist	passive margin	deltaic to slope-fan	(B60)
Malosakhora, Ust-Kirba Fms.	Yudoma-Maya depression, Russia	1005	greenschist	passive margin	shallow marine	(B61)

Unit	Location	Age (Ma)	Metamorphic Grade	Basin Type	Setting	Ref.
Kumakha Shale, Lakhanda Group	Siberian Platform, Maya depression, Siberia	1017	greenschist	epicontinental sea	shallow shelfal marine	(B62)
Rabanpalli Fm.	Bhima Basin, Dharwar craton, India	~1100	greenschist	pull-apart basin	deltaic	(B63)
Totta Fm., Kerpyl Group	S.E. Russia	~1100	greenschist	passive margin	tidal to shallow marine	(B60)
Bylot Supergroup	Borden Basin, Bylot and Baffin Islands, Canada	~1100-1200	sub-greenschist	rift or transtensional basin	shallow marine shelf to subtidal-basinal	(B64, B65)
Ft. Confidence Fm., Dismal Lakes Group	Arctic Canada	~1300	sub-greenschist	epicontinental sea	marginal marine	(B66)
Talyn, Svelty Fms., Aimchan Group	S.E. Russia	~1350	greenschist	passive margin	shallow marine	(B60)
Trekhgornaya, Dim Fms., Uchur Group	S.E. Russia	~1400	greenschist	passive margin	open, shallow marine	(B60)
Velkerri Fm., Roper Group	McArthur Basin, N. Australia	1400	lower greenschist	epicratonic basin	open-ocean ramp/shelf	(B67)
Fort Steele, Aldridge, Newland Fms.	Purcell-Belt Basin, Montana, U.S.-Canada	1497-1470	greenschist	epicratonic basin; pull-apart(?) or back-arc	deep water turbidite to shallow marine	(B68)
Lawn Hill Fm., McNamara Group	Mt. Isa Inlier, Australia	1595	greenschist	sag basin or strike-slip	shallow marine (turbiditic)	(B69, B70)

Unit	Location	Age (Ma)	Metamorphic Grade	Basin Type	Setting	Ref.
Roraima Group	Guayana Shield, Amazon Craton, Brazil	~1600	greenschist	foreland basin	shallow(?) marine	(B71)
Lady Loretta Fm., McNamara Group	Mt. Isa Basin, Australia	~1670-1570	sub-greenschist	sag basin, or inboard continental arc	deep marine	(B72)
Surprise Creek Fm.	Mt. Isa Inlier, Australia	1688	greenschist	sag basin or strike-slip	distal marine	(B69, B73)
Wollogorang Fm., Tawallah Group	McArthur Basin, Australia	1730	greenschist	intracratonic basin	open deep marine	(B74)
Cumbum Fm., Cuddapah Supergroup	E. Dharwar Craton, India	1800	lower greenschist	foreland	turbidites	(B75)
Rove Fm., Animikie Group	Animikie Basin, Superior Province, Canada	1840	lower greenschist	foreland	turbidites	(B76)
Par, Morar Fms., Gwalior Group	Bundelkhand Craton, C. India	~1900	sub-greenschist	passive margin	outer shelf marine	(B77)
Nullataktok Fm., Ramah Group	Labrador, Canada	~1900	sub-greenschist	foreland	marine turbidites	(B78)
Pilguyarvi Fm., Pechenga Group	Kola Peninsula, Russia	1990	sub-greenschist	uncertain; continental rift, oceanic trench, or continental slope	shallow to deep marine	(B79, B80)
Soutpansberg Shales	Kaapvaal Craton, S. Africa	2021-1875	greenschist	rift basin	shallow marine	(B81, B82)

References:

B1. Van Daele M, et al. (2011) Reconstruction of Late-Quaternary sea- and lake-level changes in a tectonically active marginal basin using seismic stratigraphy: The Gulf of Cariaco, NE Venezuela. *Mar Geol* 279:37-51.

B2. Böning P, et al. (2004) Geochemistry of Peruvian near-surface sediments. *Geochim Cosmochim Acta* 68:4429-4451.

B3. Brumsack H-J (2006) The trace metal content of recent organic carbon-rich sediments: Implications for Cretaceous black shale formation. *Palaeogeogr Palaeoclimatol Palaeoecol* 232:344-361.

B4. Gehrke GE, Blum JD, Meyers PA (2009) The geochemical behavior and isotopic composition of Hg in a mid-Pleistocene western Mediterranean sapropel. *Geochim Cosmochim Acta* 73:1651-1665.

B5. Arnaboldi M, Meyers PA (2007) Trace element indicators of increased primary production and decreased water-column ventilation during deposition of latest Pliocene sapropels at five locations across the Mediterranean Sea. *Palaeogeogr Palaeoclimatol Palaeoecol* 249:425-443.

B6. Backman J, Moran K (2009) Expanding the Cenozoic paleoceanographic record in the Central Arctic Ocean: IODP Expedition 302 Synthesis. *Central European Journal of Geosciences* 1:157-175.

B7. Kato Y, Fujinaga K, Suzuki K (2005) Major and trace element geochemistry and Os isotopic composition of metalliferous umbers from the Late Cretaceous Japanese accretionary complex. *Geochem Geophys Geosyst* 6:Q07004.

B8. McNeil DH, Caldwell WGE Cretaceous rocks and their foraminifera in the Manitoba Escarpment. *Geol Assoc Canada Spec Paper* 21.

B9. Lo Monaco S, et al. (2002) Distribution of major and trace elements in La Luna Formation, Southwestern Venezuelan Basin. *Org Geochem* 33:1593-1608.

B10. Erbacher J, Mosher D, Bauldauf J, Malone M (2002) Demerara Rise: Equatorial Cretaceous and Paleogene Paleoceanographic Transect, Western Atlantic. *Ocean Drilling Program* Scientific Prospectus No. 107. Available at: http://www-odp.tamu.edu/publications.

B11. Thurow JW, et al. (1988) in *Proceedings of the Ocean Drilling Program, Scientific Results*, eds Boillot G, Winterer EL, pp 587-634.

B12. Forster A, et al. (2008) The Cenomanian/Turonian oceanic anoxic event in the South Atlantic: New insights from a geochemical study of DSDP Site 530A. *Palaeogeography, Palaeoclimatology, Palaeoecology* 267:256-283.

B13. Arnaboldi M, Meyers P (2006) in *Proceedings of the Ocean Drilling Program, Scientific Results*, eds Tucholke BE, Sibuet J-C, Klaus A, pp 1-10.

B14. Rey O, Simo (Toni) J., Lorente M. (2004) A record of long- and short-term environmental and climatic change during OAE3: La Luna Formation, Late Cretaceous (Santonian–early Campanian), Venezuela. *Sedimentary Geology* 170:85-105.

B15. Patterson JH, Ramsden AR, Dale LS, Fardy JJ (1986) Geochemistry and mineralogical residences of trace elements in oil shales from Julia Creek, Queensland, Australia. *Chem Geol* 55:1-16.

B16. Lipinski M, Warning B, Brumsack H-J (2003) Trace metal signatures of Jurassic/Cretaceous black shales from the Norwegian Shelf and the Barents Sea. *Palaeogeogr Palaeoclimatol Palaeoecol* 190:459-475.

B17. Dypvik H, Zakharov V (2010) Late Jurassic/Early Cretaceous phosphates of Nordvik, North Siberian Basin. *Polar Res* 29:235-249.

B18. Tribovillard N-P, et al. (1994) Geochemical study of organic-matter rich cycles from the Kimmeridge Clay Formation of Yorkshire (UK): productivity versus anoxia. *Palaeogeogr Palaeoclimatol Palaeoecol* 108:165-181.

B19. Cohen AS, Coe AL, Bartlett JM, Hawkesworth CJ (1999) Precise Re-Os ages of organic-rich mudrocks and the Os isotope composition of Jurassic seawater. *Earth Planet Sci Lett* 167:159-173.

B20. Röhl H-J, Schmid-Röhl A, Oschmann W, Frimmel A, Schwark L (2001) The Posidonia Shale (Lower Toarcian) of SW-Germany: an oxygen-depleted ecosystem controlled by sea level and palaeoclimate. *Palaeogeogr Palaeoclimatol Palaeoecol* 165:27-52.

B21. Bowden SA, Farrimond P, Snape CE, Love GD (2006) Compositional differences in biomarker constituents of the hydrocarbon, resin, asphaltene and kerogen fractions: An example from the Jet Rock (Yorkshire, UK). *Organic Geochemistry* 37:369-383.

B22. Ross DJK, Bustin RM (2007) Shale gas potential of the Lower Jurassic Gordondale Member, northeastern British Columbia, Canada. *Bulletin of Canadian Petroleum Geology* 55:51-75.

B23. Pašava J, Oszczepalski S, Du A (2010) Re–Os age of non-mineralized black shale from the Kupferschiefer, Poland, and implications for metal enrichment. *Miner Deposita* 45:189-199.

B24. Piper DZ (1999) Trace Elements and Major-Element Oxides in the Phosphoria Formation at Enoch Valley, Idaho-Permian Sources and Current Reactivities. *US Geol Surv Open File* 99:163-66.

B25. Coveney J, Glascock MD (1989) A review of the origins of metal-rich Pennsylvanian black shales, central U.S.A., with an inferred role for basinal brines. *Appl Geochem* 4:347-367.

B26. Cruse AM, Lyons TW (2004) Trace metal records of regional paleoenvironmental variability in Pennsylvanian (Upper Carboniferous) black shales. *Chem Geol* 206:319-345.

B27. Hatch JR, Leventhal JS (1992) Relationship between inferred redox potential of the depositional environment and geochemistry of the Upper Pennsylvanian (Missourian) Stark Shale Member of the Dennis Limestone, Wabaunsee County, Kansas, U.S.A. *Chem Geol* 99:65-82.

B28. Hatch JR, Leventhal JS (1997) Early diagenetic partial oxidation of organic matter and sulfides in the Middle Pennsylvanian (Desmoinesian) Excello Shale member of the Fort Scott Limestone and equivalents, northern Midcontinent region, USA. *Chem Geol* 134:215-235.

B29. Heckel PH, Gibling MR, King NR (1998) Stratigraphic Model for Glacial-Eustatic Pennsylvanian Cyclothems in Highstand Nearshore Detrital Regimes. *The Journal of Geology* 106:373-384.

B30. Ross DJK, Bustin RM (2009) Investigating the use of sedimentary geochemical proxies for paleoenvironment interpretation of thermally mature organic-rich strata: Examples from the Devonian-Mississippian shales, Western Canadian Sedimentary Basin. *Chem Geol* 260:1-19.

B31. Lash GG, Engelder T (2007) Jointing within the outer arc of a forebulge at the onset of the Alleghanian Orogeny. *Journal of Structural Geology* 29:774-786.

B32. Martini AM, et al. (1998) Genetic and temporal relations between formation waters and biogenic methane: Upper Devonian Antrim Shale, Michigan Basin, USA. *Geochim Cosmochim Acta* 62:1699-1720.

B33. Selby D, Mutterlose J, Condon DJ (2009) U-Pb and Re-Os geochronology of the Aptian/Albian and Cenomanian/Turonian stage boundaries: Implications for timescale calibration, osmium isotope seawater composition and Re-Os systematics in organic-rich sediments. *Chem Geol* 265:394-409.

B34. Perkins RB, Piper DZ, Mason CE (2008) Trace-element budgets in the Ohio/Sunbury shales of Kentucky: Constraints on ocean circulation and primary productivity in the Devonian-Mississippian Appalachian Basin. *Palaeogeogr Palaeoclimatol Palaeoecol* 265:14-29.

B35. Caplan ML, Bustin RM (1998) Sedimentology and sequence stratigraphy of Devonian-Carboniferous strata, southern Alberta. *Bulletin of Canadian Petroleum Geology* 46:487-514.

B36. Leventhal JS (1991) Comparison of organic geochemistry and metal enrichment in two black shales: Cambrian Alum Shale of Sweden and Devonian Chattanooga Shale of United States. *Miner Deposita* 26:104-112.

B37. Cluff RM (1980) Paleoenvironment of the New Albany Shale Group (Devonian-Mississippian) of Illinois. *J Sediment Res* 50:767-780.

B38. Racka M, et al. (2010) Anoxic Annulata Events in the Late Famennian of the Holy Cross Mountains (Southern Poland): Geochemical and palaeontological record. *Palaeogeogr Palaeoclimatol Palaeoecol* 297:549-575.

B39. Werne JP, Sageman BB, Lyons TW, Hollander DJ (2002) An integrated assessment of a "type euxinic" deposit: Evidence for multiple controls on black shale deposition in the middle Devonian Oatka Creek formation. *American Journal of Science* 302:110-143.

B40. Porębska E, Sawłowicz Z (1997) Palaeoceanographic linkage of geochemical and graptolite events across the Silurian–Devonian boundary in Bardzkie Mountains (Southwest Poland). *Palaeogeogr, Palaeoclimatol, Palaeoecol* 132:343-354.

B41. Schofield DI, Davis JR, Waters RA, Williams M, Wilson D (2009) A new Early Silurian turbidite system in Central Wales: insights into eustatic and tectonic controls on deposition in the southern Welsh Basin. *Geological Magazine* 146:121-132.

B42. Dill H (1986) Metallogenesis of early Paleozoic graptolite shales from the Graefenthal Horst (northern Bavaria-Federal Republic of Germany). *Econ Geol* 81:889-903.

B43. Schovsbo NH (2003) The geochemistry of Lower Palaeozoic sediments deposited on the margins of Baltica. *The geochemistry of Lower Palaeozoic sediments deposited on the margins of Baltica* 50:11-27.

B44. Pedersen JH et al. (2007) Lower Paleozoic petroleum from southern Scandinavia: Implications to a Paleozoic petroleum system offshore southern Norway. *AAPG Bulletin* 91:1189-1212.

B45. Ferguson G, Betcher R, Grasby S (2007) Hydrogeology of the Winnipeg Formation in Manitoba, Canada. *Hydrogeol J* 15:573-587.

B46. Goodfellow WD, Peter JM (1996) Sulphur isotope composition of the Brunswick No. 12 massive sulphide deposit, Bathurst Mining Camp, New Brunswick: implications for ambient environment, sulphur source, and ore genesis. *Can J Earth Sci* 33:231-251.

B47. Hennessy JF, Mossman DJ (1996) Geochemistry of Ordovician black shales at Meductic, southern Miramichi Highlands, New Brunswick. *Atlantic Geology* 32.

B48. Schovsbo NH (2002) Uranium enrichment shorewards in black shales: A case study from the Scandinavian Alum Shale. *GFF* 124:107-115.

B49. Och LM, et al. Redox changes in Early Cambrian black shales at Xiaotan section, Yunnan Province, South China. *Precambrian Research* Available at: http://www.sciencedirect.com/science/article/pii/S0301926811002130.

B50. Lehmann B, et al. (2007) Highly metalliferous carbonaceous shale and Early Cambrian seawater. *Geology* 35:403-406.

B51. Yu B, Dong H, Widom E, Chen J, Lin C (2009) Geochemistry of basal Cambrian black shales and cherts from the Northern Tarim Basin, Northwest China: Implications for depositional setting and tectonic history. *J Asian Earth Sci* 34:418-436.

B52. Guo Q et al. (2007) Trace element chemostratigraphy of two Ediacaran-Cambrian successions in South China: Implications for organosedimentary metal enrichment and silicification in the Early Cambrian. *Palaeogeogr Palaeoclimatol Palaeoecol* 254:194-216.

B53. Saylor BZ, Kaufman AJ, Grotzinger JP, Urban F (1998) A composite reference section for terminal Proterozoic strata of southern Namibia. *J Sediment Res* 68:1223-1235.

B54. Chen DF, Dong WQ, Qi L, Chen GQ, Chen XP (2003) Possible REE constraints on the depositional and diagenetic environment of Doushantuo Formation phosphorites containing the earliest metazoan fauna. *Chem Geol* 201:103-118.

B55. Zhang S, Jiang G, Han Y (2008) The age of the Nantuo Formation and Nantuo glaciation in South China. *Terra Nova* 20:289-294.

B56. Young GM (2002) Geochemical investigation of a Neoproterozoic glacial unit: The Mineral Fork Formation in the Wasatch Range, Utah. *Geol Soc Am Bull* 114:387-399.

B57. Condie KC, Lee D, Farmer GL (2001) Tectonic setting and provenance of the Neoproterozoic Uinta Mountain and Big Cottonwood groups, northern Utah: constraints from geochemistry, Nd isotopes, and detrital modes. *Sediment Geol* 141-142:443-464.

B58. Butterfield NJ, Chandler FW (1992) Paleoenvironmental distribution of Proterozoic microfossils, with an example from the Agu Bay Formation, Baffin Island. *Paleontology* 35:943-957.

B59. Rainbird RH, Jefferson CW, Young GM (1996) The early Neoproterozoic sedimentary Succession B of northwestern Laurentia: Correlations and paleogeographic significance. *Geol Soc Am Bull* 108:454-470.

B60. Podkovyrov VN, Cullers RL, Kovach VP (2007) The provenance and weathering conditions of Riphean (Mesoproterozoic and Neoproterozoic) shales, siltstones, and sandstones with time, southeastern Russia (Siberia). *SEPM Spec Publ* 86:227-253.

B61. Cullers RL, Podkovyrov VN (2002) The source and origin of terrigenous sedimentary rocks in the Mesoproterozoic Ui group, southeastern Russia. *Precambrian Research* 117:157-183.

B62. Podkovyrov VN (2009) Mesoproterozoic Lakhanda Lagerstätte, Siberia: Paleoecology and taphonomy of the microbiota. *Precambrian Research* 173:146-153.

B63. Chakraborty PP, Dey S, Mohanty SP (2010) Proterozoic platform sequences of Peninsular India: Implications towards basin evolution and supercontinent assembly. *Journal of Asian Earth Sciences* 39:589-607.

B64. Kah LC, Lyons TW, Chesley JT (2001) Geochemistry of a 1.2 Ga carbonate-evaporite succession, northern Baffin and Bylot Islands: implications for Mesoproterozoic marine evolution. *Precambrian Res* 111:203-234.

B65. Turner EC, Kamber BS (2012) Arctic Bay Formation, Borden Basin, Nunavut (Canada): basin evolution, black shale, and dissolved metal systematics in the Mesoproterozoic ocean. *Precambrian Res* 208-211:1-18.

B66. Kah LC, Bartley JK, Frank TD, Lyons TW (2006) Reconstructing sea-level change from the internal architecture of stromatolite reefs: an example from the Mesoproterozoic Sulky Formation, Dismal Lakes Group, arctic Canada. *Canadian Journal of Earth Sciences* 43:653-669.

B67. Kendall B, Creaser RA, Selby D (2006) Re-Os geochronology of postglacial black shales in Australia: Constraints on the timing of “Sturtian” glaciation. *Geology* 34:729-732.

B68. Ross GM, Villeneuve M (2003) Provenance of the Mesoproterozoic (1.45 Ga) Belt basin (western North America): Another piece in the pre-Rodinia paleogeographic puzzle. *Geol Soc Am Bull* 115:1191-1217.

B69. Jackson MJ, Southgate PN, Black LP, Blake PR, Domagala J (2005) Overcoming Proterozoic quartzite sand-body miscorrelations: integrated sequence stratigraphy and SHRIMP U–Pb dating of the Surprise Creek Formation, Torpedo Creek and Warrina Park Quartzites, Mt Isa Inlier. *Aust J Earth Sci* 52:1-25.

B70. Andrews SJ (1998) Stratigraphy and depositional setting of the upper McNamara Group, Lawn Hills region, Northwest Queensland. *Econ Geol* 93:1132-1152.

B71. Santos J, et al. (2003) Age, source, and regional stratigraphy of the Roraima Supergroup and Roraima-like outliers in northern South America based on U-Pb geochronology. *Geological Society of America Bulletin* 115:331-348.

B72. Planavsky NJ, et al. (2011) Widespread iron-rich conditions in the mid-Proterozoic ocean. *Nature* 477:448-451.

B73. Domagala J, Southgate PN, McConachie BA, Pidgeon BA (2000) Evolution of the Palaeoproterozoic Prize, Gun and lower Loretta Supersequences of the Surprise Creek Formation and Mt Isa Group. *Aust J Earth Sci* 47:485-507.

B74. Shen Y, Canfield DE, Knoll AH (2002) Middle Proterozoic ocean chemistry: Evidence from the McArthur Basin, northern Australia. *Am J Sci* 302:81-109.

B75. Manikyamba C, Kerrich R, González-Álvarez I, Mathur R, Khanna TC (2008) Geochemistry of Paleoproterozoic black shales from the Intracontinental Cuddapah basin, India: implications for provenance, tectonic setting, and weathering intensity. *Precambrian Res* 162:424-440.

B76. Ojakangas RW, Morey GB, Southwick DL (2001) Paleoproterozoic basin development and sedimentation in the Lake Superior region, North America. *Sedimentary Geology* 141-142:319-341.

B77. Absar N, Raza M, Roy M, Naqvi SM, Roy AK (2009) Composition and weathering conditions of Paleoproterozoic upper crust of Bundelkhand craton, Central India: Records from geochemistry of clastic sediments of 1.9 Ga Gwalior Group. *Precambrian Res* 168:313-329.

B78. Hayashi K-I, Fujisawa H, Holland HD, Ohmoto H (1997) Geochemistry of ~1.9 Ga sedimentary rocks from northeastern Labrador, Canada. *Geochim Cosmochim Acta* 61:4115-4137.

B79. Abzalov MZ, Both RA, Brewer TS (1995) in *Norges Geologiske Undersokelse Special Publication*, eds Roberts D, Nordgulen O (Geol. Surv. Norway, Trondheim, Norway), pp 357-369.

B80. Melezhik VA, Sturt BA (1994) General geology and evolutionary history of the early proterozoic Polmak-Pasvik-Pechenga-Imandra/Varzuga-Ust'Ponoy greenstone belt in the northeastern Baltic Shield. *Earth Sci Rev* 36:205-241.

B81. Dorland HC, Beukes NJ, Gutzmer J, Evans DAD, Armstrong RA (2006) Precise SHRIMP U-Pb zircon age constraints on the lower Waterberg and Soutpansberg Groups, South Africa. *S Afr J Geol* 109:139-156.

B82. Bumby AJ, Eriksson PG, van der Merwe R, Steyn GL (2002) A half-graben setting for the Proterozoic Soutpansberg Group (South Africa): evidence from the Blouberg area. *Sediment Geol* 147:37-56.